Phase behavior of colloidal dimers and hydrodynamic instabilities in binary mixtures

Kristina Milinković

Phase behavior of colloidal dimers and hydrodynamic instabilities in binary mixtures

Fasegedrag van colloïdale dimeren en hydrodynamische instabiliteiten in binaire mengsels

(met een samenvatting in het Nederlands)

Proefschrift

ter verkrijging van de graad van doctor aan de Universiteit Utrecht op gezag van de rector magnificus, prof. dr. G. J. van der Zwaan, ingevolge het besluit van het college voor promoties in het openbaar te verdedigen op maandag 13 mei 2013 des ochtends te 10.30 uur

door

Kristina Milinković

geboren op 18 juni 1984 te Belgrado, Servië

Promotor: Prof. dr. ir. M. Dijkstra

Contents

1

Introduction

1.1 Colloidal particle systems

Colloidal suspensions are heterogeneous systems consisting of microscopic particles dispersed in a continuous medium [1]. We encounter such systems on a daily basis and examples include biological fluids like blood and milk, industrial and household products such as paints and glues, food products including butter and mayonnaise, but also fog, smoke and cosmetic preparations. Colloidal particles found within these systems can nowadays be synthesized to have various shapes and sizes and also different surface properties which generate different interactions. Due to this richness of particle properties there is a huge potential for both practical applications and for the design of fundamentally interesting systems. Furthermore, colloids are considered an important model system for atomic and molecular behavior since their characteristic time and length scales are large enough to facilitate single particle level studies in real time and real space. As a consequence, these systems have been studied extensively using experimental approaches, theory and computer simulations.

Colloidal particles fall in the size range of several nanometers to several micrometers, making the relevant length scale for these systems an intermediate one in between atomic and macroscopic sizes. Suspended in a solvent, colloidal particles experience collisions with fast-moving solvent molecules and these collisions together with thermal fluctuations within the solvent lead to the colloids performing Brownian motion. This is a very important characteristic of colloidal suspensions - the thermal fluctuations and Brownian motion allow these systems to explore the phase space in order to find the most favorable configuration. In principle, this opens the possibility of colloidal self-assembly and with it the possibility of obtaining a vast range of structures with different properties and levels of complexity.

The basic goal of any colloidal study is to understand the collective properties of large particle assemblies in terms of particle interactions, which is generally done within the framework of statistical mechanics [1]. The equilibrium structure in the context of statistical mechanics is the one with the lowest Helmholtz free energy, defined as $F = U - TS$, where U denotes the internal energy, T the temperature and S is the entropy. However, knowing which structure has the lowest free energy is not sufficient to explain and predict the structures we observe in nature - the time scales associated with particle

reorganization that is only thermally activated can be very long. This can result in a system remaining in a non-equilibrium state for a very long time and even in some structures being kinetically inaccessible in practical terms.

Self-assembly can, however, be encouraged on the particle level by altering the interactions and using cleverly designed building blocks, examples of which include patchy particles [2], lock-and-key systems [3], polyhedral particles [4], etc. The assembly can also be aided by using external fields such as gravity, electric and magnetic fields or by using confining walls or applying shear [5]. In general, due to their size, colloidal systems are easily influenced by external fields, the effects of which can be both constructive and destructive.

Two of the most ubiquitously studied classes of colloidal interactions are excluded volume interactions which arise as a consequence of Pauli's exclusion principle and forbid overlap between two particles, and electrostatic interactions occurring when the particles carry net surface charge. The effects of excluded volume, or hard, interactions on phase behavior can most easily be altered by changing the shape of the particles, since the change in geometry of the basic building blocks will change the geometry of the obtainable larger scale structure as well. The importance of systems interacting solely through excluded volume interactions lies in the fact that their equilibrium phase behavior depends on a single parameter - the density of the system. This provides a model system with a well defined behavior control parameter. The effects of charge are most commonly modeled by the screened Coulomb, i.e. repulsive Yukawa, pair potential which can also include hard-core repulsion. Altering the electrostatic interactions by effectively changing the screening length and the contact value of the colloid pair potential can be achieved in experiments by adding salt to the solution. In this thesis, we use computer simulations to study colloidal systems composed of particles interacting both via hard-core and repulsive Yukawa interactions.

1.2 Simulation methods

The two most widely used simulation approaches for studying the behavior of colloidal systems are molecular dynamics (MD) and Monte Carlo (MC) techniques. They were both first introduced in the 1950s [6, 7] and since then they have been used to study a multitude of problems ranging from general data analysis to predicting the properties of materials [8]. Both MC and MD simulation techniques aim to explore the phase space, albeit in different ways, of the system of interest and with it to provide information on the relevant variables. However, since the two simulation methods are, by design, different and better suited for different applications we make use of both depending on the specifics of the problem we wish to study.

1.2.1 Monte Carlo simulations

The total energy of an isolated system consisting of N particles confined to a volume V and at temperature T is given by the Hamiltonian $\mathcal{H}(\mathbf{r}^N, \mathbf{p}^N) = \mathcal{K}(\mathbf{r}^N, \mathbf{p}^N) + \mathcal{U}(\mathbf{r}^N, \mathbf{p}^N)$, where $\mathcal{K}(\mathbf{r}^N, \mathbf{p}^N)$ is the kinetic and $\mathcal{U}(\mathbf{r}^N, \mathbf{p}^N)$ the potential energy of the system, and $\mathbf{r}^N$

and $\mathbf{p}^N$ denote the sets of coordinates and momenta of the N particles. Such a system will occupy a state, defined in the phase space by the positions $\mathbf{r}^N$ and momenta $\mathbf{p}^N$, with a probability $\mathcal{P}$ proportional to the Boltzmann factor

$$\mathcal{P}(\mathbf{r}^N, \mathbf{p}^N) \propto \exp\left[-\beta\mathcal{H}(\mathbf{r}^N, \mathbf{p}^N)\right], \tag{1.1}$$

where $\beta = 1/k_B T$ and k_B is the Boltzmann constant. The canonical partition function, which counts the weighted number of states such a system can occupy, is then given by

$$Z(N, V, T) = \frac{1}{N!h^{3N}} \int\int d\mathbf{r}^N d\mathbf{p}^N \exp\left[-\beta\mathcal{H}(\mathbf{r}^N, \mathbf{p}^N)\right]. \tag{1.2}$$

The partition function can be related to the free energy which then determines the thermodynamic properties of the system.

Measuring the partition function directly in simulations turns out to be impossible, but what is possible is to calculate canonical ensemble averages of the system observables. The expectation value of a quantity $A(\mathbf{r}^N, \mathbf{p}^N)$ is given by

$$\langle A \rangle = \frac{1}{N!h^{3N}} \frac{\int\int d\mathbf{r}^N d\mathbf{p}^N A(\mathbf{r}^N, \mathbf{p}^N) \exp\left[-\beta\mathcal{H}(\mathbf{r}^N, \mathbf{p}^N)\right]}{Z}. \tag{1.3}$$

This expression can be further simplified if the quantity of interest is independent of the particle velocities and if we take into account the fact that for most systems the total energy depends on the particle momenta only through the kinetic energy term. The momentum integrals in Eq. (1.3) will cancel out giving

$$\langle A \rangle = \frac{\int d\mathbf{r}^N A(\mathbf{r}^N) \exp\left[-\beta\mathcal{U}(\mathbf{r}^N)\right]}{\int d\mathbf{r}^N \exp\left[-\beta\mathcal{U}(\mathbf{r}^N)\right]}. \tag{1.4}$$

The basic idea of the importance sampling, or Metropolis Monte Carlo, algorithm is to explore the phase space according to the canonical probability distribution and to calculate the value of $\langle A \rangle$ by only sampling the most relevant regions of the phase space. We must generate a sequence of random configurations which is sufficiently long to give reliable results, and then simply average the quantity A over the visited configurations. This sampling procedure can also be adjusted to correspond to different ensembles, i.e. not just the canonical, depending on the problem at hand. In the work described in this thesis we use two ensembles: the canonical, or constant volume (NVT) ensemble and the constant pressure (NPT) ensemble.

A Monte Carlo simulation starts from a randomly generated configuration of particles which we then evolve by attempting certain, predefined moves that depend on the ensemble used. Based on the probability distribution associated with the ensemble we then either accept or reject these moves, obtaining the next configuration. When simulating spherical particles in the NVT ensemble, for instance, the only type of trial move we employ are attempts to displace a single particle, while in the NPT ensemble we also try to change the volume of the simulation box. The volume change can be performed in such a way that the box shape remains the same (we simply scale the box dimensions) or such that we also vary the shape. Allowing the simulation box shape to vary

is especially important when we wish to study the phase behavior since it allows for the complete structural relaxation of the system. If the system we are simulating consists of anisotropic particles rotation moves have to be incorporated as well.

In this work we use Monte Carlo simulations primarily to obtain the equations of state of various dumbbell systems and the free energies of relevant crystalline phases.

1.2.2   Free energy calculations

In order to construct the phase diagram of any given system we need to determine which phases are stable and for what parameter ranges. For systems with hard-core interactions, as mentioned previously, the phase behavior is determined only by the packing fraction, or density, and hence constructing phase diagrams for this class of systems in the canonical ensemble amounts to identifying the stable phases and locating their coexistence densities.

The intuitively simplest way of studying first-order phase transitions in simulations would be to prepare the system in a state of interest and then change the temperature or pressure gradually, waiting to observe a transition. However, first-order phase transitions are usually accompanied by non-negligible hysteresis, appearing as a consequence of the large free energy barrier that separates two phases at coexistence [8]. Clearly, this would make determining the coexistence densities accurately very difficult.

A method that does not suffer from this drawback, and the one we use to determine stable solid phases in this thesis, is thermodynamic integration [9]. We cannot directly measure free energies in a simulation (for the same reason we cannot measure partition functions), but we can calculate the difference between the free energies of two different phases. If we can define a reversible path in the phase space of a system that connects it to a reference state - a path that does not involve the system crossing a first-order phase transition - we can use the thermodynamic integration method to integrate the free energy change along this path. The choice of the reference system will depend on whether a reversible path transforming this reference state to the system of interest is available, and also on whether we have a way of obtaining the free energy of the reference state. Typically, for liquid states the reference system is taken to be the ideal gas and for solids it is a non-interacting Einstein crystal with the corresponding underlying structure. Making use of the fact that the thermodynamically stable phase at a given state point in the phase space is the one with the lowest free energy at that point, together with the obtained relative free energies, allows us to construct the phase diagram.

Assuming that we have chosen a reference state (with the potential energy $\mathcal{U}_0$) and that a path exists which connects this state to the system of interest (with the potential energy $\mathcal{U}_1$), we can construct an intermediate system described by the potential energy function

$$\mathcal{U}(\lambda) = (1 - \lambda)\mathcal{U}_0 + \lambda\mathcal{U}_1. \tag{1.5}$$

Here λ represents a coupling parameter defined such that for $\lambda = 0$ we obtain the potential energy of the reference system, $\mathcal{U}_0$, and for $\lambda = 1$ we recover the potential energy of the system of interest, $\mathcal{U}_1$. The free energy F of the system of interest can then be calculated from

$$F(\lambda = 1) = F(\lambda = 0) + \int_{\lambda=0}^{\lambda=1} d\lambda \left\langle \frac{\partial \mathcal{U}(\lambda)}{\partial \lambda} \right\rangle_{\lambda}. \tag{1.6}$$

In practice, we perform a series of simulation runs for different values of the coupling parameter λ and for each of these systems (defined by their λ value) we calculate the ensemble average of the potential energy derivative with respect to λ. Finally, we numerically integrate the averaged derivatives (see Eq. (1.6)) to obtain the free energy of the system of interest at a particular state point.

1.2.3 Molecular dynamics simulations

In contrast to Monte Carlo techniques where we generate a random path through the phase space, when using the molecular dynamics method we aim to follow the natural time evolution of the trajectories of the particles which compose the system. Molecular dynamics is in its essence a numerical technique used to integrate Newton's equations of motion in small time steps. The equations of motion take into account interactions between particles, external forces acting on them and the possible constraints imposed on the system, e.g. by the presence of confining walls. The numerical method we use to calculate the trajectories of particles in this work is known as the velocity Verlet algorithm [10, 11].

In molecular dynamics we begin from a configuration of particles with randomly chosen positions and velocities, and the velocities scaled such that the system has a desired temperature. We then evolve the system in small steps by calculating the forces acting on the particles, and their new positions and velocities accordingly, at every step. The expectation value of a measurable variable $A(\mathbf{r}^{N}, \mathbf{p}^{N})$ is now calculated as a time average, i.e.

$$\langle A \rangle = \frac{1}{\tau} \int_{0}^{\tau} dt A(\mathbf{r}^{N}(t), \mathbf{p}^{N}(t)) \tag{1.7}$$

where τ denotes the length of the simulation time.

In this work we use molecular dynamics simulations primarily to study the dynamics of systems out of equilibrium.

1.2.4 Modeling hydrodynamic interactions

In order to be able to study non-equilibrium properties of a colloidal suspension, which depend both on short-time thermal Brownian motion and long-time hydrodynamic behavior of the solvent, the simulation technique we use must be able to account for both. The difficulty in accomplishing this lies in the very large difference between the time and length scales associated with mesoscopic colloidal particles and microscopic solvent particles. Hence, some kind of coarse graining of the solvent is necessary and the particular method we use in this work is the stochastic rotation dynamics (SRD) method [12, 13].

In SRD the solvent is modeled as a large number of fluid particles which are treated as point-like and allowed to move in continuous space with continuous velocities according to Newton's equations of motion. Coarse-graining is achieved by splitting the simulation box

into cells and allowing the fluid particles to interact, at discrete times, with the members of the cell they belong to. The interactions within the solvent are realized through a collision procedure which allows the particles to exchange momentum in a way that does not violate the laws of conservation of mass, momentum and energy on a local level. As long as these conservation laws are locally obeyed the simulation technique will generate the correct Navier-Stokes hydrodynamics.

In order to study a colloidal suspension the colloids must be coupled to the solvent described via SRD and this can be achieved by using a hybrid between SRD and molecular dynamics simulation techniques. More details concerning this simulation method will be given in Chapter 2.

1.3   The systems studied

The systems we study in this thesis are comprised of particles with shapes that fall into two categories. These are spherical shaped particles and dimer particles. We model colloidal spheres as almost hard particles, and in molecular dynamics simulations we describe their interactions using a steep repulsive Weeks-Chandler-Andersen type potential [14]. Dimer particles offer a large variety of shapes, depending on the sizes of the constituent spheres and their center-to-center separation. Using Monte Carlo simulations we study both tangential and non-tangential asymmetric dimers, or dumbbells, which we model as purely hard particles. The asymmetric tangential dumbbells, which we will refer to as
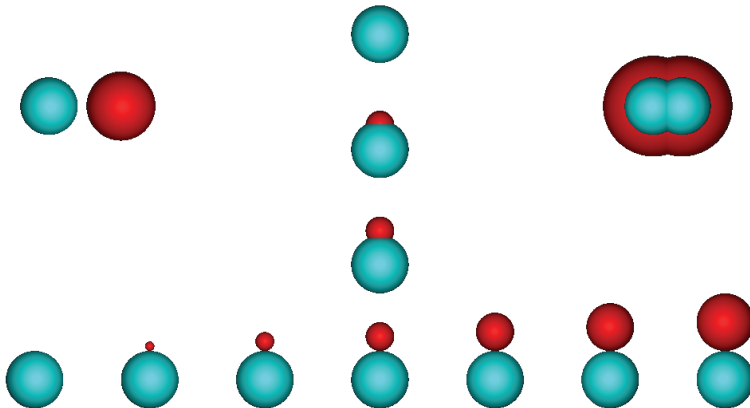

Figure 1.1: Sketch of the particle shapes studied in this thesis including spheres with a diameter ratio of 0.83 (top left), snowmen particles (bottom), anisotropic dumbbells with constituting sphere size ratio of $d = 0.5$ (middle), and Yukawa dumbbells (top right, where blue shows the hard-core and red represents the interaction range).

snowman shaped particles, consist of two spheres of different diameters D_1 and D_2 fused together at their surfaces forming a particle that can be defined solely by the ratio of the sphere diameters $d = D_1/D_2$. For non-tangential asymmetric dumbbells we choose to fix the sphere diameter ratio and vary the center-to-center separation, such that the shape of these particles ranges from a sphere to a snowman. Finally, we also study systems of dumbbell particles, comprised of non-tangential equally sized spheres, which interact via long-ranged repulsive Yukawa potentials.

A schematic representation of the particles composing the systems studied in this thesis is shown in Fig. 1.1.

1.4 Thesis outline

In this thesis we first study Rayleigh-Taylor-like instabilities in binary mixtures of hard-sphere-like colloids in Chapters 2 and 3, on both the particle scale level and also at the level of a complex fluid. Chapter 4 is dedicated to constructing the phase diagram of the snowman-shaped particles by calculating free energies of relevant crystalline phases, paying special attention to the effect of entropic degeneracy on the stabilization of predicted crystals. In Chapter 5 we investigate the phase behavior of hard non-tangential dumbbells and finally in Chapter 6 we study the phase behavior of long-ranged repulsive Yukawa dumbbells with a range of screening lengths.

2

Hydrodynamic Rayleigh-Taylor-like instabilities in sedimenting colloidal mixtures

We study the sedimentation of initially inhomogeneous distributions of binary colloidal mixtures confined to a slit using a coarse-grained hybrid molecular dynamics and stochastic rotation dynamics simulation technique. This technique allows us to take into account both Brownian motion and hydrodynamic interactions between colloidal particles in suspensions. The sedimentation of such systems results in the formation of Rayleigh-Taylor-like hydrodynamic instabilities, and here we examine the process of the formation and the evolution of the instability as well as the structural organization of the colloids, depending on the properties of the binary mixture. We find that the structural properties of the swirls that form as a consequence of the instability depend greatly on the relative magnitudes of the Peclet numbers, and much less on the composition of the mixture. We also calculate the spatial colloid velocity correlation functions which allow us to follow the time evolution of the instability and the time dependence of the characteristic correlation length.

2.1   Introduction

Binary mixtures of colloidal particles exhibit a surprisingly rich phase behavior, with a wide diversity of binary crystal structures which have been extensively studied both by experiments and computer simulations (for a review see e.g. Ref. [15]). Depending on the properties of the constituting particles and the structures they form, these systems can both have fundamentally interesting properties *and* be useful for the development and fabrication of advanced materials, such as photonic crystals [16]. Photonic crystals are materials that do not allow light propagation in all directions and are therefore potentially suitable for applications related to controlling and manipulating the propagation of light. Experimental realization of these structures on optical scales, however, is still a challenge. The two colloidal crystal structures that would potentially have a large band gap in the visible region are the diamond [17, 18] and pyrochlore [19, 20] structures, which are the underlying lattices of one of the binary Laves phases [21]. This inspired a recently proposed fabrication method that involved using external fields to facilitate the self-assembly of a hard-sphere binary Laves phase, followed by the burning or dissolving of one of the colloidal species which would result in the desired structure [22]. The stability of these binary crystalline structures in hard-sphere mixtures has been investigated using computer simulations, where Gibbs free energy calculations showed that for diameter ratios in the range of $0.74 \leq q \leq 0.84$ Laves phases are stable [22, 23]. However, while Laves phases have been so far experimentally observed in nanoparticle systems [24] and some colloidal systems [25, 26], they have not yet been fabricated for hard-sphere mixtures. The main issue lies in the fact that for micro-meter-sized colloids, which would be needed for obtaining a band gap in the visible region, gravity and slow crystallization rates hinder the formation of binary crystals [27]. With photonic applications in mind, fabrication of a binary Laves phase was attempted through the sedimentation of colloids [28] and it was observed that sedimentation starting from a vertically inhomogeneous distribution of particles (i.e. particles arranged on the upper capillary wall) leads to the development of inhomogeneities in the plane perpendicular to the gravitational field. The experiments also showed that when the sediment formed on the bottom wall, instead of forming the desired binary crystal structure, the particles of different species had become separated. However, whether this separation was a direct consequence of the observed horizontal density inhomogeneities is unclear, and it would therefore be desirable to study this process at the particle level.

In order to investigate the interplay between mixing and separation we simulate the sedimentation of binary colloidal systems immersed in a solvent and confined to a slit. The simulations start by mimicking a frequently used experimental setup - an initially homogenized dispersion is left to sediment to the bottom of the slit so that when the sediment is equilibrated, the slit is turned upside down leaving a heavy colloid-fluid layer superimposed on top of a lighter fluid one. Sedimentation of a configuration obtained in this way is accompanied by the formation of strong inhomogeneities, inducing lateral pattern formation, which resemble the hydrodynamic Rayleigh-Taylor instability. Instabilities arising due to unstable density distributions have been previously studied in different contexts [29, 30, 31]. For a one-component system of sterically-stabilized spherical colloids sedimenting in a slit, experimental observations of the Rayleigh-Taylor instability

have been reported previously by Royall *et al.* [32], and have also been studied via computer simulations by Padding and Louis [33] and Wysocki *et al.* [34, 35], who modeled the colloids as hard spheres.

The classic Rayleigh-Taylor instability occurs if a layer of a heavy fluid is placed on top of a lighter one [36]. The system will tend to minimize its potential energy, i.e. to reverse the positions of the fluids and during this process the interface that separates them will start to fluctuate. The growth of the unstable fluctuations results in the formation of the Rayleigh-Taylor instability.

The formation of the instability is driven by the gravitational field, and in our simulations the strength of the field acting on particles of one species is characterized by their Peclet number. Peclet numbers can be chosen independently for each of the species in the binary mixture. The limit in which $Pe \gg 1$ marks the granular domain where the effects of diffusion are small, while for $Pe \ll 1$, which is the case for relatively small colloids, diffusion dominates. In Ref. [37] Padding and Louis showed that for steady state sedimentation and intermediate values of Pe numbers ($Pe = 0.1 - 15$) the average sedimentation velocity of hard-spheres is completely dominated by the hydrodynamic interactions and depends little on the exact value of the Peclet number. When simulating instabilities, which occur in non-equilibrium, along with Brownian fluctuations, computer simulations need to properly include hydrodynamic interactions mediated by the solvent [38].

The simulation technique that we use in our study, since it captures both of these effects, is a coarse-grained hybrid molecular dynamics (MD) and stochastic rotation dynamics (SRD) scheme. It was first introduced by Malevanets and Kapral [12, 13], and has been used to study colloids [37, 39, 40, 41, 42], polymers [43, 44, 45] and vesicles and cells [46, 47, 48]. As mentioned above, it has also been used to simulate the Rayleigh-Taylor-like instability of a one-component colloidal system in Refs. [33, 34, 35].

Our goal in this work is to gain a detailed insight into how the properties of the binary mixtures and the constituting particles influence the formation and the time development of the Rayleigh-Taylor-like instabilities, and to investigate the potential for controlling the organization of particle species during the sedimentation.

2.2   Model

Bridging the different time and length scales between colloidal particles and a solvent in computer simulations requires coarse-graining. To this end, we employ stochastic rotation dynamics to describe the hydrodynamic interactions between colloids mediated by the solvent. Below we briefly outline the method and refer the interested reader to Ref. [49] for more technical details and also a discussion of other simulation techniques designed to describe the dynamics of colloidal suspensions.

SRD is a coarse-graining scheme that models the solvent as a large number, N_f, of point-like fluid particles, each of mass m_f, that are free to move in continuous space with continuous velocities. The system, i.e. the simulation box, is coarse-grained into cubic cells of size a_0 so that when the fluid particles interact they do so only with the members of their own cell. There is no restriction on the number of fluid particles in a cell.

The dynamics of the solvent is conducted in two steps: streaming and collision. In

the streaming step we integrate Newton's equations of motion for the solvent particles for a time Δt_c. The forces acting on fluid particles are external and are generated by the colloids, gravity and the walls.

In the collision step, particles are sorted into cubic cells and their velocities relative to the center of mass velocity $\mathbf{v}_{cm}$ of the cell they belong to are rotated, i.e

$$\mathbf{v}_i \mapsto \mathbf{v}_{cm} + \mathbf{R}(\mathbf{v}_i - \mathbf{v}_{cm}). \tag{2.1}$$

$\mathbf{R}$ is a rotation matrix that rotates the relative velocities by a fixed angle α about a random axis. We set $\alpha = \pi/2$ in all our simulations. The purpose of the collision step is to allow the solvent particles to exchange momenta while conserving mass, momentum and kinetic energy in the cell. The transformation we describe does indeed conserve these properties, leading to correct hydrodynamics [12]. To ensure Galilean invariance, we include a grid shift procedure that shifts the fluid particles by a random vector before performing the collision step [50]. By choosing the shift vector randomly, we make sure that the local environment of each fluid particle, i.e. the SRD cell it belongs to, does not stay the same over multiple collision steps, and in this way we avoid the velocity field developing anomalies [50].

Hard-sphere-like colloids are propagated through a molecular dynamics scheme and their coupling to the SRD bath is carried out via a repulsive interaction potential of the Weeks-Chandler-Andersen form

$$\phi_{fi}(r) = \begin{cases} 4\epsilon \left[\left(\dfrac{\sigma_{fi}}{r}\right)^{12} - \left(\dfrac{\sigma_{fi}}{r}\right)^{6} + \dfrac{1}{4} \right] & (r \leq 2^{1/6}\sigma_{fi}), \\ 0 & (r > 2^{1/6}\sigma_{fi}), \end{cases} \tag{2.2}$$

where $i = A, B$ denotes the colloidal species A or B, f denotes the solvent (fluid) particles, r is the separation between a colloid and a fluid particle and σ_{fi} is the colloid-fluid interaction range for species i.

The interaction between the colloids is represented by a similar, but steeper repulsive potential which takes the form

$$\phi_{ij}(r) = \begin{cases} 4\epsilon \left[\left(\dfrac{\sigma_{ij}}{r}\right)^{48} - \left(\dfrac{\sigma_{ij}}{r}\right)^{24} + \dfrac{1}{4} \right] & (r \leq 2^{1/24}\sigma_{ij}), \\ 0 & (r > 2^{1/24}\sigma_{ij}), \end{cases} \tag{2.3}$$

where $i, j = A, B$, r denotes the separation between two colloidal particles and σ_{ij} is the colloid-colloid interaction range between species i and j, given as σ_{AA}, σ_{BB} or $\sigma_{AB} = (\sigma_{AA} + \sigma_{BB})/2$. The colloid-fluid and colloid-colloid energy scales are set by ϵ. We integrate colloid-fluid and colloid-colloid forces using a velocity Verlet algorithm [8] with time step $\Delta t_{MD} = \Delta t_c/4$.

The number of fluid particles is much larger than the number of colloids, which can lead to the appearance of unwanted depletion forces between the colloidal particles. Even a slight overlap between two colloids introduces strong attractions. In order to avoid this, we set particle diameters σ_{AA} and σ_{BB} to values larger than $2\sigma_{fA}$ and $2\sigma_{fB}$ respectively, and introduce an additional depletion compensating potential between the colloids to

deal with the rare cases when they are closer then $2\sigma_{fi}$ ($i = A, B$). For purely hard-sphere interactions the depletion potential can be calculated analytically. However, the repulsive interactions given in Eqs. (2.2) and (2.3) are slightly softer. The depletion force F_d arising due to these potentials has been calculated numerically by Padding and Louis who found that it fits well with a slightly altered form of the hard-sphere result [49]. The compensating force F_c is given by $F_c(r) = -F_d(r) = n_f k_B T \sigma_{fi}^2 \ 0.85[4 - (r/(1.05\sigma_{fi}))^2]$, where r is the distance between two colloids, n_f is the number density of fluid particles, and we take $k_B T$ to be 1. The compensating potential acts for particle separations $r < 2.1\sigma_{fi}$ with $i = A, B$.

Additionally, since the systems we simulate are out of equilibrium we must couple them to a thermostat to keep the temperature constant. We do this by defining a global temperature based on the mean square deviations of the fluid particle velocities from their respective center of mass velocities of the cells they belong to. We measure the global temperature every Δt_c and then rescale the relative fluid particle velocities to get the correct temperature [49].

In summary, the hybrid MD and SRD simulation proceeds as follows. We begin by initializing the system – we place colloid and fluid particles randomly in the simulation box, such that they do not overlap, and assign random velocities to all of the particles. As an illustration, in Fig. 2.1 we show a schematic of the simulation box containing colloids and fluid particles together with the cell grid. Next we calculate the forces acting on both the colloids and the fluid particles, with the colloids feeling the presence of all other colloids and the fluid particles, and the fluid only feeling the presence of the colloids. Using the velocity Verlet algorithm we integrate colloid-fluid and colloid-colloid forces and evolve the system for time Δt_{MD} by calculating the new velocities and positions of all the particles. This recalculation of all the particle positions and velocities is performed for every iteration for the duration of the simulation run. In addition, every $\Delta t_c = 4\Delta t_{MD}$ the evolution of the system is interrupted in order to perform the SRD collision step in which only the fluid particles' velocities are altered (see Eq. (2.1)), and the temperature of the system is adjusted via the thermostat. The MD simulation is then resumed and the system evolves as described above until the next SRD collision step is scheduled.
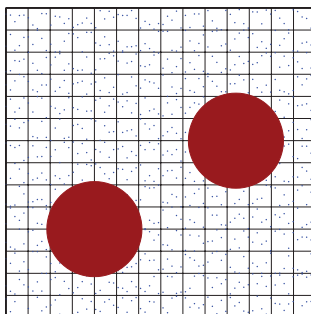

Figure 2.1: Schematic of the simulation box with colloids (red circles) and fluid particles (dark blue dots). Also shown is the cell grid of dimension a_0.

2.3   Results

We consider binary mixtures of small and large hard-sphere like colloidal particles with diameters σ_{fA} and σ_{fB}, where $\sigma_{fA}/\sigma_{fB} = 0.83$. We choose this particle diameter ratio as it is close to the size ratio of hard spheres forming a binary Laves phase with the highest maximum packing fraction [23]. The mixtures we study have two different compositions. One consists of $N_A = 6500$ and $N_B = 3250$ colloids forming a system with twice as many small particles as large ones (which is the particle number ratio of a binary Laves phase) and in this case the volume fractions of the two species are roughly equal. The other mixture consists of $N_A = N_B = 6500$ colloidal particles. In both cases the colloids are immersed in a bath of $N_f \sim 15 \cdot 10^6$ solvent particles. We set $\sigma_{fA} = 2a_0$ and $\sigma_{AA} = 4.3a_0$ as in Ref. [49], and with this we also determine $\sigma_{fB} = 2.4a_0$ and $\sigma_{BB} = 5.16a_0$. The particles are confined between two walls in xy planes and we impose periodic boundary conditions in the x and y directions with gravity acting in the z direction. The dimensions of the slit are $L_z = 72a_0$, $L_x = L_y = 216a_0$ (giving $L_z = 14\sigma_{BB}$, $L_x = L_y = 42\sigma_{BB}$ or $L_z = 17\sigma_{AA}$, $L_x = L_y = 51\sigma_{AA}$) which are close to the dimensions of the experimental setup for a one-component system presented in Ref. [35]. The average number of fluid particles per SRD cell was set to $\gamma = 5$.

We characterize the motion of a colloid by the Peclet number, $Pe = \tau_D/t_S$, which is the ratio between the time τ_D a particle needs to diffuse over its own radius a, and the Stokes time, t_S, it needs to sediment over the same distance

$$t_S = \frac{a}{v_S}, \tag{2.4}$$

where v_S is the flow velocity. The Peclet number can be calculated as

$$Pe = \frac{M_b g a}{k_B T} = \frac{4\pi}{3} \frac{(\rho_c - \rho_f) g a^4}{k_B T}, \tag{2.5}$$

where M_b denotes the buoyant mass of a particle, $M_b = \frac{4}{3}\pi(\rho_c - \rho_f)a^3$, ρ_c and ρ_f are the mass densities of a colloidal particle and the fluid respectively, g denotes the gravitational constant and a the effective hydrodynamic radius of the particle, determining the characteristic length scale [49]. With the average number of fluid particles per SRD cell fixed to $\gamma = 5$, and taking the mass of a fluid particle, m_f, as the unit of mass, and the dimension of the cell, a_0, as the unit of length in our simulations, the mass density of the fluid is fixed at $\rho_f = 5$ in simulation units. A detailed discussion on how to map the parameters of this simulation method onto physical systems is given in Ref. [49]. For each system that we study we set the Peclet numbers of each of the species, Pe_A and Pe_B, independently, and we also fix the mass of the particles of species A to $M_A = 125$ in simulation units [49]. By doing so, we determine the strength of the gravitational field and the mass of the particles of species B. We have chosen to keep Pe_B at 12 and vary Pe_A by setting it to $6, 9, 12, 15$ and 18. We note that as the particles in this study have fixed sizes, the relative Peclet number Pe_A/Pe_B is proportional to the ratio of the effective densities of the two particle species $(\rho_A - \rho_f)/(\rho_B - \rho_f)$.

2.3.1 Rayleigh-Taylor-like instability

We let an initially homogeneous distribution of colloids confined to a slit sediment towards one wall until the system reaches an equilibrium distribution. This is checked by monitoring colloidal density profiles in time. Once the particles have settled at the bottom wall of the simulation box we invert the direction of gravity, creating conditions suitable for the instability to develop. We let the system evolve further and, as a consequence of the instability, droplets of colloidal material form and sediment quickly towards the bottom wall. In this section we examine the structural properties of these droplets and their dependence on the composition of the mixture and the properties of the colloidal particles − specifically the Peclet numbers.

Figure 2.2 shows the evolution of the systems with $N_A = 2N_B$ (left column) and $N_A = N_B$ particles (right column) and Peclet numbers $Pe_A = Pe_B = 12$. We see that the process of sedimentation is accompanied by the formation of swirls. Initially, the interface separating the colloid-rich region from the pure solvent region is almost flat, then undulations start to form and as their amplitude grows the colloidal layer resolves itself into droplets. This is a consequence of the instability - it facilitates the fluid back-flow and the transition of the system to a stable configuration via the instability. We note that

$\downarrow g$

$N_A = 2N_B$ $\qquad\qquad$ $N_A = N_B$
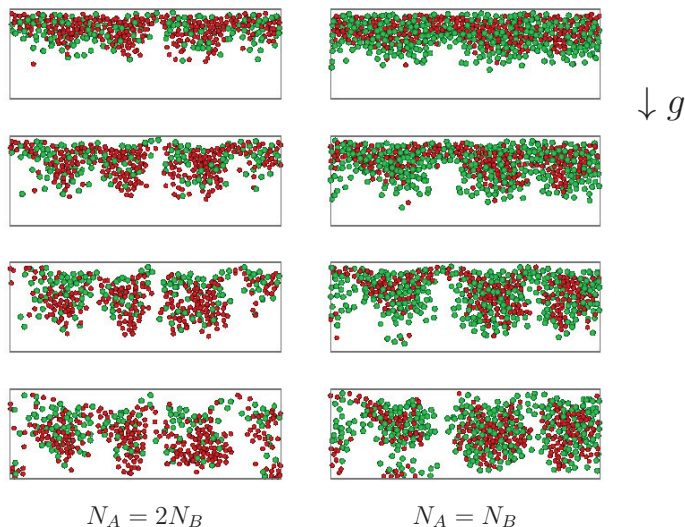
Figure 2.2: Simulation snapshots showing the time evolution (from top to bottom) of the Rayleigh-Taylor-like instability in binary mixtures of hard-sphere-like colloids with size ratio $\sigma_{fA}/\sigma_{fB} = 0.83$. Mixtures consist of $N_A = 2N_B$ (left column) and $N_A = N_B$ (right column) colloids with the same Peclet numbers $Pe_A = Pe_B = 12$. The snapshots are slices of thickness $2\sigma_{BB}$ in the vertical (xz) plane in the middle of the simulation box; gravity acts in the direction indicated in the figure (z direction). Particles belonging to species A (smaller) are colored red and particles belonging to species B (larger) are green.

the swirls we can see in Fig. 2.2 are very similar to those observed for a one-component system in Ref. [33].

The added complexity of a binary mixture, however, provides for the possibility of different arrangements of colloidal particles of different species within the droplets themselves. In Fig. 2.3 we show the density profiles of each of the particle species as well as the overall colloid density profile for mixtures with $N_A = N_B$ and different relative Peclet numbers of the particle species: $Pe_A = 6$ and $Pe_B = 12$ (left column) and $Pe_A = 18$ and $Pe_B = 12$ (right column). We plot the density profiles against the height of the simulation box, at the start of the sedimentation process (Fig. 2.3a, 2.3b), at a time when the instability is fully developed (Fig. 2.3e, 2.3f) and a time in between the two (Fig. 2.3c, 2.3d). Comparing Fig. 2.3a and Fig. 2.3b we can see that initially the overall density profiles are not, qualitatively, significantly different. However, we do observe significant differences between the mixtures if we look at the distributions of individual species within the simulation box. While the shape of the distributions in the case when the Peclet
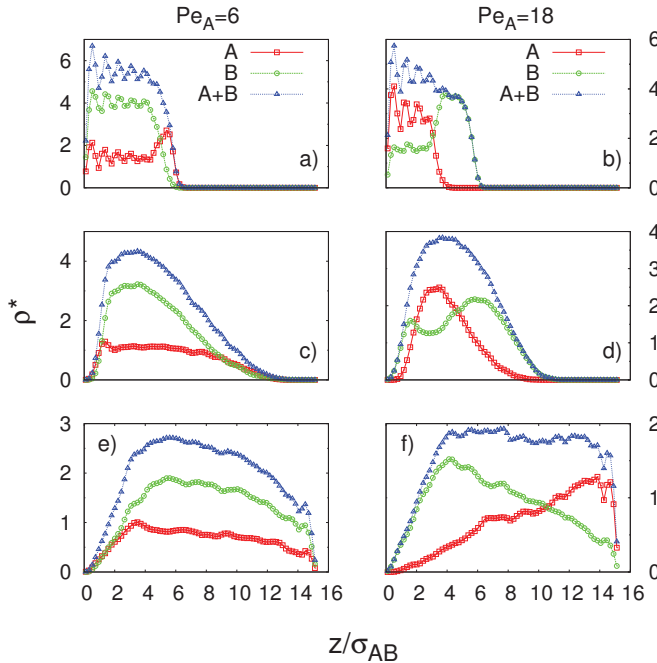
Figure 2.3: Colloid density profiles as a function of height of the simulation box at three different times increasing from top to bottom, where top corresponds to initial times, bottom to times when the instability is fully developed. Plots shown here correspond to mixtures with $N_A = N_B$, $Pe_B = 12$ and: $Pe_A = 6$ for the plots in the left column (species A is lighter in this case) and $Pe_A = 18$ for the plots in the right column (species A is heavier). Density is given as $\rho* = \rho(a_0^3/m_f)$ and the distances are rescaled by $\sigma_{AB} = (\sigma_{fA} + \sigma_{fB})/2$.

number of smaller particles is smaller indicates a degree of mixing (Fig. 2.3a), when the Peclet number of smaller particles is larger we can clearly distinguish between two layers - one composed of the heavier particles near the wall and one with lighter ones mostly further away (Fig. 2.3b). At later times we again see that for the mixture in which the smaller particles are lighter (Fig. 2.3c, 2.3e) the relative density of the particle species, and hence the number ratio as well, is similar at all heights. Hence, we find that the system remains more mixed when the mass density of the smaller particles is smaller than the density of the larger particles, compared to the case when the smaller particles are heavier (Fig. 2.3d, 2.3f) where we find different degrees of mixing as a function of height. Clearly, depending on the relative magnitudes of the Peclet numbers the distributions of the colloidal particles will progress in different ways within the instability.

To examine the behavior within the horizontal planes, in Fig. 2.4 we present a series of simulation snapshots of a slice of the simulation box in the plane perpendicular to the direction of gravity, as the instability develops in time. Figure 2.4 allows us to look closer at the time development of network-like structures that appear as a consequence of the Rayleigh-Taylor-like instability. The snapshots shown correspond to the systems with $N_A = 2N_B$ (Fig. 2.4a, 2.4b) and $N_A = N_B$ particles (Fig. 2.4c, 2.4d), and Peclet numbers $Pe_B = 12$ and $Pe_A = 6$ and 18, i.e. $Pe_A = 0.5Pe_B$ and $Pe_A = 1.5Pe_B$, with those corresponding to times when the swirls are fully developed highlighted.

If we compare the highlighted snapshots in Fig. 2.4a and Fig. 2.4b, or the highlighted snapshots in Fig. 2.4c and Fig. 2.4d, corresponding to systems with the same particle number ratios but different relative Peclet numbers, we can see considerable differences in the structures formed. Although there is not much difference in the characteristic dimensions of the colloid-rich regions corresponding to the network branches (assuming the same particle number ratio), the distributions of particles of different species within the branches are different. In the case when the Peclet number of the smaller species is smaller (Fig. 2.4a compared to Fig. 2.4b, or Fig. 2.4c compared to Fig. 2.4d) the colloid-rich regions appear to be composed of similar numbers of A and B particles, randomly and homogeneously scattered throughout each region. However, in the case when the Peclet number of the smaller species is larger, we see the smaller colloids positioned mostly in the inner parts of the colloid-rich regions, with the larger particles positioned more towards the boundaries of these regions. As this organization of particles can be seen in both mixtures, i.e. mixtures with different number ratios of colloidal particles, we conclude that it must be due to gravitational effects, and not the composition of the mixture.

In order to quantitatively describe the structures we observe in the simulation snapshots in Fig. 2.4, for each system we calculate the radial distribution functions $g_{ii}(r)$, $i = A, B$, in a slab of thickness $2\sigma_{BB}$ in the middle of the simulation box at a time when the instability has fully developed. In Fig. 2.5 we show the radial distribution functions for the systems with Peclet numbers $Pe_A = 6$ and $Pe_A = 18$, since these are the two extremes of the parameter range we have studied. We see that the radial distribution functions calculated for the two mixtures do not depend strongly on the composition (compare Fig. 2.5a and Fig. 2.5c or Fig. 2.5b and Fig. 2.5d), but do show different behavior with different Pe_A. In the case where $Pe_A = 6$ both $g_{AA}(r)$ and $g_{BB}(r)$ curves exhibit second peaks, which for the larger species (B) are slightly more pronounced, and for the smaller species (A) are positioned at distances slightly larger than $r = 2\sigma_{AA}$. In

a) $N_A = 2N_B$ $Pe_A = 6$

$t = 12t_S$ $t = 16.5t_S$ $t = 21t_S$ $t = 35t_S$

b) $N_A = 2N_B$ $Pe_A = 18$

$t = 7t_S$ $t = 9.5t_S$ $t = 12t_S$ $t = 19t_S$

c) $N_A = N_B$ $Pe_A = 6$

$t = 14t_S$ $t = 18.5t_S$ $t = 23t_S$ $t = 37t_S$

d) $N_A = N_B$ $Pe_A = 18$

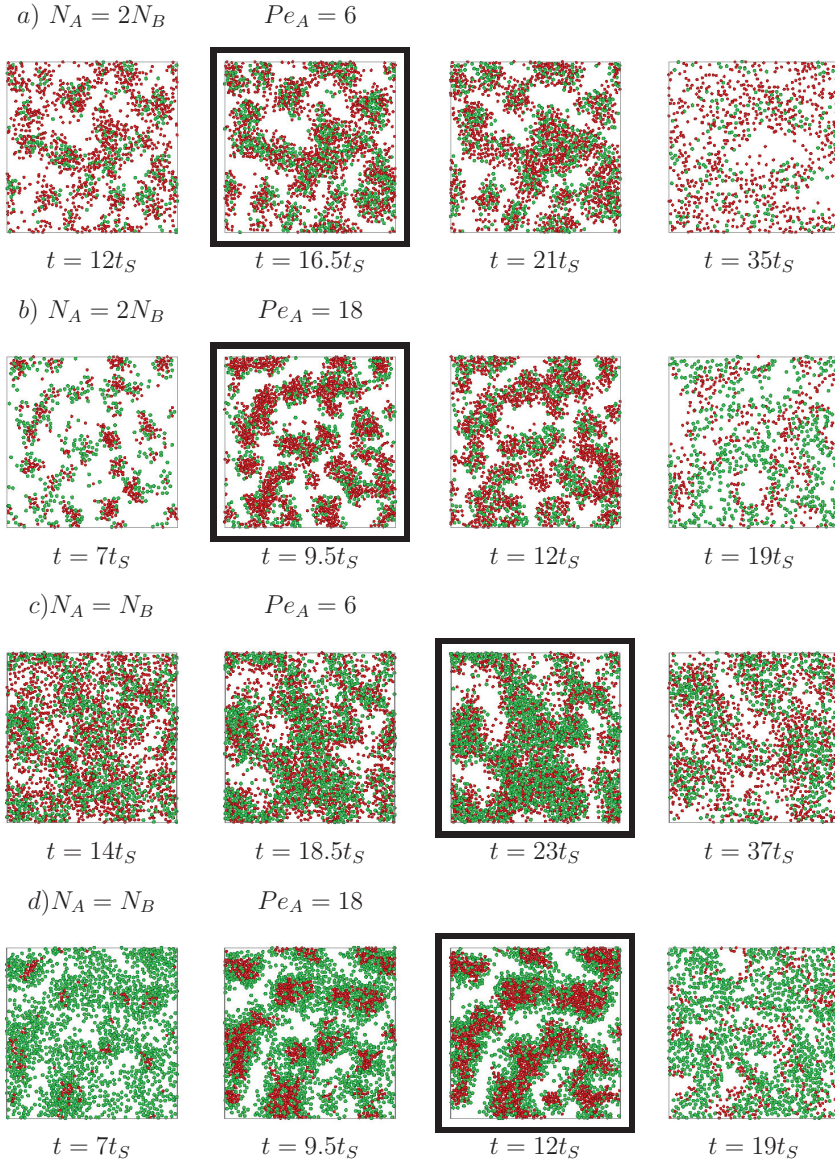$t = 7t_S$ $t = 9.5t_S$ $t = 12t_S$ $t = 19t_S$

Figure 2.4: Simulation snapshots of the time evolution (from left to right) of binary mixtures of hard-sphere-like colloids with size ratio $\sigma_{fA}/\sigma_{fB} = 0.83$, particle numbers N_A and N_B, Peclet numbers $Pe_B = 12$ and $Pe_A = 6$ and $Pe_A = 18$: a) $N_A = 2N_B$, $Pe_A = 6$; b) $N_A = 2N_B$, $Pe_A = 18$; c) $N_A = N_B$, $Pe_A = 6$; d) $N_A = N_B$, $Pe_A = 18$. The snapshots are slices of thickness $2\sigma_{BB}$ in the xy plane in the middle of the simulation box; gravity acts in the z direction. The time is measured in units of the Stokes time t_S of the larger species. Particles belonging to species A (smaller) are colored red and particles belonging to species B (larger) are green. Highlighted snapshots correspond to times when the swirls are fully developed.

the case where $Pe_A = 18$, the curves corresponding to $g_{BB}(r)$ no longer exhibit a second
peak which suggests a larger degree of dilution of species B compared to the $Pe_A = 6$
case. The plots of the radial distribution functions of the smaller particles $g_{AA}(r)$ with
$Pe_A = 18$, show for both mixtures pronounced second peaks, which are positioned at
$r \sim 2\sigma_{AA}$, and for the mixture with $N_A = N_B$ also a very small third peak at an even
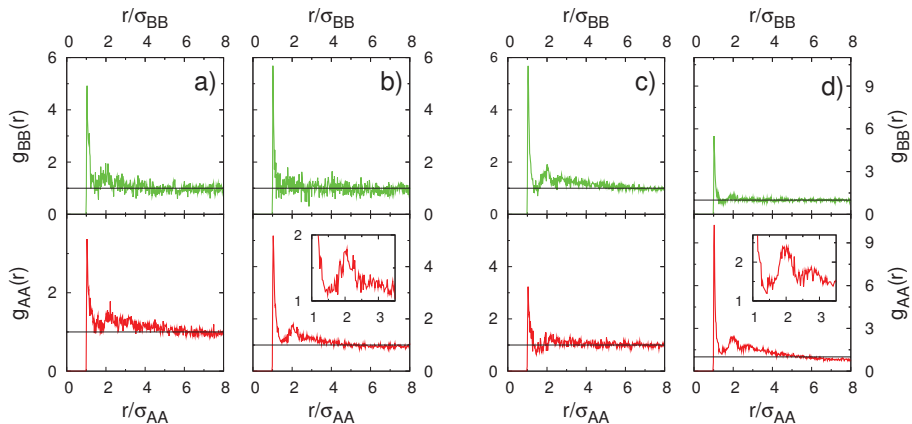larger distance (Fig. 2.5d).

Figure 2.5: Radial distribution functions $g_{ii}(r)$ with $i = A, B$ in a slab of thickness $2\sigma_{BB}$ within
the middle plane of the simulation box. $Pe_B = 12$ in all cases and a) $N_A = 2N_B$, $Pe_A = 6$; b)
$N_A = 2N_B$, $Pe_A = 18$; c) $N_A = N_B$, $Pe_A = 6$; d) $N_A = N_B$, $Pe_A = 18$. Distances are rescaled
by the appropriate particle diameters σ_{AA} or σ_{BB}. Insets show enlarged area in the region of
the second, and in d) also the third peak.

In summary, from Figs. 2.4 and 2.5 we conclude that the structure of the Rayleigh-
Taylor-like instability is hardly affected by the composition of the binary mixture, but
does depend strongly on the relative Peclet numbers of the two species. When the smaller
colloids are lighter than the larger ones ($Pe_A < Pe_B$) the density profiles indicate a higher
degree of mixing within the colloidal material than for mixtures in which the smaller
colloids are heavier ($Pe_A > Pe_B$). We would expect that, without obstacles, the heavier
colloidal species would sediment faster than the lighter species, and therefore we would
expect to see separation of colloids whenever there is a sufficient difference in colloidal mass
densities. However, larger particles will inevitably meet more resistance when propagating
through the solvent (and smaller colloids), and hence they will be slowed down, while the
smaller particles are less obstructed. Indeed, in Fig. 2.3d we see two peaks in the density
profile of the lighter, larger particles separated by a peak in the profile of the heavier,
smaller particles. This suggests that the smaller particles are penetrating the layers of
large particles, (which is in accordance with what we can see in the snapshots in Fig. 2.4)
forcing a quantity of the slower moving particles to flow up together with the solvent.
When the larger particles are heavier we see no such effect within the colloidal material
(for the parameter range studied here), with the density profiles of both species instead

progressing in a very similar fashion. Therefore it would seem that to encourage mixing of particles during sedimentation it would be preferable to have the smaller particles in the mixture with relatively smaller Peclet numbers.

2.3.2 Time correlation functions

Having examined the structural properties of the system, we next consider the dynamics of the instability formation process. We calculate the spatial correlations of colloid-velocity fluctuations in the gravity direction within the plane perpendicular to gravity. The correlation functions for the z component are calculated as

$$\frac{C_{ij}(z,r,t)}{k_B T/M_{ij}} = \langle \delta V_m(z,0,t)\delta V_n(z,r,t)\rangle, \tag{2.6}$$

with $i,j = A,B$. Here $\delta V_m(z,r,t)$ denotes the deviation of the velocity of particle m, given by $v_m(z,r,t)$, from the mean velocity in the xy plane located at height $z = L_z/2$, given by $\langle v(z,t)\rangle$, at distance r within the xy plane and at time t, i.e. $\delta V_m(z,r,t) = v_m(z,r,t) - \langle v(z,t)\rangle$. We rescale the correlation functions by the corresponding thermal fluctuation strength $k_B T/M_{ij}$, where $M_{AA} = M_A$, $M_{BB} = M_B$ and $M_{AB} = \sqrt{M_A M_B}$, with M_A and M_B the masses of species A and B respectively.

The velocity correlations develop in time in such a way that we see pronounced positive correlations at short distances and anti-correlations at larger distances followed by a final decay to 0. The anti-correlation reaching its maximum is an indication that the swirls are fully developed and the distance r at which this occurs is related to the characteristic length of the network-like structure formed. As an illustration of the described behavior,
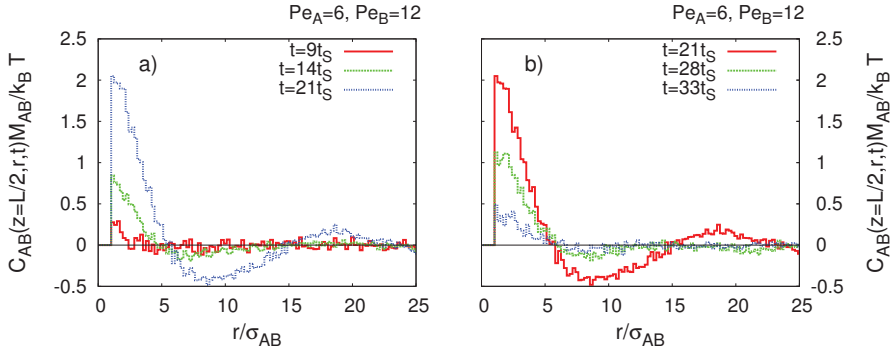
Figure 2.6: The time evolution of the r dependence of the spatial velocity correlation functions $C_{AB}(z,r,t)$ for the mixture with $N_A = 2N_B$ particles and Peclet numbers $Pe_A = 6$ and $Pe_B = 12$: a) before the anti-correlation reaches its maximum and b) after the anti-correlation has reached the maximum. The velocity correlations were calculated in the xy plane located at $z = L_z/2$ and rescaled by the thermal fluctuation strength $k_B T/M_{AB}$. The distance r is rescaled by $\sigma_{AB} = (\sigma_{fA} + \sigma_{fB})/2$, and the time t is measured in the units of Stokes time t_S of the larger species.

in Fig. 2.6 we show the r dependence of the $C_{AB}(z, r, t)$ correlation functions for one of the systems studied ($N_A = 2N_B$, $Pe_A = 6$, $Pe_B = 12$) at different times before and after the anti-correlation has reached its maximum.

The results of the calculations of the velocity correlation functions are shown in Figs. 2.7 and 2.8 where we can see the time development of the logarithm of the absolute value of $C_{ij}(z, r, t)$ for the mixtures with $N_A = 2N_B$ (Fig. 2.7) and $N_A = N_B$

Figure 2.7: Spatial velocity correlation functions $C_{ij}(z, r, t)$ for a binary mixture with $N_A = 2N_B$. The time evolution of the logarithm of the absolute value of the spatial velocity correlation function $C_{ij}(z, r, t)$, where $ij = AA, AB$ or BB, is plotted for the systems with $Pe_B = 12$ and $Pe_A = 6, 12, 18$. The correlation functions were calculated in the xy plane at $z = L_z/2$, and rescaled by the thermal fluctuation strengths $k_B T/M_{ij}$. Distances r are rescaled by σ, where $\sigma = \sigma_{fA}$ when $ij = AA$, $\sigma = \sigma_{fB}$ when $ij = BB$, or $\sigma = (\sigma_{fA} + \sigma_{fB})/2$ when $ij = AB$, and the time t is rescaled by the Stokes time t_S of species B.
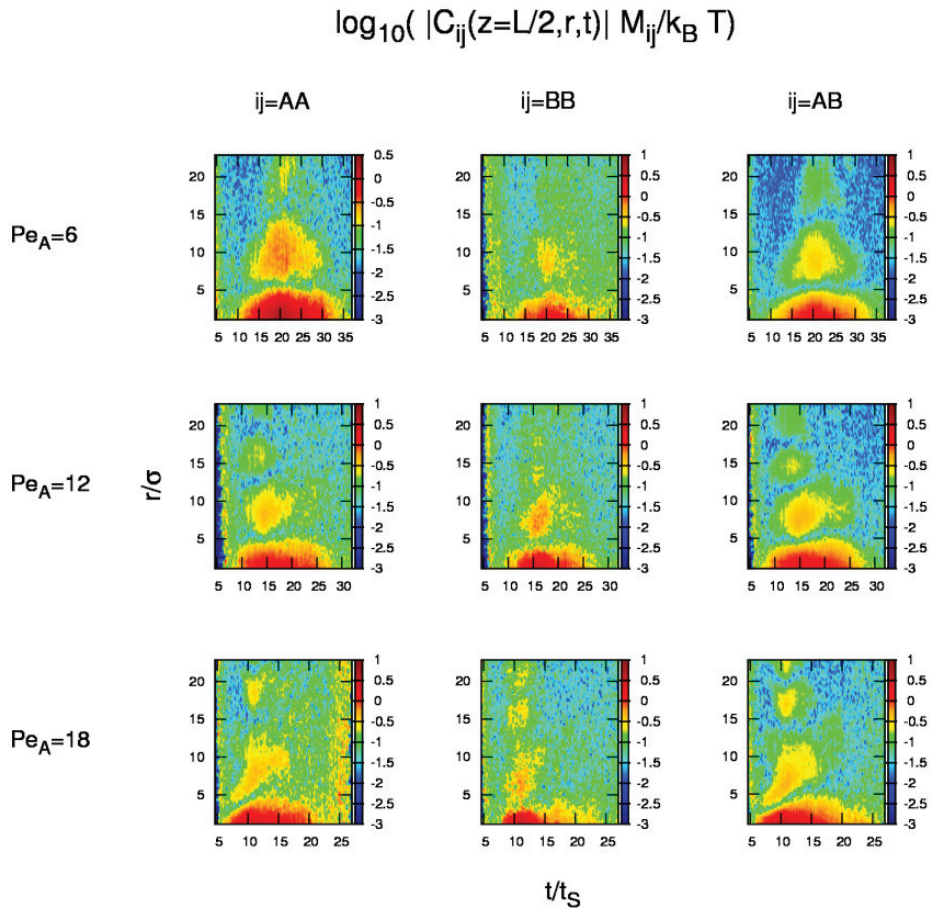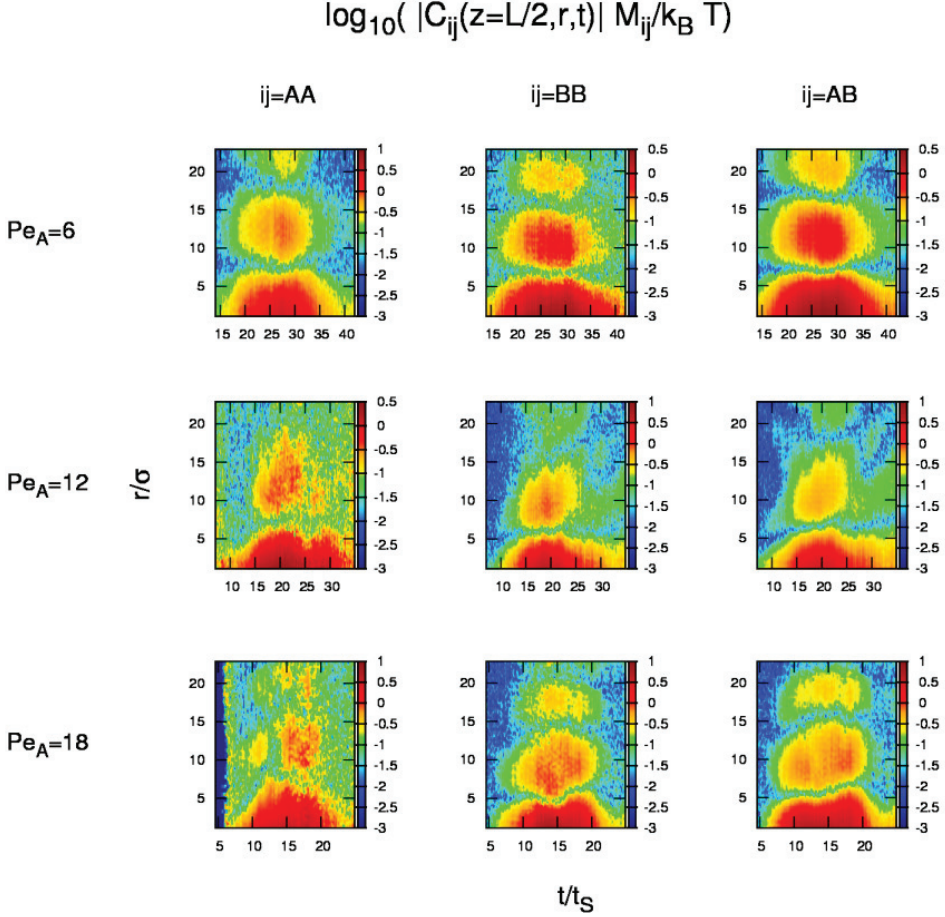
Figure 2.8: Spatial velocity correlation functions $C_{ij}(z, r, t)$ for a binary mixture with $N_A = N_B$. The time evolution of the logarithm of the absolute value of the spatial velocity correlation function $C_{ij}(z, r, t)$, where $ij = AA, AB$ or BB, is plotted for the systems with $Pe_B = 12$ and $Pe_A = 6, 12, 18$. The correlation functions were calculated in the xy plane at $z = L_z/2$, and rescaled by the thermal fluctuation strengths $k_B T/M_{ij}$. Distances r are rescaled by σ, where $\sigma = \sigma_{fA}$ when $ij = AA$, $\sigma = \sigma_{fB}$ when $ij = BB$, or $\sigma = (\sigma_{fA} + \sigma_{fB})/2$ when $ij = AB$, and the time t is rescaled by the Stokes time t_S of species B.

(Fig. 2.8), and Peclet numbers $Pe_A = 6, 12$ and 18, calculated at height $z = L_z/2$. These plots allow us to follow the evolution of the instability by following the time dependence of the characteristic length scale over which the particles are correlated. Looking at larger lengths, we see a second and sometimes even a third distance region where the particles are also strongly correlated.

As the sedimentation of the system progresses, we can see that the length over which
the particles are correlated grows at first for all systems studied. Figures 2.7 and 2.8 show
that initially this growth is monotonic in time until the characteristic length reaches a
maximum, after which, depending on the Peclet numbers of the particles, it either de-
creases monotonically or drops slightly before it increases again to a value higher than the
first one. This non-monotonic behavior of the characteristic length scale, accompanied by
the growing characteristic distances at which the second peaks of the correlation functions
appear, is observed for higher Peclet numbers.

We also note that the plots presented in Figs. 2.7 and 2.8 show that the length over
which particle velocities are correlated is larger for the denser system (i.e. the system
with more particles - $N_A = N_B = 6500$). This is in accordance with what we also observe
in Fig. 2.4.

2.4   Conclusions

Using a computer simulation technique that incorporates both long ranged hydrodynamic
interactions between particles and Brownian forces acting on them, we have studied the
sedimentation of binary mixtures of hard sphere-like colloids confined to a slit on the
particle-scale level. Initial configurations which are vertically inhomogeneous in such a way
that a heavier colloid-fluid layer is placed above a lighter one are not stable with respect
to gravity and hence their evolution results in the formation of a Rayleigh-Taylor-like
instability. In this work, we have investigated the effects of changing the strength of the
gravitational drive of one of the species, by changing its Peclet number, on the formation
and development of the instability, and on the properties of the transient network-like
structures that form during the sedimentation. By keeping the Peclet number of the
larger particles fixed and changing that of the smaller particles we have simulated a range
of relative Peclet number scenarios for two different mixtures.

We find that the organization of the particles within the droplets formed during the
sedimentation depends substantially on the relative Peclet numbers and less so on the
composition of the mixture. For mixtures in which the smaller particles have relatively
larger Peclet numbers, dense droplets, with smaller particles mostly on the inside and
larger particles mostly on the outside, form. For mixtures in which the smaller particles
have relatively smaller Peclet numbers we again see the formation of droplets, but without
any specific organization of particles within them. Our results indicate that when the
smaller particles have larger Peclet numbers, they cluster within the instability in order
to facilitate forcing their way through the lower layers of the suspension, causing a back-
flow of larger colloids together with the solvent. Therefore, to maintain a mixed sample
throughout the sedimentation process it would be desirable to have the smaller colloids
with a lower particle density.

The calculations of the spatial velocity correlation functions allow us to follow the
development of the instability in time by following the changes of the length scale over
which the particle velocities are correlated. As the instability develops, the correlation
length increases showing the existence of length scales over which the particle velocities
are correlated, followed by regions of anti-correlation, and then by regions of correlation

again at even larger distances. The distances at which we see anti-correlations correspond to the average distances between regions of particles moving in opposite directions, giving us an indication of the sizes of the colloid-rich droplets. Also, for larger Peclet numbers we see that the correlation lengths no longer grow monotonically and that the higher the Peclet number, the faster the development of the instability. For denser systems, i.e. more particles in the slit, we see that the characteristic dimensions of colloidal droplets made of particles with correlated velocities are larger. We also find that the second correlation regions are more pronounced for these denser systems, indicating that the droplets are more compact.

In conclusion, we find that the key parameter for the manipulation of the distribution of colloids within the Rayleigh-Taylor-like instabilities in binary colloidal mixtures is the relative magnitude of the Peclet numbers of the particle species. In an experimental system these parameters could be controlled by fabricating colloids from different materials and adjusting the solvent density.

2.5   Acknowledgments

3

Growth rates of the unstable modes of the Rayleigh-Taylor-like hydrodynamic instability

We perform a linear stability analysis of the interface undulations associated with the hydrodynamic Rayleigh-Taylor-like instability forming in the simulations described in Chapter 2. We calculate the growth rates of the unstable modes directly from the simulation data by examining the initial deformation of the interface between the colloid-rich and colloid-free regions. We also calculate the growth rates numerically using the linearized Navier-Stokes equation which describes the instability. This method requires a suitable definition of the viscosity of the binary sediment which we calculate from the packing fraction profiles obtained in the simulations. We find that the growth rates of the unstable modes calculated using the two approaches show good agreement.

3.1   Introduction

Microscopic studies of colloidal suspensions are generally aimed at gaining a fundamental understanding of the collective behavior of large particle assemblies. The nature of particle interactions, the way they influence the self-assembly processes, dynamical properties and relaxation times, as well as the potentially relevant starting setups and stages in the evolution necessary for a system to be suitable for a certain application are some of the examples of information that we generally seek to obtain on the microscopic scale.

In Chapter 2 we have studied colloidal suspensions sedimenting in a slit and found that with a specific setup, the evolution of the system always results in the formation of a Rayleigh-Taylor-like hydrodynamic instability. The classic Rayleigh-Taylor instability is a gravity induced instability of the interface separating two fluids of different densities positioned such that the heavier fluid is on top of the lighter one. We have studied the instability in colloidal systems on the single particle scale in an attempt to understand how the specific properties of the two particle species comprising the mixtures influence the instability. In this chapter we wish to turn our attention to a more coarse-grained description of the suspensions and examine the same systems describing them simply as a complex fluid, i.e. by defining the macroscopic properties typically associated with a fluid.

General treatment of a fluid with varying density and viscosity can be conducted through a formalism described in Ref. [36]. The analysis results in the linearized Navier-Stokes equation which can be used to calculate the growth rates of the unstable modes of the interface undulations. This was done in Ref. [35], where the authors performed theoretical analysis, in addition to experiments and computer simulations, on one-component colloidal systems undergoing the instability, finding good qualitative and quantitative agreement for the calculated instability growth rates. Experiments and simulations both provide detailed information on the positions of particles in time within the sample and the growth rates can be calculated based on these. The theoretical treatment requires knowledge of the density and viscosity profiles, and while the density profile of a specific system can be obtained directly from simulations or experiments, the viscosity profiles must be estimated instead.

The viscosity dependence on the particle concentration is essentially a many body problem and our estimates of it would, ideally, take into account the properties of the particles in the suspension, the effects of their collisions, hydrodynamic interactions and also random Brownian motion. As such a description, to the best of our knowledge, is not available, some kind of approximation is inevitably required. In this chapter, we take packing fraction profiles obtained from the simulations presented in Chapter 2 and based on these profiles we define an effective viscosity for each system using the viscosity description proposed in Ref. [51]. We also calculate the growth rates directly from the simulation data, by defining and following the initial regime evolution of a coarse-grained interface separating the colloid-rich (heavier) layer and the pure solvent layer. Comparing the simulation growth rates to those obtained theoretically allows us also to confirm the accuracy of the viscosity description used.

3.2   Model

The systems we study consist of binary colloidal suspensions of N_A spherical particles of
species A, with diameter σ_{AA} and density ρ_A, and N_B particles of species B, with diameter σ_{BB} and density ρ_B, immersed in a fluid. The suspensions are confined to a slit of
dimensions $L_x = L_y = 3L_z$ and we employ periodic boundary conditions in the x and y directions choosing the z direction as the direction in which gravity acts. The colloid-colloid
interactions, which are modeled as almost hard, are described by a steep Weeks-Chandler-
Andersen type potential [14] and the particles are propagated via a standard molecular
dynamics (MD) simulation scheme. To account for the hydrodynamic interactions in a
system we include point-like fluid particles and employ a stochastic rotation dynamics
method (SRD) to introduce interactions within the fluid. The simulation technique we
use is explained in more detail in Chapter 2.
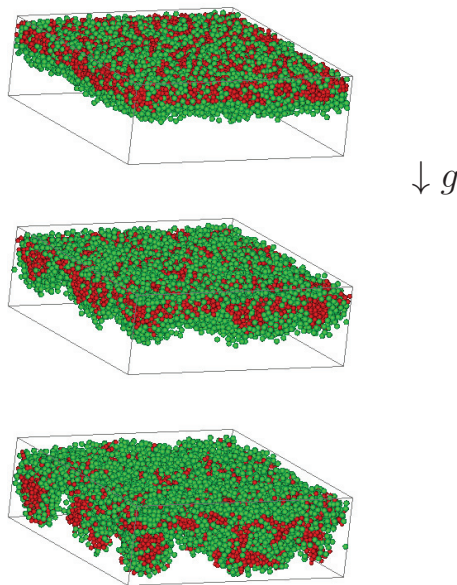
Figure 3.1: Simulation snapshots showing the time evolution (from top to bottom) of the
Rayleigh-Taylor-like instability in a binary mixture of hard-sphere-like colloids. Colloids of one
species are colored green, colloids of the other species are colored red, and the fluid is not
shown for the sake of clarity. We see that, instead of homogeneously sedimenting towards the
bottom wall of the simulation box, the particles exhibit a type of organized behavior where the
interface between the colloid-rich and the colloid-poor regions starts to undulate and deforms
progressively in time.

We start the simulations by generating a configuration of colloids homogeneously distributed within the slit and immersed in a fluid of constant density. We then let the particles sediment towards one wall of the slit, until all the colloids have settled on it and reached the equilibrium distribution. We determine this by monitoring the colloidal density profiles and when the particles have settled we invert the direction of gravity. In this way we create a configuration in which a heavier fluid layer (colloids within the solvent) is superimposed on top of a lighter one (only solvent), rendering the system unstable with respect to gravity. Finally, we allow the system to evolve, with gravity acting in the opposite direction to the initial one, and as a result the instability of the interface begins to develop.

A series of typical snapshots of the simulation box which show the system as it is experiencing the instability can be seen in Fig. 3.1.

3.3   Calculation of growth rates from theory

3.3.1   Linearized hydrodynamic equations

In order to describe the flow of a viscous fluid with varying density we start from the equation of continuity and the equation of conservation of momentum. These equations are given by

$$\frac{\partial \rho}{\partial t} + \frac{\partial}{\partial x_j}(\rho u_j) = 0, \tag{3.1}$$

and

$$\rho \frac{\partial u_i}{\partial t} + \rho u_j \frac{\partial u_i}{\partial x_j} = \rho X_i - \frac{\partial p}{\partial x_i} + \frac{\partial}{\partial x_j}\left\{\mu\left(\frac{\partial u_i}{\partial x_j} + \frac{\partial u_j}{\partial x_i}\right) - \frac{2}{3}\mu\frac{\partial u_k}{\partial x_k}\right\}. \tag{3.2}$$

Here ρ denotes the mass density of the fluid, t the time, x_i (and x_j) and u_i (and u_j) the position and the flow velocity vector components respectively ($i, j = 1, 2, 3$), p denotes the pressure, μ the viscosity and X_i is the i-th component of the resultant external force acting on the system. The equation of continuity, Eq. (3.1), accounts for the conservation of mass in a fluid since its integral form expresses the fact that the rate of change of mass in a fixed volume of fluid is given by the rate at which the fluid flows out of this volume across the boundary surface. Conservation of momentum, Eq. (3.2), in its integral form, expresses the fact that the rate of change of the momentum contained in a fixed volume of fluid is equal to the volume integral of the external forces acting on the fluid elements in this volume, plus a surface integral of the normal stresses acting on the boundary surface, minus the rate at which momentum flows out of the volume across the boundary surface. Considering the fluid as incompressible, i.e. ρ as constant, reduces the equation of continuity to

$$\frac{\partial u_i}{\partial x_i} = 0. \tag{3.3}$$

We note that for an incompressible fluid with constant viscosity μ Eq. (3.2) can be simplified to give

$$\rho \frac{\partial u_i}{\partial t} + \rho u_j \frac{\partial u_i}{\partial x_j} = \rho X_i - \frac{\partial p}{\partial x_i} + \mu \nabla^2 u_i, \tag{3.4}$$

which is the original form of the Navier-Stokes equation [36].

When studying the stability of a system our goal is to determine how it will respond to a small disturbance applied to it while it is in a stationary state. We characterize the fluid as stable with respect to those modes of disturbance which decay in time and unstable with respect to those which do not decay but keep growing in amplitude such that the system never returns to its initial state. A system that is unstable with respect to even one mode of disturbance is characterized as unstable and hence, for a general stability analysis, we need to be able to analyze the stability of a system with respect to an arbitrary disturbance.

To do so, we follow the standard analysis given in Ref. [36] and start by applying infinitesimally small perturbations to the variables describing the system. In the systems of interest in this work, these variables are the density, the pressure and the components of the velocity field. Taking the perturbations into account and simplifying Eqs. (3.1) and (3.2), while keeping only the terms linear in the infinitesimal increments, we obtain the linear equations which the perturbations must satisfy. We then analyze the perturbations into complete sets of normal modes, the functional form of which will depend on the properties of the particular system we wish to study. The geometry of the problem we are focusing on here suggests that the density and the viscosity will depend only on the z coordinate - the system is effectively infinite in the x and y directions since periodic boundary conditions are employed in these directions in the simulations. In the z direction (the direction in which gravity acts) the system has a finite height, L_z, which is determined by the separation of the walls in the simulation box.

We analyze an arbitrary perturbation by expanding it in terms of two-dimensional waves with corresponding wave numbers, i.e. to all the quantities describing the system we ascribe a dependence on the x and y coordinates and time t of the form

$$\exp[i(k_x x + k_y y) + n(k)t],\tag{3.5}$$

where $k = (k_x^2 + k_y^2)^{1/2}$ is the wave number associated with a particular disturbance and $n(k)$ denotes the corresponding growth rate.

By substituting in the above form of solutions, and further simplifying the linear equations for the perturbations we arrive at

$$D\left[\left(\rho - \frac{\mu}{n}(D^2 - k^2)\right)Du - \frac{1}{n}D\mu(D^2 + k^2)u\right] + k^2\frac{g}{n^2}D\rho u - k^2\left[\rho - \frac{\mu}{n}(D^2 - k^2)\right]u + 2\frac{k^2}{n}D\mu Du = 0,\tag{3.6}$$

where D denotes the derivative with respect to the z coordinate, u is the z component of the velocity and g is the gravitational constant. As the system is bounded by hard walls located at $z = 0$ and $z = L_z$, it must also satisfy boundary conditions $u = 0$ and $Du = 0$ at $z = 0$ and L_z.

For known density and viscosity profiles we can, in principle, solve Eq. (3.6) to obtain the full description of the instability occurring in the system of interest.

3.3.2   Obtaining the growth rates

Equation (3.6) is a fourth order boundary value problem with variable coefficients and in the general case, i.e. the fluid of interest having arbitrary density and viscosity profiles, it is not possible to solve it analytically [52]. Solutions of this equation for some simple, special cases, such as for systems which have constant viscosity and density profiles, can be found in Ref. [36]. However, to solve Eq. (3.6) for variable density and viscosity profiles we must use numerical techniques.

We follow the method given in Ref. [53] and divide the fluid into N layers of small, but finite, thickness. The layers are taken to be perpendicular to the direction of gravity, and the density is considered as constant within each layer. In the limit of sufficiently large N this approach would allow us to solve Eq. (3.6) for an arbitrary density profile. The method in Ref. [53] does not, however, account for fluids with non-zero viscosity, but its generalization, given in Ref. [54], does – both density and viscosity are taken to be constant within the small layers that the fluid is divided into. The full details of the calculation for the case of $N = 2$ layers are given in Ref. [54].

Treating the density and viscosity as constants within a layer allows us to formulate an analytical solution together with appropriate boundary conditions within each of these small regions. Based on the density and viscosity profiles obtained from the simulations we define a certain number of layers within the simulation box and impose boundary conditions on each of them [36]. The velocity u_m in the m-th layer with constant density and viscosity can be written as

$$u_m = A_m e^{kz} + B_m e^{-kz} + C_m e^{q_m z} + D_m e^{-q_m z}, \qquad (3.7)$$

where $q_m = (k^2 + n\rho_m/\mu_m)^{1/2}$, ρ_m is the fluid density in the m-th layer, μ_m the viscosity, and A_m, B_m, C_m and D_m are unknown parameters.

The boundary conditions which must be satisfied are the continuity of $u(z)$, $Du(z)$ and $\mu(D^2 + k^2)u(z)$ across the interfaces, and the jump condition given as

$$\Delta_s\left(\left(\rho - \frac{\mu}{n}(D^2 - k^2)\right)Du\right) = -\frac{k^2}{n^2}g\Delta_s(\rho)u_s - \frac{2k^2}{n}(Du)_s\Delta_s(\mu), \qquad (3.8)$$

where $\Delta_s(f)$ denotes the jump in a function f at an interface denoted by s and f_s is the value of f at s. We differentiate between the two outermost layers that are touching the walls of the simulation box and the inner layers. Each of the surfaces of contact between two fluid layers imposes 4 boundary conditions and each of the wall boundaries imposes 2 boundary conditions, altogether giving $4N$ equations that would have to be solved to obtain the parameters A_m, B_m, C_m and D_m. To make this system of equations more notationally compact we construct a $4N$ by $4N$ matrix, which we denote by $\mathbf{M}$, and a vector $\mathbf{V}$ containing the parameters A_m, B_m, C_m and D_m (see Eq. (3.7)) such that the set of the boundary condition equations can be written as $\mathbf{MV} = 0$. By solving the dispersion relation expressed as $det\mathbf{M} = 0$ we can extract the $n(k)$ dependence.

The determinant $det\mathbf{M}$ can be calculated for a range of k values using LU decomposition which is a method for factorizing a matrix into a product of an upper triangular matrix and a lower triangular matrix. The roots of $det\mathbf{M} = 0$ correspond to the $n(k)$ values and we obtain them using Newton's root finding method. We find that the packing

fraction profiles obtained from the simulations require the use of $N \gtrsim 20$ layers giving a
matrix $\mathbf{M}$ of dimensions $\gtrsim 80 \times 80$.

3.3.3   Mass density and viscosity

Solving Eq. (3.6) for a particular system requires the gravitational constant and both
the mass density and viscosity profiles as input parameters. The density and viscosity
profiles depend on the packing fraction profile of a particular colloidal system, and we
obtain these from the simulations at a time just after the inversion of the direction of
gravity.

   We consider a simulated suspension as an incompressible simple fluid with inhomoge-
neous mass density $\rho(z)$ and kinematic viscosity $\nu(z)$, both depending only on the height
z within the simulation box. The shear viscosity is given by $\mu(z) = \rho_f \nu(z)$, where ρ_f is
the density of the fluid which is kept constant in the simulations. Based on the colloidal
packing fraction profiles we can calculate the mass density as

$$\rho(z) = \phi_A(z)\rho_A + \phi_B(z)\rho_B + (1 - \phi_A(z) - \phi_B(z))\rho_f, \qquad (3.9)$$

where $\phi_A(z)$ and $\phi_B(z)$ denote the colloidal packing fraction profiles and ρ_A and ρ_B are
the single particle mass densities of species A and B. Note that in the simulations of
different systems ρ_A and ρ_B will be different, as will the gravitational constant, which will
result in different density profiles of the colloid-rich layer.

   Calculating the viscosity of a dense colloidal layer based on the particle packing frac-
tion data turns out to be less straightforward. The suspensions we are studying consist
of two distinct regions. One is a region of pure SRD fluid for which the viscosity, μ_0, is
known [49] and the other is comprised of the two types of colloidal particles which were
packed into a disordered sediment before the direction of gravity was inverted. The overall
colloidal packing fraction profiles as obtained in our simulations are shown in Fig. 3.2. We
observe that, close to the bottom of the sediment the overall packings of all the binary
mixtures studied are in the region of the random close packing of monodisperse hard
spheres, which can be expected for distributions formed in this way [55]. With this in
mind, we do not expect the standard Einstein calculation

$$\mu(\phi) = \mu_0(1 + 2.5\phi), \qquad (3.10)$$

designed for very dilute systems, or the Saito representation which also takes hydrody-
namic interactions between particles into account [51, 56]

$$\mu(\phi) = \mu_0 \left(1 + 2.5 \left(\frac{\phi}{1 - \phi} \right) \right), \qquad (3.11)$$

to give satisfactory predictions for the viscosity profiles.

   In Ref. [51] Mendoza and Santamaria-Holek give an overview of different theoretical
and phenomenological approaches for calculating the viscosity of colloidal suspensions.
They found, however, that none of these give quantitatively good results beyond the low
volume fraction limit. By introducing a correction to Einstein's formula that takes into
account the excluded volume effects and by employing the differential effective medium
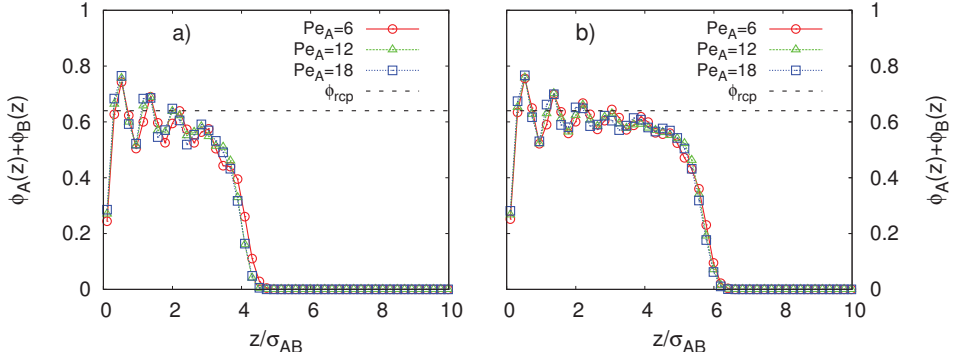
Figure 3.2: Overall packing fraction profiles for mixtures with $Pe_B = 12$, $Pe_A = 6, 12, 18$ and: a) $N_A = N_B$ and b) $N_A = 2N_B$ particles. Distances are rescaled by $\sigma_{AB} = (\sigma_{fA} + \sigma_{fB})/2$. $\phi_{rcp} \sim 0.64$ indicates random close packing of monodisperse spheres.

model, Mendoza and Santamaria-Holek arrive at a viscosity description that is valid for concentrated suspensions of mono- and poly-disperse colloidal particles [51].

Within this model the amount of space available for the particles is taken into account by defining the accessible volume as $V_{free} = V - cNV_p$, where V is the total volume of the system, V_p the volume of one particle, N the number of particles and c is a constant that takes into account the fact that not all of the total free volume can be filled with particles. The constant c is expected to assume different values for different particle shapes and sample compositions. The differential effective medium theory approach is based on adding particles to a sample in stages such that they interact with particles added in previous stages. Hence, this method requires defining an effective packing fraction which is introduced as

$$\phi_{eff} = \frac{\phi}{1 - c\phi}. \tag{3.12}$$

The expression for the viscosity Mendoza and Santamaria-Holek arrive at is

$$\mu(\phi) = \mu_0 \left(1 - \left(\frac{\phi}{1 - c\phi}\right)\right)^{-5/2}, \tag{3.13}$$

where μ_0 is the viscosity of the pure solvent, and ϕ can be taken as $\phi = \phi_A + \phi_B$ [51]. The constant c that appears in Eqs. (3.12) and (3.13) can be related to the critical packing ϕ_c by

$$c = \frac{1 - \phi_c}{\phi_c}, \tag{3.14}$$

where the critical packing ϕ_c is the only free parameter of the theory. The critical packing is defined as the packing at which the viscosity of a particular system diverges, and hence it is possible to make an estimate of its value based on the properties of the system at hand. For example, for a system of monodisperse hard spheres the critical packing would

correspond to FCC close packing or random close packing depending on whether the system of interest is forming a crystal or remaining disordered.

Using the method described above together with the simulation data we obtain the mass density and viscosity profiles of the simulated systems.

3.4 Calculating growth rates from simulation data

Using linearized equations, such as Eq. (3.6), allows us to study only the early stages of the interface deformation. To study the same regime in simulations we need to be able to identify the point in time when a system leaves the linear regime and enters the non-linear regime of the instability. This can be done by measuring the first and second density moments in time [35]. The first moment of the density is defined as the average value of the z component of particle positions, $\langle z \rangle$, and it quantifies the degree of sedimentation. The second moment of the density, $\sigma_z = \langle z^2 \rangle - \langle z \rangle^2$, quantifies the spread of the colloids in the gravity direction. Figure 3.3 shows the first and second moments as a function of time, rescaled by the height of the simulation box L_z, for the mixtures with $N_A = 2N_B$ and $N_A = N_B$ and varying Pe_A. We distinguish three different regimes in Fig. 3.3. The initial linear regime, when the undulations of the interface are still small, is identified as the regime where $\langle z \rangle$ slowly decreases and σ_z slowly increases in time. The non-linear regime, when the swirls develop fully, follows, as is indicated by the fast drop in $\langle z \rangle$ and fast increase in σ_z. Finally, both $\langle z \rangle$ and σ_z slowly decrease in time which corresponds to the final settling of the particles at the bottom wall.
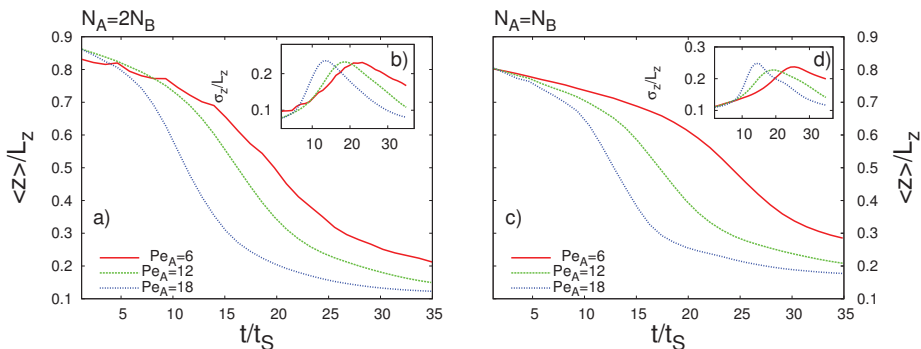

Figure 3.3: First moment of the colloidal density $\langle z \rangle / L_z$ and second moment of the colloidal density σ_z / L_z plotted as a function of time for the systems with $Pe_B = 12$, $Pe_A = 6, 12, 18$ and $N_A = 2N_B$: a) and b), and for the system with $N_A = N_B$: c) and d). The time t is measured in units of the Stokes time t_S of the larger species.

We consider only the configurations which correspond to the linear regime and follow the change of the shape of the interface separating the colloid-rich and pure solvent regions during this time. In order to identify the interface we split the simulation box into $n_{col} \times n_{col}$ square columns of width L_x/n_{col}, making sure that for the n_{col} value chosen

each column contains several particles. Next, for each column, labeled (j, k) and defined by the x and y coordinates of its center, we locate the particle with the lowest z coordinate and take this value to be the height of the interface at (x_j, y_k). We do this for all the configurations belonging to the initial regime of the instability and in this way we obtain the time dependence of the interface heights $H_{x_j, y_k}(t)$ coarse-grained at the column size level. We then perform a discrete $2D$ Fourier transform on the identified interfaces to obtain $\tilde{H}_{n_j, n_k}(t)$ which correspond to wave vectors $\mathbf{k} = (k_x, k_y)$ with $k_x = 2\pi n_j/L_x$ and $k_y = 2\pi n_k/L_y$ (with $L_x = L_y$). Finally, we plot the absolute value of the amplitude $||\tilde{H}_{n_j, n_k}||$ against time for every value of $k = (k_x^2 + k_y^2)^{1/2}$ and from an exponential fit to this we obtain the growth rates $n(k)$.

3.5 Results

We have studied binary colloidal mixtures with two different compositions: one consists of $N_A = 6500$ and $N_B = 3250$ and the other consists of $N_A = N_B = 6500$ hard-sphere-like colloidal particles. The diameters of the particles are given by σ_{AA} and σ_{BB}, where $\sigma_{AA}/\sigma_{BB} = 0.83$. In both cases the average number of fluid particles per SRD cell was set to $\gamma = 5$ yielding $N_f \sim 15 \cdot 10^6$ solvent particles for the slit size used. By setting the average number of fluid particles in a cell we also set the mass density of the fluid to $\rho_f = 5$ in simulation units. The dimensions of the slit are $L_z = 72a_0$, $L_x = L_y = 216a_0$. The motion of a colloid is characterized by its Peclet number, $Pe = \tau_D/t_S$, which is the ratio between the time τ_D a particle needs to diffuse over its own radius, and the Stokes time, t_S, it needs to sediment over the same distance. For each system that we study we set the Peclet numbers of each of the species, Pe_A and Pe_B, independently and by doing so we determine the strength of the gravitational field and the masses of the particles. We have chosen to keep Pe_B at 12 and vary Pe_A by setting it to $6, 12$ and 18. We note that for particles with fixed sizes, the relative Peclet number Pe_A/Pe_B is proportional to the ratio of the effective densities of the two particle species $(\rho_A - \rho_f)/(\rho_B - \rho_f)$.

We calculate the growth rates using both the theoretical approach outlined in Sec. 3.3 and directly from simulation data as described in Sec. 3.4. The results of these calculations are presented in Fig. 3.4. We note that when plotting the theoretical curves it is also necessary to include a correction which takes into account the effects of particle diffusion. The corrected $n(k)$ becomes $n(k) - (D_A + D_B)k^2$, where D_A and D_B are the diffusion constants of particles A and B respectively [35].

We first note that for all systems studied we find excellent qualitative and quantitative agreement between the theoretical predictions and the simulation results. We observe that the growth rates for both mixtures ($N_A = 2N_B$ and $N_A = N_B$) reach their maxima at finite values of the wave number k. The wave lengths corresponding to the wave numbers for which the maxima are reached are the initially fastest growing wave lengths. In Fig. 3.4 it can also be seen that the growth rates are larger for systems with larger Peclet numbers of species A. This indicates that the interface undulations, which develop as a consequence of the instability, develop faster for systems with higher Pe_A. The interface between the colloid-rich and the pure solvent regions in these systems deforms faster and allows the fluid to penetrate the colloidal layer sooner, leading to the quicker formation of the swirls
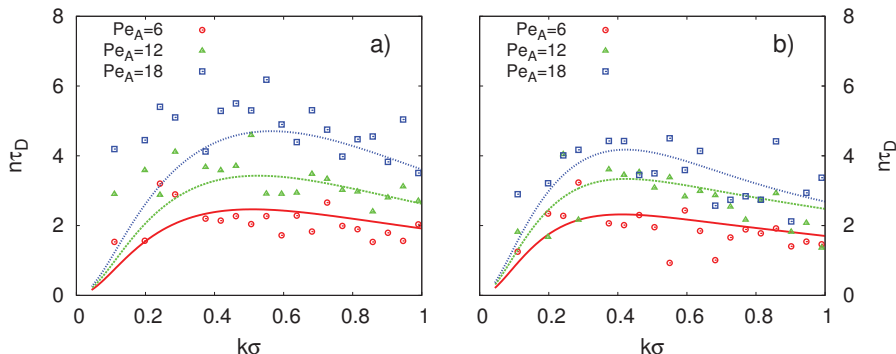
Figure 3.4: Growth rates $n\tau_D$ plotted against wave numbers $k\sigma$ of the instability as obtained from simulations (symbols) and theory (lines). τ_D is the diffusion time of larger colloids (species B) and the length σ is taken as the average particle diameter, $\sigma = (\sigma_{AA} + \sigma_{BB})/2$. In all cases $Pe_B = 12$ and we plot results for systems with $Pe_A = 6, 12$ and 18, for: a) $N_A = 2N_B$ and b) $N_A = N_B$.

that facilitate the fast sedimentation of the colloidal material (see also Fig. 3.3), until the system reaches a stable configuration.

Finally, we comment on the viscosity model used. As described in Sec. 3.3.3 to obtain the viscosity profiles from the packing fraction profiles it is necessary to define the critical packing ϕ_c. This is the packing fraction at which the viscosity of a mixture diverges. The initial configurations we study contain a dense discorded sediment, and as such we would expect the ϕ_c values to be close to the random close packing of the mixture. For monodisperse spheres this is ~ 0.64 and since the particle diameter ratio of the binary mixtures we study is close to 1 we use $\phi_c = 0.64$ as an initial guess and then vary it to find the best agreement with the simulation results. The values we used to calculate the growth rates shown in Fig. 3.4 are given in Table 3.1.

ϕ_c	$N_A = 2N_B$	$N_A = N_B$
$Pe_A = 6$	0.615	0.59
$Pe_A = 12$	0.63	0.605
$Pe_A = 18$	0.66	0.63

Table 3.1: Values of critical packing ϕ_c used to obtain the viscosity profiles for the calculations of the growth rates plotted in Fig. 3.4 for mixtures with $N_A = 2N_B$ and $N_A = N_B$ and $Pe_A = 6, 12$ and 18. $Pe_B = 12$ in all cases.

For systems consisting of a single colloidal species immersed in an SRD bath studied in Ref. [35] it was found that using the Saito approximation [56] to estimate the viscosity yielded satisfactory results for the instability growth rates. In Fig. 3.5 we plot the growth rates as calculated from our simulations compared to predictions obtained using the Saito representation of the viscosity together with the diffusion corrections. As can be seen, the

Saito approximation based viscosity profiles result in overestimated growth rates. This suggests that the higher packing and added complexity of a binary mixture, as compared to a monodisperse system, result in an instability description that is more sensitive to the viscosity model used.
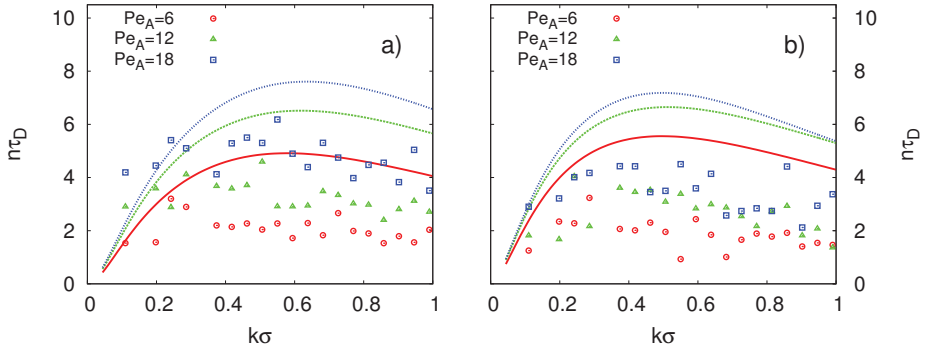

Figure 3.5: Growth rates $n\tau_D$ plotted as a function of wave numbers $k\sigma$ of the instability as obtained from simulations (symbols) and theory using the viscosity profiles based on the Saito approximation (lines). τ_D is the diffusion time of larger colloids (species B) and the length σ is taken as the average particle diameter, $\sigma = (\sigma_{AA} + \sigma_{BB})/2$. In all cases $Pe_B = 12$ and we plot results for systems with $Pe_A = 6, 12$ and 18, for: a) $N_A = 2N_B$ and b) $N_A = N_B$.

3.6   Conclusions

Systems consisting of a heavy fluid layer placed above a lighter one are not stable with respect to gravity and hence their evolution results in the formation of a Rayleigh-Taylor-like instability. We have studied this behavior in the context of confined binary colloidal mixtures with different compositions immersed in a solvent, using a computer simulation technique that incorporates both hydrodynamic interactions and Brownian motion. The initial top-heavy configurations were generated by allowing a homogeneously dispersed colloidal mixture to sediment onto a wall of the simulation box, followed by reversing the direction of gravity. This results in initial configurations with a dense layer of what is effectively a sediment placed on top of a less dense layer of a pure solvent.

In this chapter we have studied the initial regime of the instability by calculating the growth rates of the unstable modes. We have calculated the growth rates both directly from our simulation data and theoretically via a linear stability analysis, finding good qualitative and quantitative agreement. Calculations based on the simulation data require a definition of the interface between the colloid-rich phase and the pure solvent which deforms as the system undergoes the Rayleigh-Taylor-like instability. The theoretical approach relies on obtaining well defined initial mass density and viscosity profiles. We have outlined the general hydrodynamic treatment of fluids with varying density and viscosity, and described the numerical method we have used to solve the hydrodynamic equations.

Our results show the existence of a wave length of fastest growth for each system studied. Increasing the Peclet number of the smaller particles leads to the overall increase in the magnitude of the growth rates, i.e. the interface between the colloid-rich and pure solvent regions deforms faster. We also find that the wave numbers corresponding to the fastest growing wave lengths increase with the Peclet number.

Comparing the theoretical predictions of the growth rates to those obtained from the simulation data shows that an accurate description of the viscosity is essential for predicting the behavior of the initial regime of the instability. The complexity and high packing of binary mixtures lead to these systems being more viscous than the corresponding monodisperse systems, and hence standard viscosity models can lead to inaccurate predictions.

Finally, we note that the only microscopic information required to obtain an accurate theoretical description of the instability growth rates are the initial packing fraction profiles. This indicates that the initial behavior of the instability depends only on the macroscopic properties of the complex fluid and not on the specific properties of the colloidal particles in the solvent. Hence, we believe that this analysis could be applicable to any other colloidal system, irrespective of the particle shape or the level of polydispersity.

3.7   Acknowledgments

4

Phase diagram of hard snowman-shaped particles

In this chapter we present the phase diagram of hard snowman-shaped particles which was obtained using Monte Carlo simulations and free energy calculations. The snowman particles consist of two hard spheres rigidly attached at their surfaces. We find a rich phase behavior with isotropic, plastic crystal and aperiodic crystalline phases. The crystalline phases found to be stable for a given sphere diameter ratio correspond mostly to the close packed structures predicted for equimolar binary hard-sphere mixtures of the same diameter ratio. However, our results also show several crystal-crystal phase transitions, with structures with a higher degree of degeneracy found to be stable at lower densities, while those with the best packing are found to be stable at higher densities.

4.1   Introduction

The potential for building colloidal structures with useful optical, mechanical and/or functional properties has lead to the development of new routes for synthesizing anisotropic colloids [57]. Recent work has shown the prospect of controlling the size, shape and surface properties of colloidal particles [58, 59], resulting in a huge number of possible building blocks. Understanding how the microscopic properties of these particles affect the macroscopic behavior of a system is therefore very important.

One such colloidal particle with a simple anisotropic shape is the snowman particle, which consists of two spheres of different diameters joined together. Particles with this specific geometry can also be referred to as hetero-atomic dimers or asymmetric dumbbells. It is possible to synthesize snowman-shaped particles with a range of different diameter ratios of the two spheres and also with different sphere separations [60, 61, 62, 63, 64, 65], providing a large phase space even for purely repulsive interactions. These particles have the potential to mimic diatomic molecules and form a wide range of crystalline structures, and it would clearly be desirable to understand their phase behavior. However, understanding the packing of colloidal particles with purely hard-body interactions has been a persistent challenge. Even for hard spheres, which are the simplest 3-dimensional reference system and which have been studied since the early days of computer simulations [66, 67], the issue of the relative stability of the face-centered-cubic (FCC) and hexagonal-close-packed (HCP) crystalline structures was a longstanding one [68, 69, 70]. Particle anisotropy only adds to this complexity.

Perhaps the simplest model anisotropic particle is the hard dumbbell (or dimer), which can be seen as a special case of a snowman particle formed from hard spheres of equal diameter. Such systems have been extensively studied in both two and three dimensions using theoretical [71, 72, 73] and simulation [74, 75, 76, 77, 78] approaches. The phase diagram of these particles is already surprisingly rich [78], with a variety of crystalline structures found to be stable. In the case when the spheres are tangential, this system forms a stable crystalline phase where the constituent spheres sit on an FCC lattice and are randomly connected to form dimers. This so-called aperiodic FCC structure [75, 76, 77, 78] offers an interesting parallel to the FCC structure of hard spheres. The similar nature of the crystalline phases of tangential dumbbell and hard-sphere systems suggests the intriguing prospect that other tangential dimer systems, such as snowman-shaped particles, can form binary hard-sphere crystalline phases, where the two spheres of the dimer would sit on the corresponding lattice sites of the binary crystal. Therefore, as well as being interesting anisotropic particles in their own right, snowman particles can also be viewed as a system of paired up spheres.

Binary hard-sphere mixtures are often used as a colloidal model for atomic systems [27, 79, 80]. Several attempts have been made to determine the closest packed crystalline structures of binary hard sphere mixtures using theoretical [81] and simulation methods [82, 83, 84, 85]. In particular, Ref. [84] found $NaCl$, CrB, αIrV and $\gamma CuTi$ structures to be close packed for various diameter ratios, and being able to form this rich variety of colloidal crystals would be desirable. However, studies of the phase behavior show that these crystal structures are often metastable with respect to other crystal structures or phase separated FCC structures [23]. Fabrication of the best packed structures could

be aided by using snowman-shaped particles, as phase separation would no longer be an issue since each large sphere is already tangential to a smaller sphere. Stucke and Crespi [86] attempted to predict the best packed structures for snowman-shaped particles and found some of those later predicted for binary hard spheres [84]. While knowledge of the best packed structures can give an indication of the phase behavior of a system at highest densities, it does not give any information on the phase behavior at lower densities nor about the phase boundaries.

A recent study of snowman-shaped particles with various soft potentials, which used molecular dynamics simulations [87], showed that an $NaCl$ crystal forms spontaneously under compression for diameter ratios below ~ 0.41 as the potential approaches the hard-particle limit. Similarly, for large diameter ratios ($\gtrsim 0.95$) FCC-like structures were found to form [72, 73]. For intermediate diameter ratios, however, no crystalline structures formed spontaneously, possibly due to the potential crystal structures in this region being kinetically inaccessible [87]. In this chapter, we use computer simulations to map out the phase diagram of hard snowman-shaped particle systems by evaluating the free energies of candidate crystalline structures which correspond to the close packed structures of binary hard-sphere mixtures. We take the structures found in Ref. [84] to be our candidate crystals, and we place the large and small spheres making up the snowman particles on the lattice sites. As the spheres are tangential there is no difference in the close packed structures of the snowmen and the binary crystals [82]. Therefore, we define all crystalline structures based on the positions of the constituent spheres of the snowmen.

4.2 Method

4.2.1 Simulation Details

We perform Monte Carlo (MC) simulations on systems of hard snowman-shaped particles. These particles consist of two hard spheres rigidly bonded at their surfaces (see Fig. 4.1). We define the shape of these particles by the ratio of the constituent sphere diameters $d = D_S/D_L$, where D_S is the diameter of the smaller sphere and D_L is the diameter of the larger sphere. In the limiting case of $d = 0$ the snowmen reduce to hard spheres and for $d = 1$ they reduce to hard-sphere dimers. We study systems defined by d ranging from $d = 0$ to $d = 1$ in steps of 0.1, except in the regions of $0.2 < d < 0.5$ and $0.9 < d < 1$ where a higher resolution is required to clarify the phase behavior.
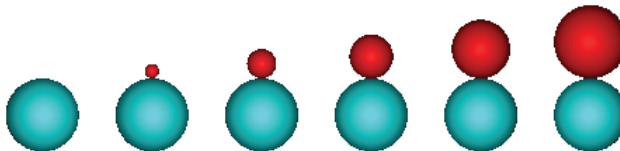

Figure 4.1: Snowman-shaped particles with sphere diameter ratios $d = D_S/D_L = 0$ to $d = 1$, shown in intervals of 0.2.

To obtain the equations of state (EOS) for a given diameter ratio d, we perform constant pressure Monte Carlo (NPT) simulations on a system of $N \sim 500$ snowman-shaped particles, at temperature T and pressure P. We note that only the ratio P/T is relevant in hard-body systems. For all systems studied we perform both compression runs, where we start from an initial isotropic fluid configuration at low pressure and then increase P in small steps, and expansion runs, where we employ one of the candidate crystal structures and decrease the pressure until the crystal melts. As the candidate crystal structures we consider those which were predicted in Ref. [84] to be densely packed for the binary hard-sphere systems with the corresponding d values. We list these in Table 4.1. For each state point (i.e. at each pressure P) we divide the simulation runs into two parts: an equilibration part of $\sim 2 \times 10^6$ MC cycles, followed by a production part of $\sim 4 \times 10^6$ MC cycles from which we obtain the density ρ of the system at pressure P, and hence the EOS.

$d = D_S/D_L$	Candidate structures			
0.1	$NaCl$	CrB		
0.2	$NaCl$	CrB		
0.25	$NaCl$	CrB		
0.3	$NaCl$	CrB		
0.35	$NaCl$	CrB		
0.38	$NaCl$	CrB		
0.4	$NaCl$	CrB		
0.42	$NaCl$	CrB		
0.48	CrB	$NaCl$		
0.5	CrB	$\gamma CuTi$	$NaCl$	αIrV
0.6	CrB	$\gamma CuTi$	αIrV	$NaCl$
0.7	CrB	αIrV	$CsCl$	$\gamma CuTi$
0.8	$\gamma CuTi$	αIrV	$CsCl$	CrB
0.9	αIrV	$\gamma CuTi$	$CsCl$	CrB
0.95	αIrV	FCC^*		
0.97	αIrV	FCC^*		
0.98	αIrV	FCC^*		

Table 4.1: Candidate crystal structures for snowman-shaped particles of diameter ratio $d = D_S/D_L$ ranging from 0.1 to 0.98, listed from best packed at high pressure to less well packed as found in Ref. [84].

4.2.2   Crystal structures

For a large range of d values compression of isotropic phases does not result in the spontaneous formation of crystalline structures. Therefore, in order to obtain the crystalline branches of the EOS we must generate all candidate crystals at high pressure and then expand them until they melt. As the snowmen consist of tangential spheres, we choose

to classify their crystalline structures as the structures of the corresponding binary hard-sphere crystals, i.e. we classify them as the crystal lattices that the constituent spheres, instead of the particle centers of mass, are positioned on. However, in addition to the positions of the constituent spheres, a snowmen crystal structure is also defined by the orientational ordering of the particles, and this gives rise to three types of orientational organization. These are: (i) periodic crystals (PC), in which the constituent spheres have positional order and the snowmen have periodic orientational ordering; (ii) aperiodic crystals (APC), in which the constituent spheres have positional order but there is no repeating orientational ordering of the snowmen, and as such the snowmen centers of mass are positionally aperiodic; (iii) rotator (plastic) crystals (RC), in which the snowmen center of mass positions are on average located on a lattice, but the particles can still rotate (although free rotation can be hindered by the surrounding particles). We note that, particularly at high densities, the instantaneous position of a particle in a rotator phase can be correlated to its orientation [88]. For large d values we also find one additional type of structure in which the constituent spheres lie on a slightly distorted FCC lattice with the large and small spheres positioned on random sites. As such, this structure has no repeating positional ordering of the constituent spheres, nor repeating orientational or positional ordering of the snowman particles. These structures are similar to the 2D aperiodic structures studied in Ref. [89], and also to the aperiodic FCC-like structure found to be stable for $d = 1$ (tangential dumbbells) in Ref. [78], and we will refer to them as FCC^* from here on.

For both PCs and RCs, there is only one possible configuration, and to obtain the EOS for a given d, only a single set of expansion runs has to be performed. There is, however, a large number of configurations (yet finite for a given number of particles) that we characterize as APCs of a given crystal structure, as there are multiple combinations of snowman orientations with the same corresponding binary crystal structure. The number of possible configurations defines the degeneracy of an APC. For snowman-shaped particles the APC and PC of each crystalline structure are indistinguishable in terms of packing due to the non-penetrating nature of the two constituent spheres. As such, we would expect the PC and different APC configurations of a candidate crystal to have identical EOS, and hence that the periodic crystal structures can be considered as a special case of the APC configurations. We check this by generating and expanding a PC and 3 APC configurations for each candidate crystal. For FCC^* structures, there are again multiple configurations and in this case, due to the random positioning of the large and small constituent spheres on the lattice sites, we would expect different configurations to have slightly different EOS, particularly at high densities where packing considerations become important. Because of this, we also generate and expand multiple FCC^* configurations for the relevant d values.

We generate the candidate crystal structures using the following method. Firstly, we generate a binary hard-sphere structure of $N_L = N_S \sim 64$ particles for each of the candidate structures. We then allow these to equilibrate at high pressure, and based on the configuration obtained we produce a larger system of typically $N_L = N_S \sim 500$ spheres. The exact number varies slightly depending on the crystal structure. Next we connect neighboring spheres of different species to form a periodic crystal structure of snowman-shaped particles. Finally, we use bond-switch moves [78] to produce APC

crystals. For FCC^* structures we use the same method, but we start from a crystal with $D_L = D_S$ from which we form an APC crystal. We then reduce the diameter of one of the constituent spheres (chosen randomly) to give the required d value. This system is finally allowed to equilibrate at high pressure.

Rotator phases form spontaneously during the expansion runs, and in the case of low d during the compression runs as well. As such, we do not need to generate these configurations.

4.2.3   Free energy calculations

We determine which crystals are stable and map out the phase diagram, using free energy calculations. In order to calculate the Helmholtz free energy F of the isotropic phases we initially use the Widom particle insertion method [90] to calculate the chemical potential μ, which is then related to the free energy by

$$\frac{F}{N} = \mu - \frac{P}{\rho}. \tag{4.1}$$

To calculate the free energies of the candidate crystal structures we use the thermodynamic integration method to integrate from a reference state. For each crystal of interest the reference state is a non-interacting Einstein crystal with the corresponding structure, for which the free energy can be calculated analytically [8]. The method we use is similar to that in Ref. [78], which considered hard dumbbells, with some adaptations required to describe snowman-shaped particles.

We begin by considering rotator crystals in which the snowmen particles do not have fixed orientations but their average centers of mass are positionally ordered. We wish to be able to follow a path through phase space that connects an RC to the reference Einstein crystal. To do so, we start by tethering the snowmen with harmonic springs to their corresponding lattice sites in the reference crystal. The coupling potential energy function is given by

$$\beta U_k(\mathbf{r}^N, \mathbf{u}^N, k) = k \sum_{i=1}^{N} \frac{(\mathbf{r}_i - \mathbf{r}_{i,0})^2}{\sigma^2}, \tag{4.2}$$

where k is the spring constant, $\mathbf{r}_i - \mathbf{r}_{i,0}$ is the distance of particle i at position $\mathbf{r}_i$ from its corresponding lattice site at $\mathbf{r}_{i,0}$ and $\mathbf{u}_i$ is the orientation of the snowman particle. We take $\sigma = D_L$ to be the unit of length in our systems. To obtain the lattice site positions $\mathbf{r}_{i,0}$ of the reference crystal we calculate the average center of mass position of each particle in an equilibrated crystal configuration using constant volume (NVT) simulations at a state point of interest. For $k = 0$ the particles are completely untethered, and such a system corresponds to the structure under consideration (i.e. the rotator crystal). The spring constant k is then increased gradually to a value $k_{\max}$, at which the particles are completely fixed to their lattice sites. We find that a value $k_{\max} \sim 16000$ is sufficient to fix the particles.

While the particles are now fixed positionally, they can still rotate about their center of mass and hence particle interactions are still possible. To ensure that the particles do not interact as they rotate, we replace the hard-core interaction of the snowmen with a

pair potential that allows the softness of the interaction to be tuned. We use the following soft potential

$$\beta U_\gamma(\mathbf{r}^N, \mathbf{u}^N, \gamma) = \begin{cases} \gamma \sum_{i<j}^N \sum_{a,b=1}^2 \left(1 - A\frac{(\mathbf{r}_{ia} - \mathbf{r}_{jb})^2}{\sigma^2}\right) & |\mathbf{r}_{ia} - \mathbf{r}_{jb}| \le \sigma_{ab}, \\ 0 & |\mathbf{r}_{ia} - \mathbf{r}_{jb}| > \sigma_{ab}, \end{cases} \quad (4.3)$$

where $\mathbf{r}_{ia} - \mathbf{r}_{jb}$ is the separation of sphere $a = 1, 2$ of particle i from sphere $b = 1, 2$ of particle j, σ_{ab} is the interaction diameter ($\sigma_{11} = D_1$, $\sigma_{22} = D_2$ and $\sigma_{12} = \sigma_{21} = (D_1 + D_2)/2$), and γ and A are adjustable parameters. We set $A = 0.9$ throughout [78], and vary γ from 0 to $\gamma_{\max}$. In the limit of $\gamma \to \infty$, the potential reduces the system to hard snowmen once more, and we find that a value of $\gamma \gtrsim 150$ is sufficient to achieve this behavior. As such, we begin from a maximum value of $\gamma_{\max} = 200$, and then slowly reduce γ until $\gamma \to 0$, where the constituent spheres become non-interacting.

We now have the following integration path from the rotator phase to the reference crystal: at $\gamma_{\max}$, where the particles behave as hard snowmen, we turn on the spring potential $U_k(\mathbf{r}^N, \mathbf{u}^N, k)$ by increasing k from 0 to $k_{\max}$ to fix the particles to their lattice sites. At $k_{\max}$ we decrease γ to 0 so that the particles cease to interact, and the system reduces to a non-interacting Einstein crystal. The Helmholtz free energy F of a system of N particles at volume V and temperature T is then calculated by integrating over this path, and is given by

$$\beta F = \beta F_E - \int_0^{k_{\max}} dk \left\langle \frac{\partial \beta U_k}{\partial k} \right\rangle_{\gamma_{max}} + \int_0^{\gamma_{\max}} d\gamma \left\langle \frac{\partial \beta U_\gamma}{\partial \gamma} \right\rangle_{k_{max}}$$

$$= \beta F_E - \int_0^{k_{\max}} dk \left\langle \sum_{i=1}^N \frac{(\mathbf{r}_i - \mathbf{r}_{i,0})^2}{\sigma^2} \right\rangle$$

$$+ \int_0^{\gamma_{\max}} d\gamma \left\langle \sum_{i<j}^N \sum_{a,b=1}^2 \left(1 - A\frac{(\mathbf{r}_{ia} - \mathbf{r}_{jb})^2}{\sigma^2}\right) \right\rangle, \quad (4.4)$$

where F_E is the Helmholtz free energy of a non-interacting Einstein crystal together with the center of mass correction, and $\langle \dots \rangle$ denotes the ensemble average. In our case F_E is given by

$$\beta F_E = \frac{3(N-1)}{2} \ln\left(\frac{\pi}{k_{\max}}\right) + \ln\left(\frac{\rho\sigma^3}{N^{3/2}}\right) + N \ln(\Lambda_r^2) + N \ln\left(\frac{\Lambda_t^3}{\sigma^3}\right). \quad (4.5)$$

Λ_r is given by

$$\Lambda_r = \sqrt{\frac{\beta h^2}{8\pi^2 I}}, \quad (4.6)$$

where h is the Planck constant and I is the moment of inertia of a particle. Λ_t is the de Broglie wavelength given by

$$\Lambda_t = \sqrt{\frac{\beta h^2}{2\pi m}}, \tag{4.7}$$

where m is the particle mass. We calculate the integrands in Eq. (4.4) by performing NVT Monte Carlo simulations and using these together with Eq. (4.5) we calculate the free energies of all the rotator phases.

We now consider PC, APC and FCC^* structures as defined in Sec. 4.2.2. In order to obtain the free energies we follow the same procedure as outlined above for RCs. However, we also add an additional term to the potential in Eq. (4.2), which couples the particle orientations to the corresponding orientations in the reference crystal. We use NVT simulations to calculate the average positions $\mathbf{r}_{i,0}$ and orientations $\mathbf{u}_{i,0}$ of each particle within the crystal. Equation (4.2) then becomes

$$\beta U_k(\mathbf{r}^N, \mathbf{u}^N, k) = k \sum_{i=1}^{N} \left(\frac{(\mathbf{r}_i - \mathbf{r}_{i,0})^2}{\sigma^2} + \frac{1 - \cos\theta_i}{2} \right), \tag{4.8}$$

where θ_i is the angle between the orientations of particle i and the corresponding particle in the reference crystal, and is given by $\cos^{-1}(\mathbf{u}_i \cdot \mathbf{u}_{i,0})$. Eq. (4.4) is therefore modified to become

$$\beta F = \beta F_E \quad - \quad \int_0^{k_{\max}} dk \left\langle \frac{\partial \beta U_k}{\partial k} \right\rangle_{\gamma_{max}} + \int_0^{\gamma_{\max}} d\gamma \left\langle \frac{\partial \beta U_\gamma}{\partial \gamma} \right\rangle_{k_{max}} - \ln\Omega$$

$$= \beta F_E \quad - \quad \int_0^{k_{\max}} dk \left\langle \sum_{i=1}^{N} \left(\frac{(\mathbf{r}_i - \mathbf{r}_{i,0})^2}{\sigma^2} + \frac{1 - \cos\theta_i}{2} \right) \right\rangle$$

$$+ \quad \int_0^{\gamma_{\max}} d\gamma \left\langle \sum_{i<j}^{N} \sum_{a,b=1}^{2} \left(1 - A \frac{(\mathbf{r}_{ia} - \mathbf{r}_{jb})^2}{\sigma^2} \right) \right\rangle$$

$$- \quad \ln\Omega, \tag{4.9}$$

where we again integrate over both the spring and soft potentials to relate the free energy of each crystal structure to that of the corresponding reference crystal. Note that there is now an additional term $\ln\Omega$, where Ω denotes the degeneracy of the crystalline phase (i.e. the number of possible configurations of a structure). We calculate the value of Ω using the series expansion method given in Ref. [91], which has been shown to be accurate for sufficiently large systems [78]. The zeroth order term Ω_0 of this expansion, which reduces to the Bethe approximation, depends solely on the number of smaller spheres that touch each larger sphere, which we denote as q, and is given by

$$\Omega_0 = q^N \left(1 - \frac{1}{q} \right)^{N(q-1)}. \tag{4.10}$$

The higher order terms vary even for structures with the same q value, and we calculate these up to 8th order and show the calculated values of $\ln \Omega$ in Table 4.2. A more detailed description of the method used is given in the Appendix of this chapter. Typically we find that the difference between the values obtained from the high order expansion and from the zeroth order term is of the order of a few percent. For FCC^* crystalline phases, Ω is calculated as for the aperiodic FCC phases of dumbbells with equal sized spheres, with the positional degeneracy arising from the up-down asymmetry of snowman-shaped particles with $d < 1$ taken into account. Finally, the free energy of the non-interacting Einstein crystal F_E with the center of mass correction becomes

$$\beta F_E = \frac{3(N-1)}{2} \ln \left(\frac{\pi}{k_{\text{max}}} \right) + \ln \left(\frac{\rho \sigma^3}{N^{3/2}} \right) + N \ln(\Lambda_r^2) + N \ln \left(\frac{\Lambda_t^3}{\sigma^3} \right) - N \ln(J(k_{max})), \quad (4.11)$$

where the final term arises due to the orientational part of the potential given in Eq. (4.8), and is given by

$$J(k) = \int_{-1}^{1} e^{k(x-1)/2} dx = \frac{2(1 - e^{-k})}{k}. \quad (4.12)$$

In order to account for finite size effects, for all crystalline phases we perform free energy calculations for various N values, and extrapolate the results to $N \to \infty$.

Using the free energies and the equation of state calculations, we determine the coexistence regions by equating both the pressure and chemical potential in phase i at density ρ_i and in phase j at density ρ_j

$$\begin{aligned} P(\rho_i) &= P(\rho_j) \\ \mu(\rho_i) &= \mu(\rho_j). \end{aligned} \quad (4.13)$$

Finally, we use these to construct the phase diagram.

Crystal structure	q	$\ln \Omega/N$
$NaCl$	6	0.8945
CrB	6	0.8933
CrB	7	1.0279
αIrV	6	0.8864
αIrV	8	1.1504
$\gamma CuTi$	4	0.5423
$\gamma CuTi$	5	0.7293
FCC^*	12	2.2114

Table 4.2: Degeneracy term per particle $\ln \Omega/N$ of the candidate crystal structures for snowmen particles. q gives the number of smaller spheres that touch each large sphere.
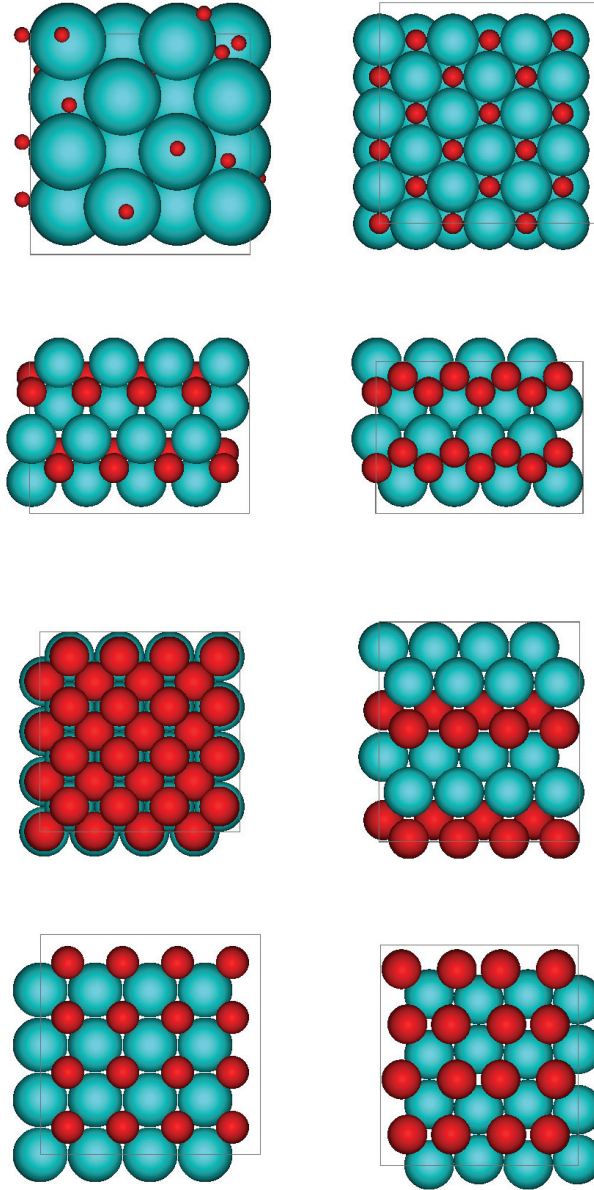
Figure 4.2: Examples of candidate crystal structures for snowmen particles (see text). Light blue spheres are larger spheres with diameter D_L, red spheres are smaller spheres with diameter D_S. Top row, left: rotator crystal (RC) with diameter ratio $d = D_S/D_L = 0.2$. Top row, right: $NaCl$ with $d = 0.4$. Second row: two planes of CrB with $d = 0.5$. Third row: two planes of $\gamma CuTi$ with $d = 0.8$. Bottom row, left: $CsCl$ with $d = 0.6$. Bottom row, right: αIrV with $d = 0.8$.

4.3 Results

4.3.1 Crystal structures

We first comment on the candidate crystal structures we constructed using the method described in Sec. 4.2.2. As starting configurations we employ the dense packed crystal structures as predicted for the equimolar binary hard-sphere mixtures in Ref. [84]. We refer the interested reader to the supplementary information of Ref. [82] for data necessary to construct the close packed structures. After generating the crystals we perform NPT Monte Carlo simulations on these systems at very high pressures. Figure 4.2 shows example snapshots of each of the candidate crystalline structures considered. We note that, with the exception of the $CsCl$ structure, all of the candidates considered are the best packed structure for some range of d values. We also find that for some d values the generated candidate structures can reconfigure into other structures (such as $CsCl$ structures forming αIrV structures, $\gamma CuTi$ structures forming CrB structures, etc.), which allows us to discard some of the potential candidate structures in advance of performing the free energy calculations. We do note, however, that we observe no transitions between the various APC configurations of a candidate structure, or between the various FCC^* structures during our simulation runs.
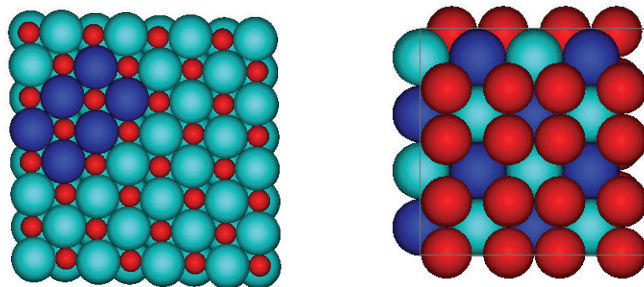

Figure 4.3: Examples of modified candidate crystal structures of snowmen particles (see text). Blue spheres are larger spheres with diameter D_L, red spheres are smaller spheres with diameter D_S. Left: $NaCl$ of snowmen particles with diameter ratio $d = 0.45$. The dark blue region highlights the modified behavior where we see that pairs of larger spheres alternate between touching and being separated. Right: αIrV with $d = 0.85$, where dark blue spheres are larger spheres with 4 neighbors and light blue spheres are larger spheres with 8 neighbors.

In most cases the highest packings that we find agree with those given in Refs. [82, 84]. However, upon further compression in several cases we find that systems with certain structures can maximize their packing by regularly distorting the initial lattice configurations. For $d > 0.414$, we find that a system with the standard $NaCl$ structure can

significantly increase its packing by separating alternating pairs of large spheres that touch at close packing, to fit better the smaller spheres in between (see Fig. 4.3). Similarly, for $0.75 \lesssim d \lesssim 0.95$, the αIrV structure changes from having the same number of small spheres touching each large sphere at intermediate pressures, to alternating numbers of contacts at high pressures (i.e. half of the large spheres have 4 small sphere neighbors and half have 8, see Fig. 4.3). When we expand these modified structures we find that they change continuously into the initial, simpler, crystalline structures, at a density at which the particles have sufficient free space that the distortion is no longer necessary.

In Fig. 4.4 we show the densities of best packing for all the candidate crystals considered. As noted previously, in some cases the candidate structures may have either formed modified structures or changed into other structures. However, we find that the crystal structures only change into other crystal structures for d values where the candidate crystal under consideration is anyway not the best packed structure. We finally note that the number of contacts that each sphere has with spheres of different diameter at highest packing determines the number of ways we can connect the spheres into snowmen particles, and hence also the degeneracy of the APC structures.
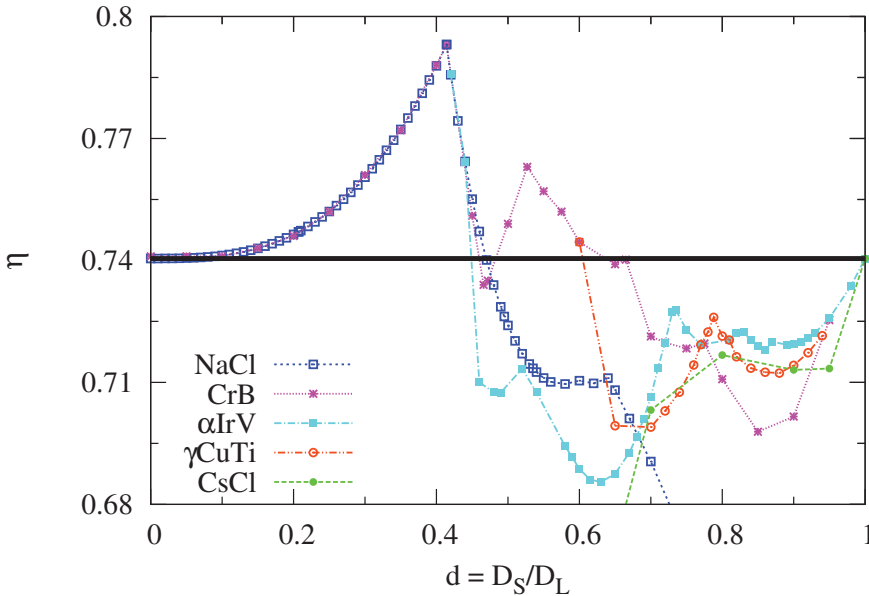

Figure 4.4: Close packing densities (given as packing fraction $\eta = N v_0 / V$ with v_0 the particle volume) of candidate crystal structures for snowman-shaped particles as a function of diameter ratio d, constructed using the method outlined in Sec. 4.2.2. Solid line at $\eta = 0.74048$ represents the close packing density of hard spheres. The legend indicates the crystal structures that the compression runs start from, although in some cases the initial structures have rearranged to form another structure.

4.3.2   Equations of state

We now examine the equations of state (EOS) calculated from our simulation runs, beginning with the compressions of the isotropic fluid phases. For systems with $d \lesssim 0.3$ we see the spontaneous formation of rotator phases upon compression (see Fig. 4.5a for the EOS for $d = 0.1$), with the centers of mass of the particles located on average on an FCC lattice. In the case of $d \lesssim 0.2$, further compression of the obtained RCs does not result in any further phase transitions. However, at higher densities we observe that the large spheres, rather than the particle centers of mass, are positioned on an FCC lattice, while the smaller spheres can still move within the free space. We note that in this case the gaps left by the larger spheres are large enough to fit multiple smaller spheres. For $0.2 \lesssim d \lesssim 0.3$, where the gaps are no longer large enough, compression of the RCs results in the formation of an aperiodic structure resembling the $NaCl$ crystal.
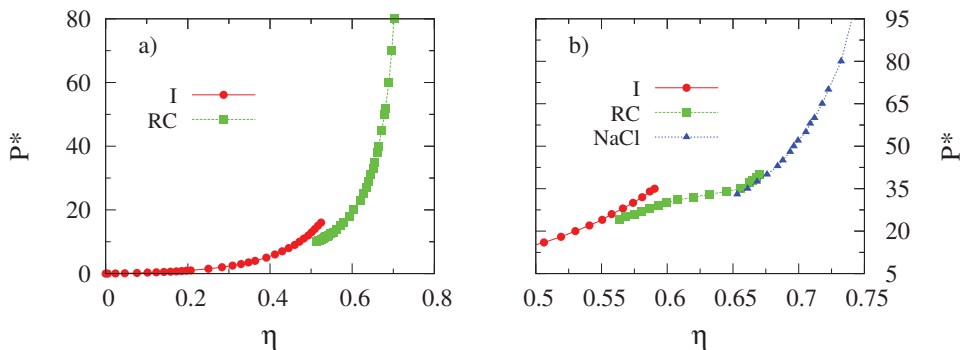

Figure 4.5: Equations of state of: a) isotropic and rotator phases for $d = 0.1$ and b) isotropic, rotator and $NaCl$ phases for $d = 0.4$. $\eta = Nv_0/V$ is the packing fraction with v_0 the particle volume, and $P^* = \beta P D_L^3$ is the reduced pressure. I denotes the isotropic fluid phase and RC denotes the rotator crystal phase.

For $d \gtrsim 0.3$ compression of the isotropic fluid phase does not result in any phase transitions and therefore we must expand one of the generated candidate crystal structures. For each candidate crystal structure we have examined at least 3 different aperiodic structures as well as the periodic structure. We find that each of these have the same EOS, and as an example we show this for the CrB crystal with $d = 0.7$ in Fig. 4.6a. As mentioned previously, this is to be expected since the constituent spheres of the snowmen particles are joined at their surfaces and hence arranging the snowmen orientations periodically would not result in better overall packing. As before, we conclude that the PCs for snowmen particles can be considered as a special case of the corresponding APC crystalline structures.

For systems up to $d \sim 0.48$ we find that upon expansion the candidate crystals transition into RC phases, where once again the particle centers of mass are on average positioned on an FCC lattice. Once formed, we recompress the RCs, and we find that for

$0.2 \lesssim d \lesssim 0.48$ this does not result in the reformation of the candidate crystal structure, but instead results in the continuous change to a structure with fixed particle orientations, resembling the $NaCl$ crystal. As an illustration of this behavior we show in Fig. 4.5b the EOS for $d = 0.4$. Further expansion of all RCs results in a transition to an isotropic fluid phase.
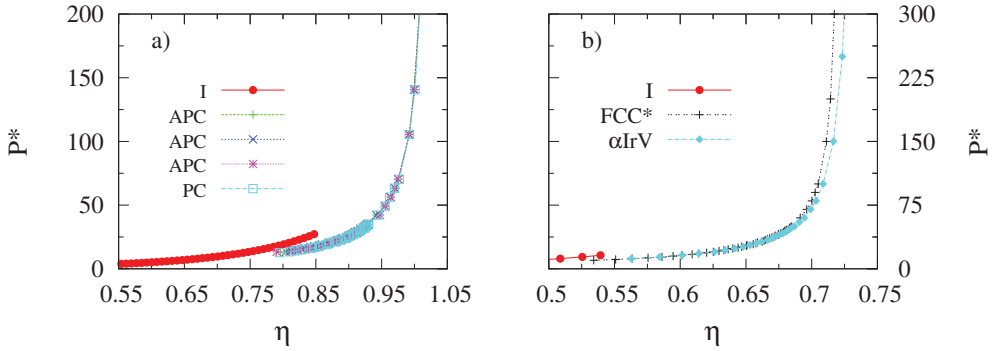

Figure 4.6: Equations of state of: a) isotropic (I), three aperiodic (APC) and periodic (PC) CrB phases for $d = 0.7$ and b) isotropic, FCC^* and αIrV phases for $d = 0.98$. $\eta = Nv_0/V$ is the packing fraction with v_0 the particle volume, and $P^* = \beta P D_L^3$ is the reduced pressure.

For $d \gtrsim 0.48$ we observe direct APC-isotropic fluid phase transitions upon expansion of the crystal phases. For $d \gtrsim 0.97$ we find that the EOS of αIrV (which is the crystal structure with highest packing in this d range) and the EOS of the FCC^* crystals are the same at low pressure (see Fig. 4.6b), while they differ significantly at higher pressures. This indicates that for these small anisotropies in the sphere diameters, the details of the particle shape become important only at high densities.

We finally note that in some cases we observe crystal-crystal transformations, as explained in Sec. 4.3.1. For the $NaCl$ structures (with $d \gtrsim 0.414$), we see that the modified structure described in the Sec. 4.3.1 converts into the standard $NaCl$ structure upon expansion, with this transformation having no obvious effect on the EOS. Upon recompression we observe the same continuous change from the standard to the modified structure. For the modified αIrV structure (found for $0.75 \lesssim d \lesssim 0.95$) the process is identical, with a reversible continuous transformation from the modified to the standard structure observed.

4.3.3   Phase diagram

We now use the methods described in Sec. 4.2.3 to calculate the free energies of the isotropic fluid phases and the candidate crystal structures. We determine the stable phases at each d value and calculate the coexistence densities at all phase transitions in order to construct the phase diagram of snowman-shaped particles. The predicted phase
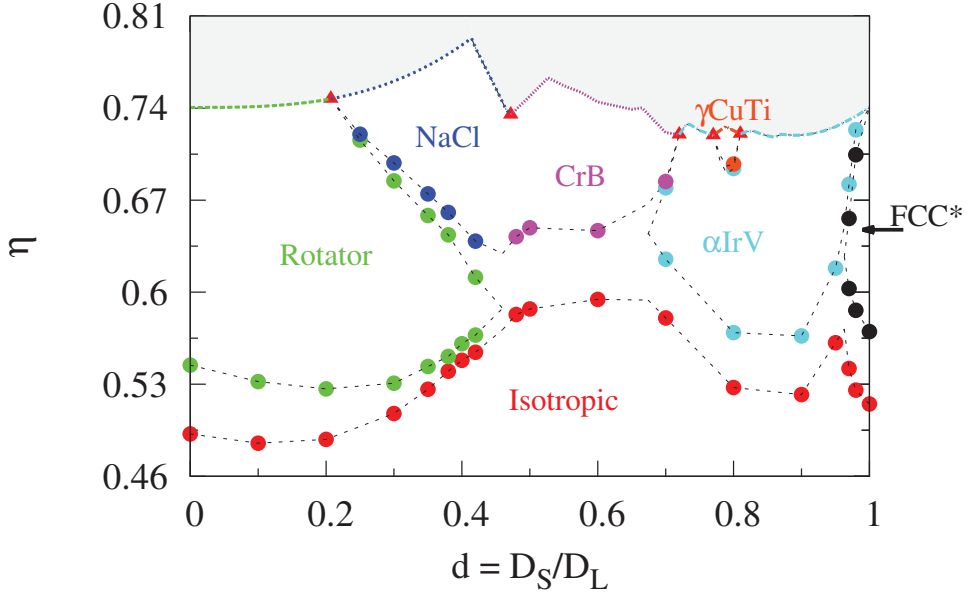
Figure 4.7: Phase diagram of snowman-shaped particles in the $d - \eta$ representation, with $d = D_S/D_L$ ranging from 0 (the hard sphere) to $d = 1$ (the tangential dumbbell) and $\eta = Nv_0/V$ (where v_0 is the snowman volume for a given d value). Circles indicate coexisting phases, while the lines are intended to guide the eye. At the top of the plot we indicate the density of closest packing, with triangles indicating the crossover from one close packed structure to another. Coexistence densities for $d = 0$ are taken from Ref. [66] and for $d = 1$ they are taken from Ref. [78].

diagram is shown in Fig. 4.7. We note that, as stated previously, for non-RC structures studied we find that the stable structures are all orientationally aperiodic. Indeed, we find that the difference between the free energies of the corresponding PC and APC structures is small, and is much smaller then the degeneracy term $\ln \Omega$ (see Eq. (4.9)). As such, from here on all crystalline phases discussed are aperiodic unless stated otherwise.

We predict the existence of stable isotropic fluid and rotator phases for $d \lesssim 0.45$, although the RCs formed during the expansion of candidate crystals for a slightly larger range of d values ($d \lesssim 0.48$). For comparison, in systems of hard dumbbells (with diameter ratio $d = 1$) a rotator phase is stable for sphere separations of $\lesssim 0.38$ [78]. A dumbbell particle therefore has a slightly shorter length of the major axis at the rotator phase triple point than a snowman particle does at the corresponding rotator phase triple point, but has a larger particle volume (~ 1.4 times as large). We note that the RC phase initially becomes slightly more stable with respect to the isotropic phase as d goes from 0 to 0.1, before becoming increasingly less stable at larger d values.

In the region where $d \lesssim 0.2$ we find no further phase transitions (as discussed in

Sec. 4.3.2). For $0.2 \lesssim d \lesssim 0.4$ we predict that the RC transitions into an $NaCl$ crystal structure with increasing density. The range of d values where $NaCl$ phases are stable is roughly the same as the range of size ratios for which $NaCl$ phases were observed to form spontaneously in Ref. [87]. We also see that as d increases the $NaCl$ phases become increasingly more stable with respect to the RC phases. Clearly, as d increases the free energy gain associated with freely rotating particles is diminished as particles interact more strongly during rotations, and hence an orientationally ordered phase is favored.

The behavior in the region $0.4 \lesssim d \lesssim 0.5$ is more complex. At $d = 0.42$ we find both isotropic fluid-RC and RC-$NaCl$ phase transitions, while at $d = 0.48$ we only find an isotropic fluid-CrB phase transition. This leads us to believe that there is a point where the rotator and $NaCl$ phases stop being stable and are replaced by the CrB crystalline phase. By extrapolating our data, we estimate that this point is located at $d \sim 0.46$, which is also close to the point where the CrB structure begins to have better packing than the $NaCl$ structure (at $d \sim 0.47$, see Fig. 4.4).

From $d \sim 0.47$ to $d \sim 0.6$ we find only isotropic fluid-CrB coexistence. At $d = 0.7$ we find that the αIrV phase becomes stable at intermediate densities while the CrB phase is still stable at higher densities, i.e. the phase behavior changes from an isotropic fluid-CrB phase transition to isotropic fluid-αIrV and αIrV-CrB phase transitions. We expect there to be a point where αIrV emerges as the stable phase at intermediate densities, and by extrapolating our results we predict this to be at $d \sim 0.68$. The CrB phase, however, is the best packed structure for $0.47 \lesssim d \lesssim 0.72$, and we thus expect to find an αIrV-CrB phase transition for $0.68 \lesssim d \lesssim 0.72$.

The stability of the αIrV phase in this region can be understood if we consider the effect of degeneracy on the free energy. In Fig. 4.8 we show both the EOS and the free energy F with the degeneracy term $\ln \Omega$ added (see Eq. (4.9)), of both the αIrV and CrB crystalline phases for the system with $d = 0.7$. This allows us to compare the non-degeneracy related contributions to the free energy. As can be seen, the EOS of both systems lie on top of each other at intermediate densities, as do the $F + \ln \Omega$ lines (up to $\eta \sim 0.65$). However, in the αIrV phase there is a larger number of touching large-small spheres ($q = 8$) than in the CrB phase ($q = 6$), which results in a larger number of possible APC structures and therefore a larger $\ln \Omega$ term. This higher degeneracy results in a lower total free energy, and with it the stability of the αIrV phase. Clearly, the orientational degrees of freedom of the snowman particles are responsible for stabilizing the αIrV phase with respect to the CrB phase. This presents an intriguing scenario where we can potentially stabilize binary crystalline phases with respect to other, better packed phases by fusing the spheres to form snowman particles.

For d values larger than ~ 0.72 the CrB phase is no longer the best packed structure and we find the αIrV phase to be the best packed structure up to $d \sim 0.78$. For $0.78 \lesssim d \lesssim 0.81$ we see from Fig. 4.4 that $\gamma CuTi$ has the best packing, and indeed, at $d = 0.8$, based on our free energy calculations, we find this to be the stable structure at high densities. However, at intermediate densities we find that the αIrV phase is still stable, and at lower densities we observe isotropic fluid-αIrV coexistence.

For $d \gtrsim 0.81$ we find that αIrV is again the best packed structure and at high densities we find this phase to be stable all the way up to $d = 1$. At $d = 0.9$ we observe only isotropic fluid-αIrV coexistence, but for $0.9 \lesssim d \lesssim 1$ we also expect a stable FCC^* phase
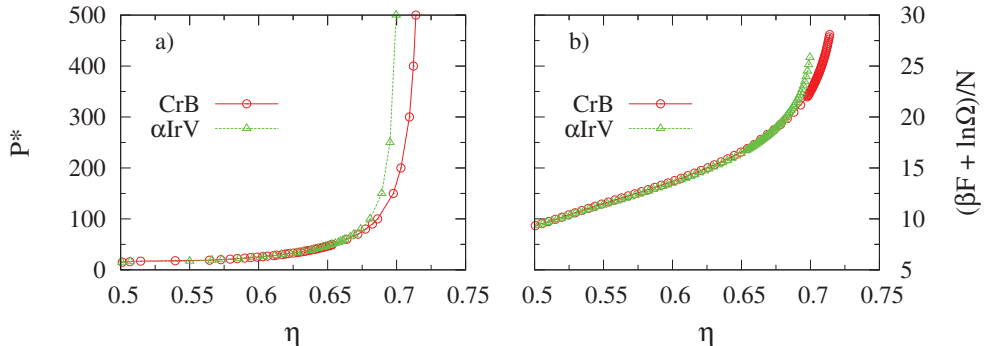
Figure 4.8: Data for CrB (red circles) and αIrV (green triangles) phases of snowman-shaped particle systems with diameter ratio $d = 0.7$. a) Equations of state where $\eta = Nv_0/V$ is the packing fraction with v_0 the particle volume, and $P^* = \beta PD_L^3$ is the reduced pressure. b) Free energy per particle F/N with degeneracy term per particle $\ln\Omega/N$ added (see Eq. (4.9)). For the CrB phase $\ln\Omega/N = 0.8933$, while for the αIrV phase $\ln\Omega/N = 1.1504$ (see Table 4.2).

to emerge at intermediate densities. To check this, we perform free energy calculations for snowman particles with $d = 0.95$, 0.97 and 0.98, finding isotropic fluid-FCC^* coexistence at $d = 0.97$ and 0.98, but not at $d = 0.95$. This closely matches the results of Ref. [87]. We note that the FCC^* phase has a similar EOS at low densities to the αIrV phase (Fig. 4.6b), but has the advantage of a higher degree of degeneracy, which is due to the positional aperiodicity of the constituent spheres as well as the orientational aperiodicity of the composite particle. It is this higher degeneracy that stabilizes the FCC^* phase. As the density is increased, we see from Fig. 4.6b that the αIrV phase becomes better packed than the FCC^* phase, and becomes stable. At $d = 1$, the two phases are identical and are also identical to the aperiodic crystal phase found for tangential hard dumbbells in Ref. [78].

Comparing the structures we have found to be stable for snowman particles with those found for binary hard-sphere mixtures [92, 93, 94, 95, 96, 97, 98], we note that only the $NaCl$ crystal structure is predicted to be stable for binary hard-sphere mixtures with size ratios $d = 0.3$ [97], $d = 0.414$ and 0.45 [93], while the CrB, αIrV and $\gamma CuTi$ structures are never found to be stable. The supplementary information of Ref. [98] lists all the binary crystal structures which are predicted to be stable in the phase diagrams of binary hard-sphere mixtures obtained from full free energy calculations for various size ratios.

4.4   Conclusions

Using Monte Carlo simulations and calculating free energies we have determined the phase diagram of hard snowman-shaped particles. We find the phase behavior of these systems to be extremely rich, with isotropic fluid, FCC rotator crystals, the orientationally aperiodic snowman equivalents of the binary $NaCl$, CrB, αIrV and $\gamma CuTi$ crystal structures and

the snowman-specific FCC^* phases.

At low diameter ratios d we find, along with the isotropic phase, rotator (or plastic crystal) phases. Increasing the diameter ratio suppresses the rotator phase as orientational ordering becomes favored. For intermediate d values we find the above mentioned crystal phases, all of which are orientationally aperiodic. For large d values (as d approaches 1) we find a region where FCC^* phase is stable. We note that all the stable crystalline phases found are orientationally aperiodic as in this way the systems can lower the free energy due to a higher degeneracy, without affecting the packing.

At very high densities we find that the best packed structure is always the stable phase, although in some cases the snowman equivalents of the standard binary crystal structures become modified in order to give better packing. However, at intermediate densities we find that for some d values additional crystalline phases can be stabilized. In such cases we observe that two crystal structures have similar equations of state at intermediate densities, and that the one with the higher degeneracy emerges as the stable phase.

In conclusion, we have shown that the phase diagram of snowman shaped particles is very rich and offers the possibility of forming crystalline phases analogous to and beyond those predicted for binary hard-sphere mixtures.

4.5   Acknowledgments

Appendix

To calculate the number of different ways in which we can connect large and small spheres on a binary crystal lattice in order to obtain a crystal of snowman-shaped particles, we use a method given by Nagle in Ref. [91]. Nagle derives a series expansion for the grand-canonical partition function of systems of monomers and dimers on a lattice by mapping the lattice onto a regular graph G of degree q (i.e. each vertex of the graph is joined by q edges to other vertices). Each term of the expansion series corresponds to a weighted sum of subgraphs G' contained in the original graph G, where the weight of a subgraph is determined by the degrees of its vertices and its number of edges. Any subgraph with a vertex of degree one has, by construction, a zero weight, and hence the expansion will only include the contributions from closed subgraphs.

Obtaining the total free energy βF of a snowman-shaped particle crystal requires adding an additional contribution of $\ln \Omega$ to the free energy of a single crystalline configuration, with Ω denoting the number of different bond configurations of the snowman-shaped particles, i.e. the degeneracy. The grand-canonical partition function for dimers in the limit of close packing corresponds to the degeneracy and can be written as (Ref. [91])

$$\Omega = \Omega_0 \sum_{G' \subseteq G} w(G'). \tag{4.14}$$

The zeroth order term Ω_0 of this expansion reduces to the Bethe approximation, giving the degeneracy of a Bethe lattice. The Bethe lattice is a connected cycle-free graph in which each vertex is connected to q neighboring vertices. In the systems of interest here the zeroth order term depends solely on the number of smaller spheres that touch each larger sphere, i.e. q, and is given by

$$\Omega_0 = q^N \left(1 - \frac{1}{q} \right)^{N(q-1)}. \tag{4.15}$$

The weights $w(G')$ of subgraphs G' which we sum over in Eq. (4.14) are calculated from

$$w(G') = \frac{1}{(q-1)^e} \prod_{p=0}^{q} (1-p)^{v(p)}, \tag{4.16}$$

where e denotes the number of edges in G' and $v(p)$ is the number of vertices of degree p.

In practice, to calculate the degeneracy of a certain lattice using Eq. (4.14), we must calculate the zeroth order term and the sum of weights associated with the closed subgraphs of the original graph corresponding to the lattice. We first identify the subgraphs with a given number of edges e that have a non-zero weight attached to them, and then we count the number of these in the lattice under consideration by generating paths of length e and counting those that are closed. The subgraphs that have to be taken into account when calculating the degeneracy of crystals of snowman-shaped particles are sketched in Fig. 4.9 up to the 8$^{\text{th}}$ order (8 vertices in a subgraph). We note that subgraphs with $e = 3$ and $e = 5$ are forbidden for systems of snowman-shaped particles: $e = 3$ would imply connecting two spheres of the same size, which does not form a snowman particle, and a subgraph with $e = 5$ would have to contain the forbidden subgraph with $e = 3$.
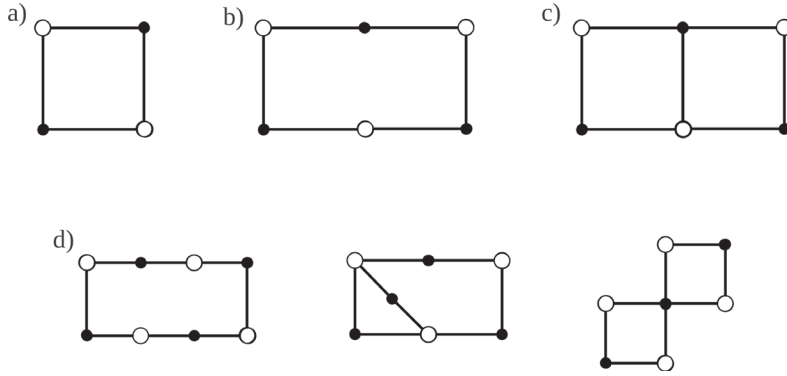
Figure 4.9: Sketch of subgraphs with e edges that have non-zero weights: a) $e = 4$, b) $e = 6$, c) $e = 7$ and d) $e = 8$ edges. Smaller filled symbols represent one species of snowman-shaped particle constituent spheres and larger empty symbols represent the other.

Crystal structures that have the same q value will have the same zeroth order term, but the higher order terms will differ. However, as mentioned in Sec. 4.2.3 we find that the differences between the values obtained from the high order expansion and from the zeroth order term are on the order of a few percent. The calculated values of $\ln \Omega$ are shown in Table 4.2.

5

Phase diagram of hard asymmetric dumbbell particles

Using Monte Carlo simulations and free energy calculations, we study the phase behavior of hard asymmetric dumbbell particles with a constituent sphere diameter ratio of 0.5. We find a rich phase behavior with isotropic fluid, FCC rotator, and periodic $NaCl$-based and both periodic and aperiodic CrB-based crystalline phases. The rotator phases found to be stable in this study are similar to those found in systems of snowman-shaped and dumbbell particles and we investigate the behavior of these phases by comparing their stability ranges, and by looking at the orientational reorganization of particles. We also find that the $NaCl$-based crystalline phase can expand its range of stability by undergoing a slight modification which allows it to pack better. Finally, we see that reducing the sphere separation results in the aperiodic crystalline phases becoming destabilized as compared to the phase behavior of snowman-shaped particles.

5.1   Introduction

With the continual progress of techniques for synthesizing novel anisotropic colloidal particles comes the need to advance our understanding of the phase behavior of these systems accordingly. It is now not only possible to synthesize colloids with simple shapes such as discs [99], rods [100] and cubes [101], but also more complex morphologies such as raspberry-like colloids [62] and octopods [102]. However, predicting the collective system behavior is not trivial, even for simple geometries.

Perhaps the simplest anisotropic particle, which has been the focus of many theoretical [71, 72, 73] and simulation [74, 75, 76, 77, 78, 87, 103] studies, is the dimer. Dimer particles are not only fundamentally interesting, e.g. as a model for diatomic molecules, but also have practical applications, e.g. in the production of colloidal crystals with useful optical properties [104, 105]. Dimers consist of two connected spheres, and they can be synthesized with a range of different constituent sphere diameter ratios and separations [60, 61, 62, 63, 64, 65, 106, 107, 108]. This ability to vary both the diameter ratio of the constituent spheres and their separation results in a vast parameter space, even for dimer particles interacting only via excluded volume.

In Chapter 4 we used computer simulations to map out the phase diagram of hard tangential dimer (snowman-shaped) particles with varying constituent sphere diameter ratios. We found that the stable structures at high densities are colloidal crystals analogous to the best packed structures for equimolar binary hard-sphere mixtures. Specific orientational organization of particles within a crystal was found to have no effect on the packing, and as such crystals with aperiodic ordering of particles are stabilized by the degeneracy entropy. In these tangential systems, the degeneracy entropy also stabilizes additional less well-packed crystalline phases at intermediate densities. For non-tangential dimers, however, periodic ordering of particles can result in better packing than aperiodic ordering, leading to a more complex competition between packing and degeneracy entropy. The effects of this competition are important for understanding the phase behavior of these systems since synthesized dimers are often non-tangential, e.g. because one sphere is 'grown' onto another [62] or arising from techniques such as the lock-and-key [109].

Dumbbells, which consist of spheres with equal diameters and different separations, are a non-tangential dimer particle system which has been widely studied using theoretical and simulation approaches [74, 75, 76, 77, 78]. It has been shown that these particles form aperiodic crystalline phases only for very large constituent sphere separations and also that the underlying structure of the close packed crystalline phase does not change as the constituent sphere separation is reduced [75, 76, 78]. We note that two-dimensional aperiodic colloidal crystals have been experimentally observed in systems of dumbbell particles [110].

In this work we address the question of how varying the sphere separation in systems of hard non-tangential dimer particles with different constituent sphere diameters –which we will refer to as asymmetric dumbbells –affects the phase behavior. Hard-core systems are often used as a reference for systems with more complex interactions as a variety of colloidal and nanoparticle systems behave as nearly hard spheres [98, 111]. Using Monte Carlo simulations and free energy calculations we map out the phase diagram of systems of

asymmetric dumbbells consisting of spheres of diameter ratio $d = 0.5$. This d value allows us to study different aspects of the phase behavior of dimer particles. The tangential particle phase behavior at this diameter ratio is relatively simple, with only isotropic fluid and an aperiodic crystalline phase found to be stable [103]. We can therefore investigate whether reducing the sphere separation can have the same effect on the phase behavior as reducing the diameter ratio, i.e. stabilizing additional crystalline phases. We can also study the range of stability of aperiodic crystals in a system of non-tangential dimers with a constituent sphere diameter ratio much lower than that of dumbbell particles.

The outline of this chapter is as follows. In Sec. 5.2 we briefly describe the simulation methods used and we present the calculated phase diagram in Sec. 5.3.1. In Sec. 5.3.2, 5.3.3, 5.3.4 and 5.3.5 we discuss the behavior and the properties of the various phases which we predict to be stable. Finally, in Sec. 5.4 we present our conclusions and also discuss what we can infer, based on our results, about the phase behavior of asymmetric dumbbell particles with other diameter ratios.

5.2   Method

5.2.1   Model and simulation details

We perform Monte Carlo (MC) simulations on systems of hard asymmetric dumbbell (AD) particles. These particles consist of two hard spheres with a diameter ratio $d = D_S/D_L$, where D_S is the diameter of the smaller sphere and D_L is the diameter of the larger sphere. We define the shape of an asymmetric dumbbell by the reduced sphere separation $L^* = (2L + D_S - D_L)/2D_L$, where L is the distance between the centers of the constituent spheres and we have taken D_L to be the unit of length (see Fig. 5.1). The quantity L^* can be thought of as the length by which the smaller sphere is protruding from the larger one. In the limiting case of $L^* = D_S/D_L$ an asymmetric dumbbell particle reduces to a hard snowman-shaped particle, while for $L^* = 0$ it becomes simply a hard sphere. The phase behavior in both of these limiting cases is known. In this chapter we study systems of AD particles with constituent sphere diameter ratio $d = 0.5$ and reduced sphere separations
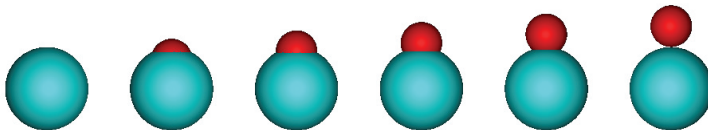

Figure 5.1: Asymmetric dumbbell particles with constituent sphere diameter ratio $d = D_S/D_L = 0.5$ and reduced sphere separation $L^* = (2L + D_S - D_L)/2D_L = 0$ to $L^* = 0.5$, in intervals of 0.1.

$L^* = 0.1$, 0.2 and 0.3, while in the region of $0.3 < L^* < 0.5$, where the phase behavior becomes more intricate, we use a higher resolution.

In order to obtain the equations of state (EOS) for all particle shapes defined by L^* we perform constant pressure Monte Carlo (NPT) simulations on systems of $N \sim 500$ AD particles at pressure P and temperature T. For all L^* values studied we obtain the isotropic fluid branches of the equations of state by increasing the pressure of a dilute isotropic fluid configuration in small steps. The solid branches of the equations of state are calculated in NPT MC expansion runs, where we start by generating a candidate crystal structure at high pressure and then we decrease the pressure slowly until the crystal melts. The crystal structures we consider as candidates are those which were found to be stable in Chapter 4 for hard snowman-shaped particles with a constituent sphere diameter ratio $d \leq 0.5$, namely the structures based on the binary sphere $NaCl$ and CrB crystals. In order to obtain the AD particle candidate crystal structures we begin by generating the corresponding crystals of snowman-shaped particles in which the constituent spheres are tangential ($L^* = 0.5$), using the method described in Chapter 4. We then sink the smaller sphere of each particle into the larger sphere in small steps, equilibrating the intermediate configurations, until we reach the desired L^* value. We note that the positions of the large and small constituent spheres of an AD particle will deviate from the ideal lattice positions of the corresponding binary crystal. To illustrate this, we show examples of the $NaCl$- and CrB-based structures for both snowman-shaped particles and AD particles in Fig. 5.2.

As in the case of systems of dumbbell particles [78] and snowman-shaped particles [103], for AD particle systems it is possible to define three types of ordered structures. These are: rotator phases (RP), periodic crystals and aperiodic crystals. In a rotator phase (also referred to as a plastic crystal in the literature) the particle center of mass positions are on average located on a lattice but the particles can still rotate. Free rotation of a particle can be hindered by the surrounding particles and at high densities correlations between the instantaneous particle positions and orientations can develop [88, 105]. Periodic crystals have both periodic positional ordering of the particle centers of mass and periodic orientational ordering of the particles' major axes, and as such both the small and large constituent spheres are also periodically ordered even for non-tangential AD particles. Finally, for aperiodic crystalline structures the orientations of the particles' major axes are aperiodically ordered, leading to the centers of mass of the particles becoming disordered. We note that in the case of tangential AD particles (snowman-shaped particles) the constituent spheres in an aperiodic structure sit on a lattice, however, as L^* is lowered the sphere positions will deviate non-uniformly from the corresponding binary lattice sites.

The equations of state for the rotator and periodic crystal phases can be obtained from only a single set of expansion runs each, since there is only one representative configuration of each for a given L^* value. For aperiodic structures, however, there are multiple ways in which the particle orientations can be distributed. Hence, for each L^* value we perform expansion runs on a number of different aperiodic crystal structures and average the results to obtain the EOS of each candidate crystal. For tangential snowman-shaped particles it was found that both the aperiodic and periodic structures of a candidate crystal have the same EOS [103]. However, we do not expect this to be the
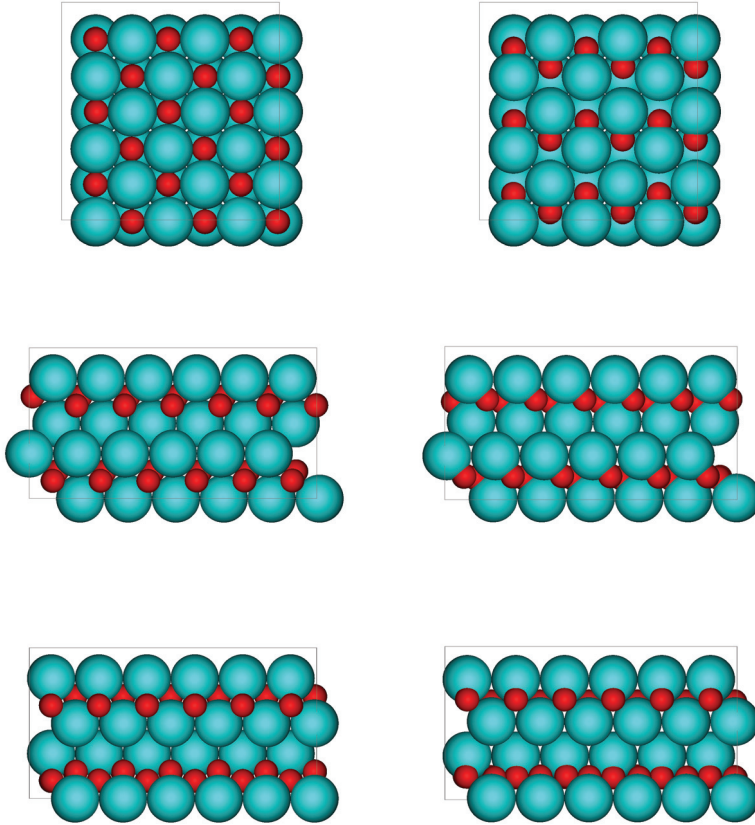
Figure 5.2: Example configurations of $NaCl$ (top row) and CrB (middle and bottom rows, shown in two different planes) crystalline structures for snowman-shaped particles (left-hand column) and asymmetric dumbbell (AD) particles (right-hand column). Blue spheres represent the larger constituent spheres, red represent the smaller ones.

case for asymmetric dumbbell particle systems, since orienting the particles periodically can, in principle, increase the overall density of an AD crystal at fixed pressure.

We finally comment on our choice of periodic configurations of the candidate crystals we use in this study. As the AD particle crystals are made from binary sphere crystals by joining touching large-small sphere pairs, there is clearly more than one way of obtaining periodic ordering. However, based on the results of previous studies of similar systems of dumbbell particles we assume that, if chosen carefully, the specific periodic structure used will not affect the phase boundaries significantly. In Ref. [75] it was shown that three

different types of periodically ordered structures in which the bonds of neighboring dumb-bells are parallel have free energies that are very close to one another (with a difference of $\sim 0.01 k_B T$ per particle). Furthermore, in Ref. [77] it was shown that periodic orderings of dumbbells in which neighboring particle bonds were orthogonal to one another have a significantly higher free energy than the stable structure (up to $\sim 0.7 k_B T$ per particle). Hence, the periodic crystalline structures we study are formed with parallel neighboring bonds.

5.2.2   Free energy calculations

In order to determine which of the candidate crystalline phases are stable and to find the coexistence regions we use free energy calculations. In this section we outline the method we use and for a more detailed description we refer the interested reader to Chapter 4 in which hard snowman-shaped particles were considered.

We calculate the Helmholtz free energy F of an isotropic fluid phase from the chemical potential which we obtain using the Widom particle insertion method [90]. In order to calculate the free energies of each of the candidate crystal structures we use the thermo-dynamic integration method. This method involves integrating the free energy change along a reversible path which links the system of interest to a suitably chosen reference state for which the free energy is known. As the reference state we use a non-interacting Einstein crystal with the same underlying structure [8], and we obtain the lattice site positions and orientations for this crystal by averaging the center of mass positions and orientations of all particles using constant volume MC simulations.

To link the system of interest to the reference crystal we tether the particle positions to the corresponding lattice sites using harmonic springs, and their orientations using a binding potential. We vary the strength of the tethering such that in one limiting case the particles are completely fixed to their lattice sites, while in the other they can move freely. Note that for rotator phases only the particle center of mass tethering is required. In order to complete the transformation from the crystal of interest to the non-interacting Einstein crystal we use a soft potential which allows the particle interactions to be tuned between the hard-core and the interaction free limit. The resulting integration path linking the system of interest to the reference crystal is as follows: the springs are turned on in stages until the particles are fixed to the lattice sites of the reference crystal, then the softness of the particles is gradually increased, through the soft potential, until the system reduces to a non-interacting Einstein crystal. Integrating over this path gives us the free energy at a single state point. In order to account for finite size effects we calculate the free energy for various system sizes N at this state point and extrapolate the results to the thermodynamic limit [112]. Although the original extrapolation method was designed for hard spheres [112], it was shown in Ref. [77] that it also works well for systems consisting of hard dumbbells. Finally, to obtain the free energy as a function of density, we integrate the free energy change over the EOS of the structure of interest.

For aperiodic crystalline structure an additional degeneracy entropy contribution to the free energy has to be taken into account since the different aperiodic realizations have the same free energy. The degeneracy Ω of a particular crystal structure is defined as the number of possible configurations of particle orientations, and for crystalline structures

of AD particles the degeneracy will be the same as for the snowman-shaped particle crystals that they are based on. For the candidate crystalline structures considered here the degeneracy has been calculated in Chapter 4 by following the series expansion method given in Ref. [91]. The zeroth order term, which is equivalent to the Bethe approximation, depends solely on the number of large-small sphere nearest neighbors (defined as q), while the higher order terms are calculated specifically for each lattice. While both the $NaCl$ and CrB lattices have the same q value, it was found in Ref. [103] that the higher order terms differ and hence their degeneracies also differ slightly. For the aperiodic $NaCl$ phase the degeneracy is given by $\ln \Omega/N = 0.8945$ and for the aperiodic CrB phase it is given by $\ln \Omega/N = 0.8933$.

Having calculated the equations of state and the free energies, we determine bulk coexistence densities by equating the pressure and the chemical potential of the two coexisting phases.

5.3   Results

5.3.1   Phase diagram

Using the methods described in Sec. 5.2.2, we have calculated the free energies of isotropic fluid and candidate crystalline phases of asymmetric dumbbell particle systems for a range of reduced AD constituent sphere separations L^*. Based on the obtained free energies we have determined the stable phases, calculated the coexistence densities and, finally, we have constructed the phase diagram shown in Fig. 5.3.

For $L^* = 0$ we recover the phase behavior of pure hard spheres, with stable isotropic fluid and FCC phases. As we go towards higher values of L^*, in the range of $0 < L^* \lesssim 0.207$, the asymmetric dumbbells form only stable isotropic fluid and FCC rotator (or plastic crystal) phases. These rotator phases form spontaneously in MC compression runs and they are characterized by the centers of mass of the particles being located, on average, on FCC crystal lattice sites. At high densities, in order to optimize the packing, this organization changes to the large spheres of the AD particles (instead of the centers of mass of the particles) occupying the FCC lattice sites, with the small spheres still moving within the free space. As we approach close packing, the ADs no longer rotate but become frozen in place.

Moving towards still higher L^* values, with L^* in between 0.207 and ~ 0.35, the phase behavior complicates further, with orientationally periodic $NaCl$ phases found to be stable at high densities. In this L^* region, we expect to find stable isotropic fluid, RP and periodic $NaCl$ phase with increasing density. Moreover, we can see from the phase diagram that, as L^* is increased within this region the periodic $NaCl$ phase becomes increasingly more stable with respect to the rotator phase, as does the isotropic fluid phase. At $L^* = 0.35$ an additional structure –a periodic CrB crystal –emerges as stable. Hence, the expected phase behavior from low to high densities for the system characterized by $L^* = 0.35$ is: isotropic fluid, an FCC rotator (plastic crystal) phase followed by a periodic CrB and finally a periodic $NaCl$. For $0.35 < L^* \lesssim 0.38$ the range of stability of the periodic CrB phase increases, while the density ranges in which the rotator and now also periodic $NaCl$ phases are stable decrease. Finally, at $L^* \sim 0.38$ the FCC rotator phase vanishes
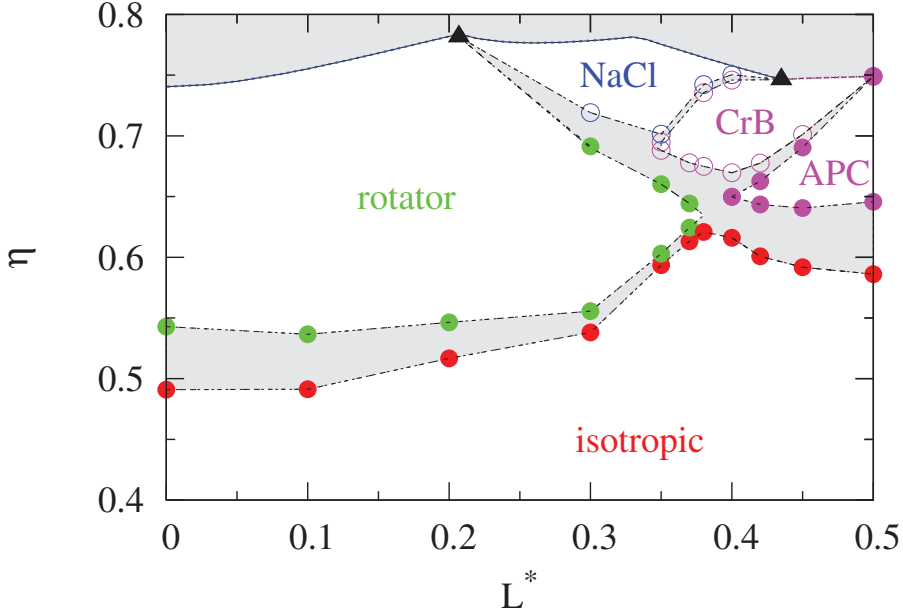
Figure 5.3: Phase diagram of hard asymmetric dumbbell (AD) particles with sphere diameter ratio $d = D_S/D_L = 0.5$ in the $L^* - \eta$ representation, with $L^* = (2L + D_S - D_L)/2D_L$ ranging from 0 (the hard sphere) to $L^* = 0.5$ (the tangential snowman-shaped particle) and $\eta = v_0 N/V$, where v_0 is the volume of an AD particle for a given L^* value and V is the total volume of the system. APC refers to the aperiodic CrB crystal structure, CrB denotes the periodic CrB crystalline phase and $NaCl$ denotes the periodic $NaCl$ crystalline phase. Circles indicate coexisting phases while the lines are intended to guide the eye. At the top of the plot we indicate the density of closest packing, with triangles indicating crossover points from one close packed structure to another. Coexistence densities for $L^* = 0$ are taken from Ref. [113] and for $L^* = 0.5$ they are taken from Ref. [103].

completely and we predict a direct isotropic fluid-periodic CrB phase transition. At high densities a periodic $NaCl$ is still found to be stable, although we note that the structure has become somewhat modified. This will be discussed further in Sec. 5.3.4.

Slightly increasing the value of L^* even further, to $L^* \sim 0.4$, results in the emergence of a stable orientationally aperiodic CrB phase, which we will refer to from now on as APC. The range of stability of this phase grows all the way up to $L^* = 0.5$ at the expense of both the periodic CrB and the isotropic fluid phase. For $L^* > 0.435$ we find that the periodic $NaCl$ phase is no longer stable –this is also where the CrB crystal becomes the best packed structure. Finally, at the snowman-shaped particle limit, corresponding to $L^* = 0.5$, only stable isotropic fluid and aperiodic CrB phases are found [103].

5.3.2   Stability range of rotator phases

A large portion of the phase diagram in this study is dominated by rotator phases –they are found to be stable in the range of $0 < L^* \lesssim 0.38$. Such a large range of rotator phase stability was also found in the similar dimer systems of snowman-shaped particles (SM) [103] and dumbbells (DB) [75, 76, 114]. In this section, we turn our attention to the rotator phase behavior in these systems.

We discuss the phase behavior of the rotator phases in terms of two parameters: the end-to-end length x of a particle and the single particle volume v_0. For the AD particles studied here, the end-to-end length is given by $x = D_L(1 + L^*)$, for SM particles it is given as $x = D_L(1 + d)$, while for DB particles it is given by $x = D_L(1 + L/D_L)$ where L is the distance between the centers of the constituent spheres. In Fig. 5.4 we illustrate these particles for several x values.
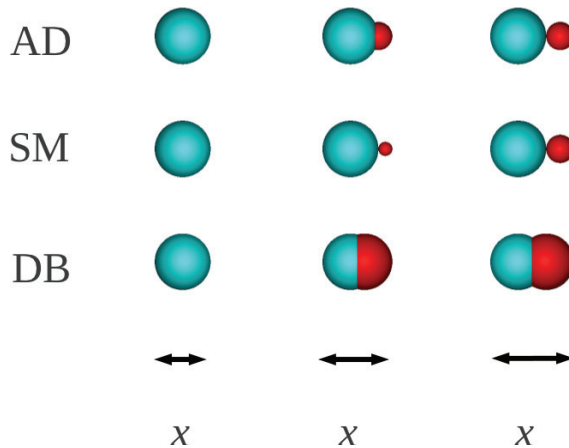

Figure 5.4: Top to bottom: asymmetric dumbbell (AD), snowman-shaped (SM) and dumbbell (DB) particles with end-to-end lengths (from left to right) $x/D_L = 1$, 1.25 and 1.5.

We first note that the particle end-to-end length at which an isotropic fluid-rotator phase transition is no longer observed, and at which a direct fluid-solid transition is found, is similar for all of these systems. This can be seen in Fig. 5.5a, where we show, for the three systems, the phase diagram of the fluid-rotator and rotator-solid phase transitions as a function of the particle end-to-end length. Of the three, the systems of snowman-shaped particles form rotator phases which are stable for a slightly larger particle end-to-end length than in the case of the other two systems, both of which are remarkably close. We also see that the packing fractions at which isotropic fluid-rotator phase coexistence is predicted are lowest for snowman-shaped particles (for a given end-to-end length), followed by the DB and AD particles, while the packing fractions at which rotator-solid
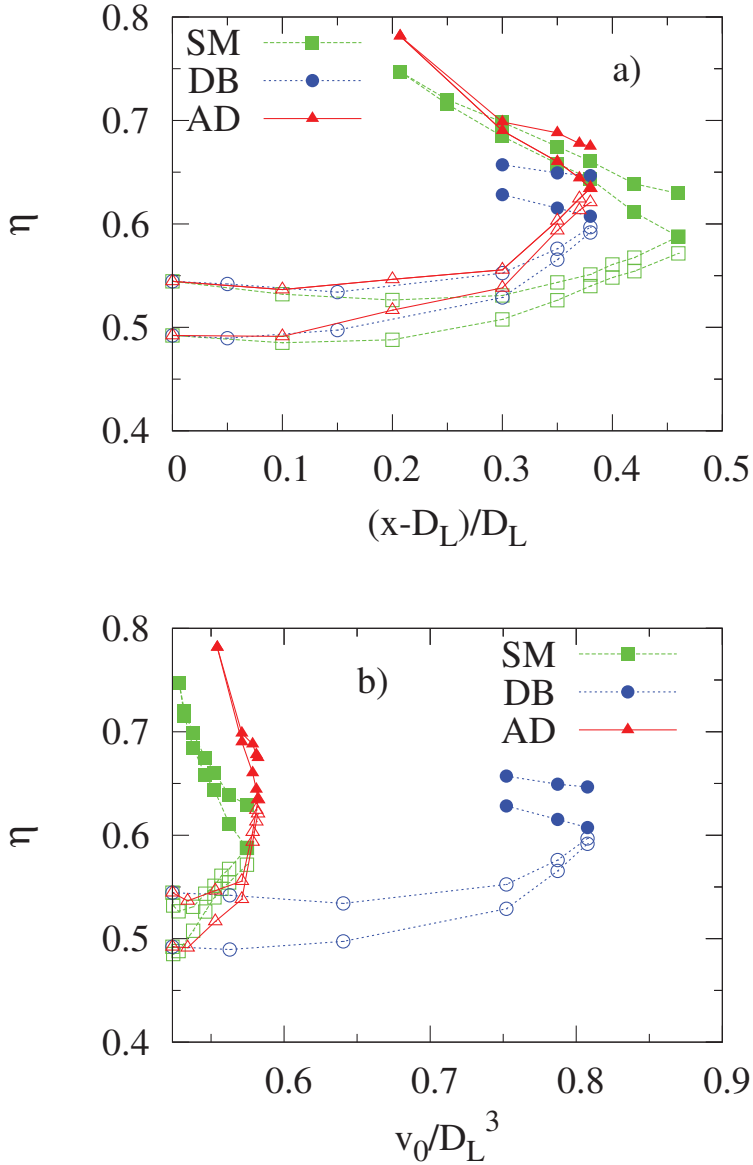
Figure 5.5: Phase diagram showing the isotropic fluid-rotator (open symbols) and rotator-solid (filled symbols) phase transitions in systems of hard dumbbell (DB), hard snowman-shaped (SM) and asymmetric hard dumbbell (AD) particles, as a function of a) reduced end-to-end length of a particle $(x - D_L)/D_L$ and b) particle volume v_0/D_L^3. η denotes the packing fraction; D_L is the unit of length. Data for DB particles are taken from Ref. [114] and for SM particles from Ref. [103].

phase coexistence is predicted are lowest for the DB particles, followed by the SM and AD particles. Consequently, the snowman-shaped particles have the largest packing fraction range for which the rotator phases are stable. This indicates that snowman-shaped particles, which are the only particles consisting of tangential spheres, favor the rotator phase significantly more than the other two systems, in which the constituent spheres are overlapping. The AD particles studied here have an intermediate sized region of stability, while the dumbbells have the smallest. These observations can be understood in terms of the geometry of the different particle shapes. For a given end-to-end length, the dumbbell has the largest volume, which will clearly lead to more interactions between particles at high packing fractions, making free rotation unfavorable. Conversely, the snowman-shaped particles, which have the largest range of the rotator phase stability, are the ones with the smallest volume. In Fig. 5.5b we show the isotropic fluid-rotator and rotator-crystal phase transitions as in Fig. 5.5a, but now as a function of the volume v_0 of a single particle instead of its end-to-end length x. From this, we can clearly see that the volume of dumbbell particles forming rotator phases is much larger than the volumes of the dimer particles in the rotator phases of the other two systems.

In conclusion, we find that the key factor in determining when the rotator phase of a dimer particle system stops being stable is the particle end-to-end length, while the particle volume determines the packing fraction range of stability.

5.3.3   Orientational reorganization

The presence of aperiodic and rotator phases in the phase diagram of asymmetric dumbbell particles is a direct consequence of the AD particles having orientational degrees of freedom. Both of these types of phases are characterized by a degree of orientational disorder which results in an entropy gain that stabilizes them. As discussed previously, for L^* values below ~ 0.207 the only stable ordered structures are the rotator phases, while above this L^* value the stability range of the rotator phases shifts to mid-densities and the $NaCl$ phase emerges as the stable structure at high densities. Thus, we see from the phase diagram in Fig. 5.3 that as L^* is increased the stability range of the rotator phases decreases.

In the case of aperiodic structures the scenario is reversed. They are stable only for large L^* values and their range of stability grows with L^*, until finally at $L^* = 0.5$ the aperiodic structures completely replace the other solids. In these structures, the particles are localized both positionally and orientationally, although the particle orientations are not arranged in any particular way –they form a disordered set –and this is where the gain in entropy, compared to a periodic structure, comes from.

Our aim in this section is to investigate the orientational behavior of the AD particles in rotator and aperiodic phases. To do this, we calculate the first and second order orientational time correlators for a single, randomly chosen particle, over a long MC simulation run. These time correlation functions are given as

$$P_1(t) = \langle \cos\theta(t) \rangle, \tag{5.1}$$

$$P_2(t) = \frac{1}{2}\left\langle 3\cos^2\theta(t) - 1 \right\rangle, \tag{5.2}$$

where $\theta(t)$ is the angle between the initial orientation of the particle and its orientation at time t (given in units of MC cycles) and $\langle \ldots \rangle$ denotes the ensemble average. $P_1(t)$ takes values in the range of -1 to 1, where 1 corresponds to perfect alignment and -1 corresponds to a head-to-tail arrangement. $P_2(t)$ takes values from -0.5 to 1, where 1 again corresponds to perfect alignment and -0.5 indicates an orthogonal arrangement. Generally, we expect both correlators to have a high value for any solid phase and to decay to 0 very quickly for isotropic fluid phases, and we expect the attained values in both of these cases not to change in time. We note here that the rotational motion of non-tangential dimers has previously been studied in dilute suspensions using combined experimental and theoretical techniques [115, 116].

We plot $P_2(t)$ for rotator phases with $L^* = 0.1$, 0.3 and 0.35 in Fig. 5.6. The simulated systems are in all cases at a packing fraction of $\eta \sim 0.64$ which is well inside the stable rotator phase regime. For $L^* = 0.1$, we see that the time correlation function decays rapidly to 0, indicating that the particles are rotating freely. For the intermediate value of $L^* = 0.3$, we see an initial drop in $P_2(t)$ to below 0, followed by fluctuations around 0 until the correlation function finally settles to a value close to 0. The negative value of $P_2(t)$ indicates that the particle is aligned roughly orthogonal to its initial orientation. As the centers of mass of the AD particles are positioned on average on an FCC lattice, and as for $L^* = 0.3$ only one small AD constituent sphere can fit in each of the gaps in between the larger spheres, there are six directions along which an AD particle is on
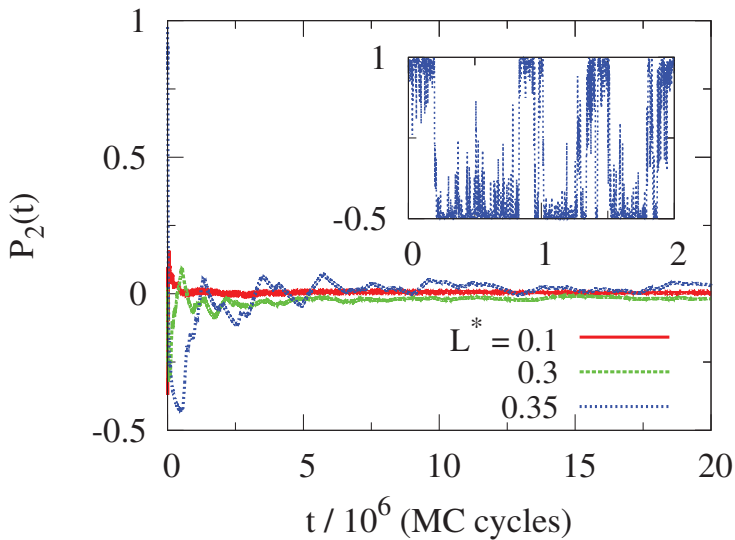

Figure 5.6: Second order orientational time correlation function $P_2(t)$ plotted as a function of simulated time t for asymmetric dumbbell (AD) particle systems with $L^* = 0.1$, 0.3 and 0.35, at packing fraction $\eta \sim 0.64$ at which the systems form stable rotator phases. Inset: $(3\cos^2\theta(t) - 1)/2$ as a function of simulated time for the system with $L^* = 0.35$.

average mostly oriented. Each of these six directions is orthogonal to the neighboring ones, hence, when a particle reorients its new orientation is most likely to be perpendicular to the previous one. The decay to zero of the correlation function at longer times indicates that the particle does not favor any of these directions in particular. For $L^* = 0.35$, the effect is more pronounced. The jagged decay of the $P_2(t)$ line towards 0 indicates that a particle keeps its orientation for a longer time before reorienting again. Further confirmation of this can be seen in the inset of Fig. 5.6, where we show the instantaneous value of $(3\cos^2\theta(t) - 1)/2$. As we can see, the values this function takes are mostly close to -0.5 and 1, which correspond to perpendicular orientations of the particle. Clearly, the distribution of orientations of a single particle in a rotator phase become increasingly non-uniform, i.e. rotation becomes more hindered with increasing L^*, until the rotator phase finally becomes unstable at $L^* \sim 0.38$.

In Fig. 5.7a we plot $P_1(t)$ for a system of AD particles with $L^* = 0.45$ which forms a stable aperiodic CrB crystal at intermediate densities and a periodic CrB crystal at high densities. The periodic structure is stable above $\eta = 0.701$, the aperiodic structure is stable in the region of $\eta = 0.641$ to 0.690, while the isotropic fluid phase is stable below $\eta = 0.592$. The $P_1(t)$ curves plotted here correspond to 4 different densities: a very high density where the stable phase is a periodic CrB (at $\eta = 0.714$), a lower density where we predict a stable aperiodic CrB (at $\eta = 0.648$), a density within the aperiodic CrB-isotropic fluid phase coexistence region (at $\eta = 0.611$), and a density where the system is an isotropic fluid (at $\eta = 0.501$). The correlation function for the system in the isotropic fluid phase decays rapidly to $P_1(t) \sim 0$ as expected. In the periodic and aperiodic crystal structures the orientations of particles are fixed and the correlation functions decay to a constant, high value. This value is slightly lower for the aperiodic structure than for the
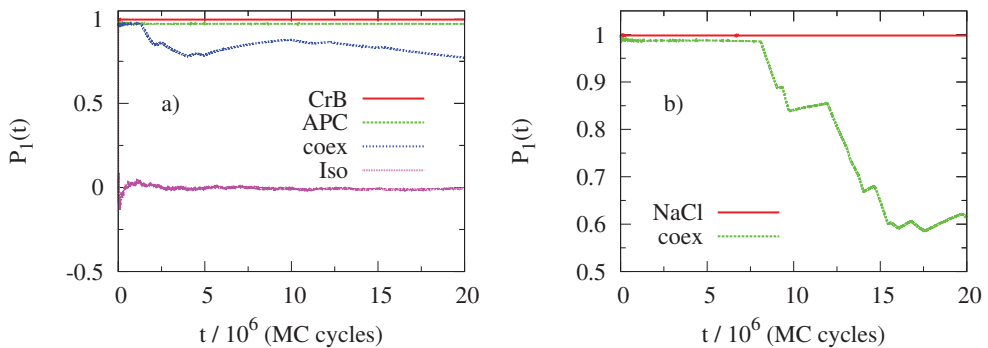

Figure 5.7: a) First order time orientational correlator $P_1(t)$ as a function of simulated time for a system with $L^* = 0.45$ at 4 densities: CrB here indicates periodic CrB phase, APC indicates aperiodic CrB phase, coex denotes the system in the APC-isotropic fluid phase coexistence region, and Iso indicates isotropic fluid phase. b) $P_1(t)$ for a system with $L^* = 0.3$ at 2 densities: $NaCl$ indicates periodic $NaCl$ phase at $\eta = 0.74$, and coex denotes the system in the $NaCl$-rotator phase coexistence region at $\eta = 0.685$.

periodic structure, since the APC is at a lower density, which leaves more free space for fluctuations in the positions and orientations of the particles.

For the system within the aperiodic CrB-isotropic fluid phase coexistence region we see a slow reorganization of particles as the $P_1(t)$ value does not remain constant but instead decays gradually. This metastable structure does not, however, melt completely into the isotropic fluid phase, as the particle orientations remain correlated. Once the orientations of particles within an aperiodic crystal structure are no longer fixed, the crystal can no longer be considered as aperiodic and hence it loses the degeneracy entropy contribution to the free energy. We also see a similar process of orientational reorganization of particles for a system with $L^* = 0.3$ within the periodic $NaCl$-rotator phase coexistence region, as shown in Fig. 5.7b. We note that we only see orientational reorganization of the particles within crystals in the density regions where we have predicted them to be unstable.

5.3.4   Modified $NaCl$ structure

We now turn our attention to the modified $NaCl$ crystal structures found to be stable at very high densities in the reduced sphere separation range of $0.207 \lesssim L^* \lesssim 0.435$, as mentioned in Sec. 5.3.1. The periodic crystal structures we consider are those in which neighboring AD particles are parallel with constituent sphere bonds oriented at 180° to one another, since we find that these structures can pack better than those with parallel bonds oriented at 0°. In an unmodified $NaCl$ structure, each large constituent sphere has 12 large sphere nearest neighbors at high density (4 in each plane). However, in the range of $0.207 \lesssim L^* \lesssim 0.435$, we find that the $NaCl$ structure can, at high pressure, achieve better packing by modifying such that each large sphere now has 6 large sphere nearest neighbors (2 in each plane). This is illustrated in Fig. 5.8. Here, the large spheres along the line denoted by a become slightly separated, to fit the small spheres better, while those along the line denoted by b remain touching. The transformation from unmodified to modified $NaCl$ when compressing a system, as well as from modified to unmodified when expanding, does not result in a noticeable effect on the equation of state. We note that a similar modification was observed in systems of snowman-shaped particles with diameter ratios $d > 0.414$ [103].

To elucidate what the role of this modification is in the stability of the $NaCl$ phase, we calculate the free energy of both the modified and the unmodified $NaCl$ structures at a range of densities. We obtain the unmodified structure at the desired density by simply generating an $NaCl$ configuration at this density, while to obtain the modified structure we uniformly expand an equilibrated close-packed modified configuration to the same density. We then calculate the free energies at each of these state points, and show the results for a system with $L^* = 0.3$ in Fig. 5.9a.

What is immediately apparent is that in the density region for which the $NaCl$ phase was found to be stable, the free energy of the unmodified structure for $L^* = 0.3$ is significantly higher than that of the modified structure. At lower densities the free energies become closer, but only below the coexistence region. For $L^* = 0.35$ we also find that the free energy of the modified $NaCl$ structure is lower than that of the unmodified $NaCl$ in the region of stability. This implies that the stability of the periodic AD $NaCl$ phase is significantly enhanced by this modification, as a higher free energy (corresponding to
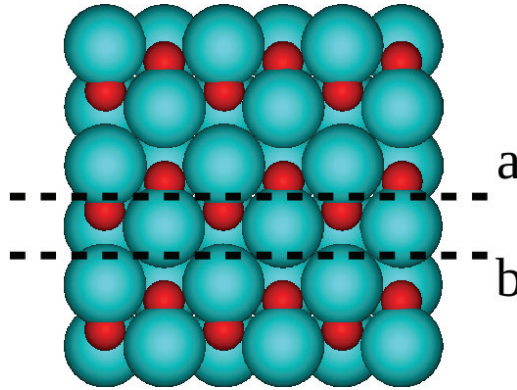
Figure 5.8: Example configuration of the modified $NaCl$ crystalline structure of asymmetric dumbbell (AD) particles with $L^* = 0.3$. Blue spheres represent the larger constituent spheres, red represent the smaller ones. Large constituent spheres along the dashed line denoted by a are slightly separated, while those along the dashed line denoted by b are touching.

the unmodified $NaCl$ structure) would result in the coexistence regions being predicted at higher densities.

Furthermore, when we consider the best packings that the unmodified $NaCl$ structures can achieve in the context of the predicted stability range of the $NaCl$ phase, we see that these are only slightly higher than the packings at which the $NaCl$ phases first become stable. This is shown in Fig. 5.9b. Additionally, it can be seen that the L^* value at which the periodic CrB phase becomes better packed than the $NaCl$ phase is also lower for the unmodified $NaCl$ structure. Hence, while we would still expect the $NaCl$ phase to be present in the phase diagram in the absence of the modification, its range of stability would be significantly smaller.

5.3.5 Destabilizing aperiodic structures

In contrast to the phase behavior predicted for tangential snowman-shaped particles [103], where all stable crystal structures are orientationally aperiodic, for AD particle systems aperiodic structures have only a very small range of stability. A tangential particle system at high density can be thought of as an equimolar binary sphere mixture with certain pairs of touching spheres connected, therefore the constituent spheres in a crystal of snowman-shaped particles will have the same positions in both periodic and aperiodic realizations. What is different is that there are many more ways of constructing the aperiodic crystals, which results in APCs having a higher entropy and with that a lower free energy. However, as we lower L^* below 0.5 (the snowman-shaped particle limit), the constituent sphere positions in the resulting crystals will diverge more and more from their positions on the
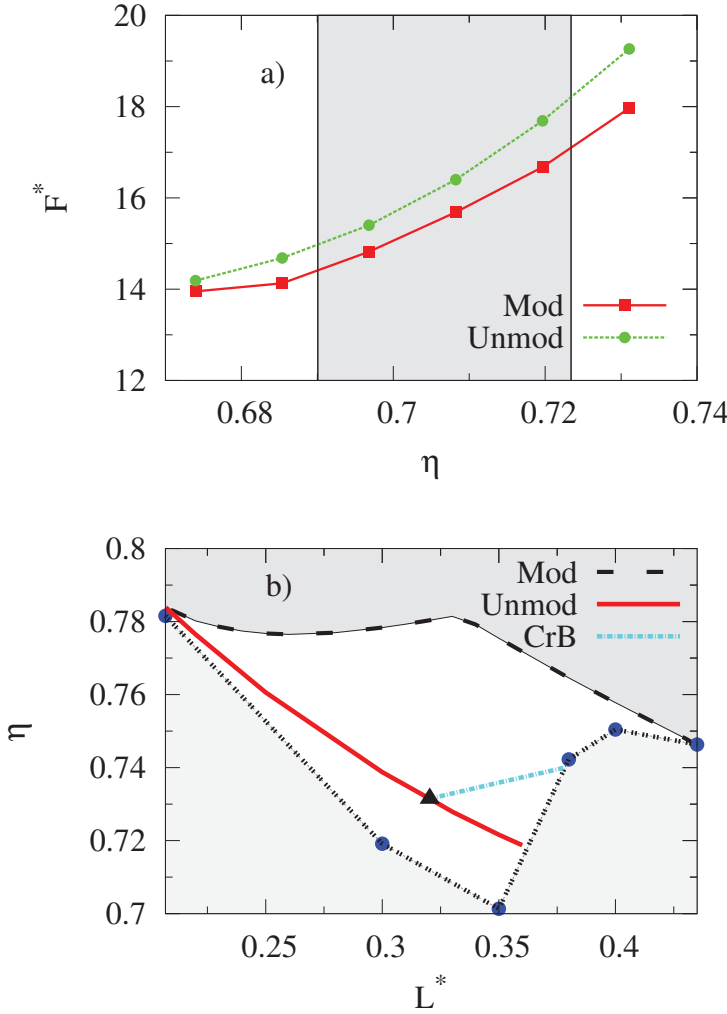
Figure 5.9: a) Free energy per particle $F^* = \beta F/N$ as a function of packing fraction η for both modified (red squares) and unmodified (green circles) $NaCl$ structures for a system of asymmetric dumbbell (AD) particles with $L^* = 0.3$. Shaded region indicates the predicted rotator-modified $NaCl$ coexistence region. b) Density at close packing of the modified (long-dashed black line) and the unmodified (solid red line) periodic AD $NaCl$ structures as a function of L^*. Dashed-dotted line with circles indicates the $NaCl$ melting line. Unshaded region represents the range of predicted $NaCl$ stability. We also include the line of close packing for the periodic CrB structure (short-dashed light blue line). Black triangle indicates the L^* value at which the CrB phase becomes better packed than the unmodified $NaCl$ structure.

corresponding ideal binary lattice. For periodic crystals this distortion of the lattice will be uniform, while for aperiodic structures it will be non-uniform and, as a consequence, the way the particles are oriented will influence the packing.

As an illustration of this behavior, in Fig. 5.10a, we plot the equations of state for both aperiodic and periodic CrB AD particle crystals with $L^* = 0.45$. As we can see, the EOS curves of the 3 aperiodic structures lie on top of each other (within statistical error), while the EOS of the periodic structure shows higher packing for a given pressure at all densities. From the phase diagram (Fig. 5.3) we see that, for the system with $L^* = 0.45$, the APC structure is stable at densities in the range of $0.65 < \eta < 0.69$, even though it is less well packed than the periodic structure in this density range. This indicates that the aperiodic structure in this region is stabilized by degeneracy, i.e. the entropic gain associated with the aperiodicity of the particle orientations outweighs the loss in packing. The importance of the degeneracy can also be seen in Fig. 5.10b, where we show that the free energy per particle is lower at all densities in the periodic phase than in the APC phase if the degeneracy entropy term is removed, while if it is included, the free energy of the aperiodic phase is lower up to $\eta \sim 0.7$.
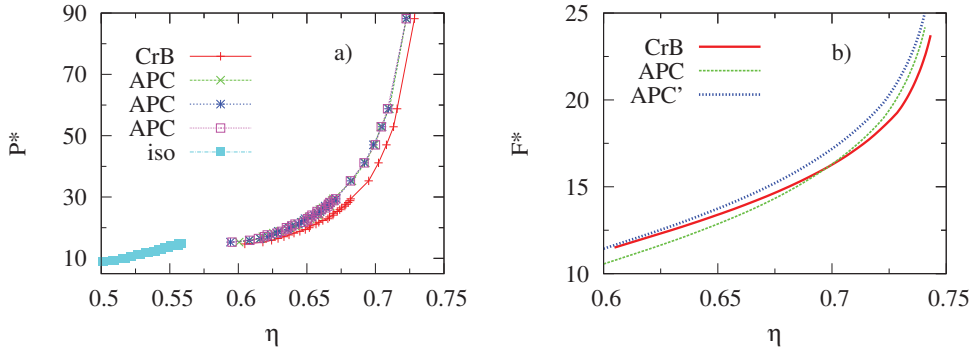

Figure 5.10: a) Equations of state for the periodic and 3 aperiodic structures for the AD CrB based crystal with $L^* = 0.45$. $P^* = \beta P D_L^3$ denotes the reduced pressure and $\eta = \rho v_0$ is the packing fraction, where v_0 is the volume of an AD particle. b) Free energy per particle $F^* = \beta F/N$ as a function of packing fraction η for periodic and aperiodic structures of the CrB-based crystal with $L^* = 0.45$. CrB denotes the free energy of the periodic and APC the free energy of the aperiodic phase. APC' denotes the free energy of the aperiodic phase without the degeneracy entropy term: $F^* = (\beta F + \ln \Omega)/N$.

5.4 Conclusions

We have investigated the phase behavior of systems of hard asymmetric dumbbell particles with a fixed constituent sphere diameter ratio of $d = 0.5$, using Monte Carlo simulations

and free energy calculations. The particle shapes studied here range from the snowman-shaped particle to the hard sphere. At the snowman-shaped particle limit, only isotropic fluid and aperiodic CrB phases were predicted to be stable. Reducing the separation of the constituent spheres of the AD particles results in the phase behavior becoming more complex, as we now find stable isotropic fluid, FCC rotator (plastic crystal), periodic $NaCl$ and both periodic and aperiodic CrB phases.

For low sphere separations, we predict FCC rotator phases to be stable for a large region of the phase diagram. We compare this region to the ranges of stability of the rotator phases in systems consisting of hard snowman-shaped and dumbbell particles, as these three shapes belong to the same class of hard-sphere dimer particles. We find that the particle end-to-end length at which the rotator phases are no longer present in the phase diagram is similar in all cases. This indicates that the end-to-end length is more important for destabilizing the rotator phases of dimer particles than the individual particle volumes, since these vary greatly between the three systems. We also see that, as the sphere separation of the AD particles is increased, free rotation of the particles in a rotator phase becomes increasingly hindered by the surrounding particles, until the rotator phase finally becomes destabilized.

For intermediate values of the sphere separation, we predict a periodic $NaCl$ phase to be stable at high densities. However, the observed crystal structure is not the standard, but instead a slightly modified $NaCl$ crystal and we find that the origin of this modification lies in the tendency of the system to optimize its packing, i.e. in this way the $NaCl$ phase achieves better packing at very high pressures. The modification extends significantly the range of stability of the $NaCl$ phase. We confirm this by calculating and comparing the free energies of the modified and unmodified $NaCl$ structures, and also by comparing the best possible packing of the unmodified $NaCl$ to that of the modified $NaCl$ and CrB structures.

At high values of the asymmetric dumbbell constituent sphere separation, as we approach the snowman-shaped particle limit, we find a region in which aperiodic phases are stable. We note that the range of stability of the aperiodic crystals of asymmetric dumbbells is significantly smaller than in the case of snowman-shaped particles, where all predicted crystalline phases are orientationally aperiodic. This suppression of aperiodicity in systems of asymmetric dumbbells (as compared to the phase behavior of snowman-shaped particles) is due to the positions of the constituent spheres deviating from the crystal lattice sites as the sphere separation is reduced. The density is no longer invariant to the orientation of the particles and the degeneracy entropy is not always sufficiently large to overcome the free energy gain arising from the better packing of periodic structures.

Finally, we discuss what we can infer from our results about the general phase behavior of asymmetric dumbbell particles. Based on the present work and previous studies of snowman-shaped and dumbbell particles we would always expect a rotator phase to be present in the phase diagram of systems of dimers with small diameter ratios and/or sphere separations. We would also expect that reducing the sphere separation, compared to tangential particles with the same sphere diameter ratio, will at first destabilize the aperiodic structure, as the periodic ordering of particles will give better packing. This will not be the case for $d < 0.414$, since the $NaCl$ structure predicted to be stable for

tangential dimers in this d range will have the same packing for periodic and aperiodic structures as the separation is reduced. It is also possible that as the sphere separation is reduced the best packed crystalline phase will change relative to that of the corresponding tangential particle system. This can lead to the appearance of an additional stable phase at high densities, although we note that for dumbbell particles no additional structures were found to be stable, indicating that this will be the case only for certain sphere diameter ratios.

5.5 Acknowledgments

6

Phase behavior of dumbbell-shaped particles with long-ranged repulsions

In this chapter we study the phase behavior of systems of hard-core repulsive Yukawa dumbbells using Monte Carlo simulations. We characterize these systems by different interaction parameters, finding that dumbbells with sufficiently long-ranged repulsive interactions under compression crystallize spontaneously into plastic crystal phases. By examining the local bond order parameters we identify the underlying structure of the particle centers of mass as a BCC crystal lattice for all the plastic crystals obtained. We also calculate the auto- and spatial orientational time correlation functions which reveal, in contrast to the behavior of plastic crystal phases in hard-particle systems, that the particle rotations are not hindered even for the shortest ranged interactions we study.

6.1   Introduction

Building a colloidal system to suit a fundamental study or a particular technological application requires the ability to design its properties. This generally implies being able to choose the composition and the characteristics of the particles in the system, since their sizes, shapes and interactions will determine the behavior of the system and the way it responds to different external influences, both on microscopic and macroscopic scales. The simplest model system, that has been extensively studied using experiments, theory and simulations, is the system of spherical particles interacting via excluded volume. In equilibrium, hard spheres form only two stable phases: a fluid and a crystal phase [66]. Hence, obtaining more complex behavior on the macroscopic level clearly requires the chosen building blocks to have more complex properties.

The range of particle shapes that can be synthesized nowadays is extensive (see e.g. Refs. [100, 117, 118, 119]), as is the range of different interactions that can be attained in experimental setups (e.g. Refs. [120, 121]) and also the range of different techniques used to study colloidal systems. Recently, a particle tracking algorithm that can be used to determine both positions and orientations of anisotropic particles based on confocal microscopy images has been developed [122]. Using this algorithm it was demonstrated that systems of anisotropic particles with added long-ranged repulsive interactions can form structures that exhibit long-ranged positional but no orientational order. These properties are characteristic of plastic crystals, or rotator phases as they are also referred to in the literature. In addition, the underlying structures of the observed plastic crystals were characterized as body centered cubic (BCC) lattices, i.e. long-ranged repulsive anisotropic particles can form BCC based plastic crystal phases.

In an attempt to model this behavior in computer simulations, in this chapter we use dumbbell-shaped particles as model anisotropic particles. They are composed of spheres of diameter σ with center-to-center separation of 0.5σ, making the shape such that in the hard interaction limit these particles do not form rotator phases, but, instead, form fully positionally and orientationally ordered structures [78]. To the hard-core shape we add long-ranged repulsive interactions, modeled here by hard-core repulsive Yukawa potentials, and we study the structures that these systems form as a function of the interaction parameters. As we make the range of the particle interactions longer their effective aspect ratio will become shorter, and we expect to start observing plastic crystal phases as the systems are compressed.

The hard-core Yukawa potential is essentially an interaction model potential for charged spherical particles based on the DLVO theory [123, 124], with attractive van der Waals forces neglected. In this model, the thickness of the double layer is taken into account through the choice of the screening length, and it is also possible to adjust the charge of the particles. The expected phase behavior of charged spherical colloids with this model Yukawa potential has been predicted for inverse screening lengths $\kappa\sigma$ in the range of 2 to 10 (see Ref. [125]). These systems were found to form both stable FCC and BCC phases. In this work we introduce a degree of particle shape anisotropy and study a larger range of screening lengths, expecting to observe the formation of plastic crystal phases with the particle centers of mass on FCC and/or BCC lattices. Our aim is to investigate if this simple model system is indeed suitable for studying real systems of long range repulsive

anisotropic particles as seen in experiments [122, 126]. To this end we study the phase
behavior of the simulated system by examining both the behavior of the centers of mass
and the orientations of the dumbbell-shaped particles.

6.2 Model and method

We use Monte Carlo simulations to study systems consisting of N dumbbell particles which
interact via a long-ranged repulsive potential. The dumbbell particles are composed of
spheres of diameter σ, with a center-to-center distance $L = 0.5\sigma$. The constituent spheres
are taken to be the sites of the model interaction potential such that the pair interaction
of two dumbbells is the sum of pair interactions of their constituent spheres. The site-site
pair potential that we use here is a hard-core repulsive Yukawa potential which is given
by

$$\beta U_{ia,jb}(r) = \begin{cases} \epsilon \dfrac{exp[-\kappa\sigma(r/\sigma - 1)]}{r/\sigma} & r > \sigma, \\ \infty & r < \sigma, \end{cases} \tag{6.1}$$

where r denotes the distance between sphere $a = 1, 2$ of dumbbell i and sphere $b = 1, 2$ of
dumbbell j, $\beta = 1/k_B T$, with k_B denoting the Boltzmann constant and T the temperature;
the inverse Debye screening length is denoted by κ and ϵ is the contact value of the pair
potential. We keep the value of $\epsilon = 81$ throughout and study a range of potentials with κ
values such that $1/\kappa\sigma$ varies from 0.1 to 0.9 in steps of 0.1. When simulating systems with
this model potential it is also necessary to choose the cut off distance of the potential,
r_{cut}, and we take this to be the point when the potential falls below $0.01 k_B T$ for each of
the $1/\kappa\sigma$ values. The screening lengths and the cut off values of the potentials studied
in this chapter are summarized in Table 6.1 and a sketch of the potentials is given in
Fig. 6.1.

$1/\kappa\sigma$	$\kappa\sigma$	r_{cut}/σ
0.1	10.0	1.85
0.2	5.0	2.6
0.3	3.33	3.6
0.4	2.5	4.0
0.5	2.0	4.7
0.6	1.67	5.4
0.7	1.43	6.0
0.8	1.25	6.7
0.9	1.1	7.4

Table 6.1: Values of the hard-core repulsive Yukawa potential parameters used in this study:
dimensionless Debye screening length $1/\kappa\sigma$ and the potential cut off distance r_{cut}.

To investigate the phase behavior, we perform constant pressure Monte Carlo (NPT
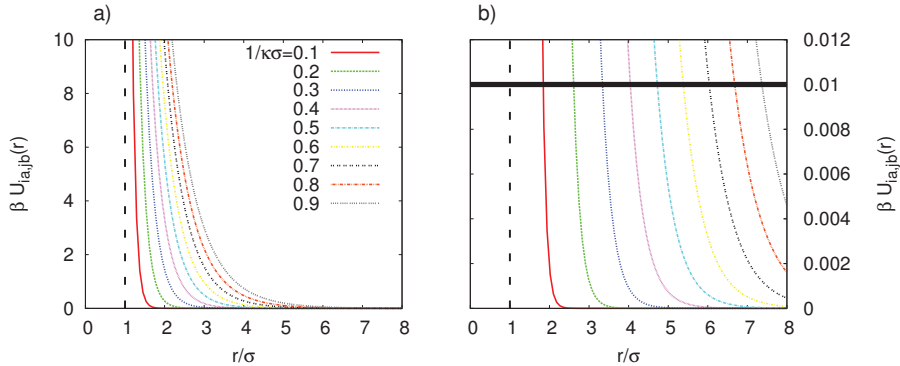MC) simulations on systems consisting of both $N = 432$ and $N = 500$ dumbbell particles

Figure 6.1: a) Site-site hard-core repulsive Yukawa potential plotted as a function of distance for screening lengths $1/\kappa\sigma$ ranging from 0.1 to 0.9 in steps of 0.1. Dashed vertical line represents the hard-core limit. b) The same as in a), focusing on the region close to the potential cut off r_{cut} for each of the $1/\kappa\sigma$ values used. The potential cut off is taken to be the distance at which the pair potential falls below $0.01k_BT$. The bold horizontal line corresponds to $\beta U_{ia,jb} = 0.01$.

interacting with potentials defined by the $1/\kappa\sigma$ values listed in Table 6.1. Since we are interested in the bulk phase behavior of these systems, we employ periodic boundary conditions in all directions and keep the shape of the simulation box cubic. We start the simulations from a dilute isotropic fluid configuration which we then compress in steps, equilibrating each system at each pressure reached. The particle numbers we study are chosen such that we make sure that our results are not biased towards the formation of one particular crystal structure, since a given number of particles in a simulation box would favor the formation of a crystal structure with the commensurate number of lattice sites. In addition, 432 and 500 particles are commensurate with BCC and FCC crystal structures contained in a cubic box and will hence minimize the amount of defects that might be present in crystals that form spontaneously during simulation runs. Finally, when simulating systems with long-ranged particle interactions it is also necessary to make sure that the simulation box size is always large enough so that the particles do not interact with their own periodic images, i.e. the box dimensions cannot be smaller then twice the potential cut off value r_{cut}.

6.2.1   Locating transitions

In order to determine when an initial isotropic fluid configuration forms a crystalline structure, we use the local bond order parameter which was introduced by Ten Wolde in Ref. [127]. To calculate the value of this order parameter we start by compiling a list of neighboring particles for each particle. The neighbors of particle i are taken to be all particles located within a spherical shell of radius r_c centered on particle i, and we denote their total number as $N_b(i)$. Then, for each particle i we define the bond orientational order parameter as a $2l + 1$ dimensional vector given by

$$q_{l,m}(i) = \frac{1}{N_b(i)} \sum_{j=1}^{N_b(i)} Y_{l,m}(\theta_{i,j}, \phi_{i,j}),$$

(6.2)

where $Y_{l,m}(\theta_{i,j}, \phi_{i,j})$ are spherical harmonics with $m \in [-l, l]$, $\theta_{i,j}$ and $\phi_{i,j}$ are the polar and azimuthal angles of the vector $\mathbf{r}_{ij} = \mathbf{r}_i - \mathbf{r}_j$ giving the distance between the centers of mass of particle i and one of its neighbors j. Next, for each particle and all of its neighbors, we calculate the normalized dot products of the bond orientational order vectors as

$$d_l(i,j) = \frac{\sum\limits_{m=-l}^{l} q_{l,m}(i) q_{l,m}^*(j)}{\left(\sum\limits_{m=-l}^{l} |q_{l,m}(i)|^2 \right)^{1/2} \left(\sum\limits_{m=-l}^{l} |q_{l,m}(j)|^2 \right)^{1/2}},$$

(6.3)

and based on the $d_l(i,j)$ values we define the number of connections of particle i as

$$n_{con}(i) = \sum_{j=1}^{N_b(i)} H(d_l(i,j) - d_c),$$

(6.4)

where $H(...)$ denotes the Heaviside step function and d_c is the dot-product cut off. Each particle i with the number of connections $n_{con}(i)$ larger than a certain threshold value n_{con}^c is characterized as a solid particle. Finally, to obtain a measure of how solid the whole configuration is, we calculate the percentage of solid particles, expecting it to be ~ 0 for an isotropic fluid configuration and ~ 1 for a solid configuration.

In practice, to check for 6-fold FCC ordering we calculate the bond order parameter with $l = 6$, and we also need to choose suitable values for the free parameters r_c, d_c and n_{con}^c. Since we wish to identify only the nearest neighbors of any given particle, we take r_c to be the r value of the first minimum of the radial distribution function for the configuration under consideration. We then calculate the bond order parameter using a range of values for the dot-product cut off d_c and threshold number of connections n_{con}^c, finding no qualitative difference in the behavior of the order parameter for a d_c range of 0.5 to 0.9 and for an n_{con}^c range of $5-9$. Hence, in this chapter we present results obtained with $d_c = 0.7$ and $n_{con}^c = 7$.

While the analysis described above can be used to differentiate between liquid and solid phases it does not provide information on the type of crystalline structure under consideration. In order to be able to make a distinction between crystals typically found in systems of spherical particles (note: we are only interested in translational order of the particles' centers of mass when determining the underlying crystal structure of a plastic crystal phase) we also use the local bond order parameter in a different form. A method introduced in Ref. [128] and later used for structure differentiation in e.g. Refs. [129, 130, 131, 132], proposes averaging the bond order parameter in such a way as to take into account the particles contained in not just the first but also the second shell around a reference particle. The proposed averaged form of $q_{l,m}(i)$ is

$$\bar{q}_{l,m}(i) = \frac{1}{\widetilde{N}_b(i)} \sum_{j=1}^{\widetilde{N}_b(i)} q_{l,m}(j), \tag{6.5}$$

with the sum from $j = 0$ to $\widetilde{N}_b(i)$ running over all the neighbors of particle i including the particle itself. The averaged local bond order parameter then becomes

$$\bar{q}_l(i) = \sqrt{\frac{4\pi}{2l+1} \sum_{m=-l}^{m=l} |\bar{q}_{l,m}(i)|^2}. \tag{6.6}$$

To identify the crystal structure we calculate both $\bar{q}_4$ and $\bar{q}_6$ as it has been shown in Ref. [128] that the distributions of these averaged order parameters can be used to distinguish between different crystalline structures.

6.2.2 Orientational correlations

The order parameters described in Sec. 6.2.1 enable us to determine when the centers of mass of the dumbbells become ordered and which type of crystalline structure they assemble. However, for a complete characterization of a structure formed by anisotropic particles it is also necessary to investigate the behavior of their orientational degrees of freedom. While the particles are expected to rotate freely in a fluid phase, the orientations of the particles may become fixed when the particles' centers of mass crystallize. In this case we would characterize the obtained structure as an orientationally ordered solid. However, if the particles would still be able to rotate freely while their centers of mass are on average positionally ordered, we would characterize the obtained structure as a plastic crystal. In order to investigate orientational correlations as the systems evolve, we calculate the orientational time correlation functions $P_1(t)$ and $P_2(t)$ for a single randomly chosen particle from

$$P_1(t) = \langle \cos\theta(t) \rangle, \tag{6.7}$$

$$P_2(t) = \frac{1}{2} \left\langle 3\cos^2\theta(t) - 1 \right\rangle, \tag{6.8}$$

where $\theta(t)$ is the angle between the initial orientation of the particle and its orientation at time t (given in units of MC cycles) and $\langle \ldots \rangle$ denotes the ensemble average. Both of these time correlators are expected to have a high value for any solid phase and to decay to 0 very quickly for isotropic fluid phases. For plastic crystal phases the rate of decay of the correlators can give an indication of how free the particle rotations are – a very rapid decay to zero would indicate completely free rotation while slow decay would indicate a degree of rotational hindrance.

To investigate the spatial correlations of the particle orientations, we calculate

$$g_2(r) = < P_2(\mathbf{u}(0) \cdot \mathbf{u}(r)) > \tag{6.9}$$

where $P_2(x)$ represents the 2nd Legendre polynomial, $\mathbf{u}(r)$ is the orientation unit vector of a particle located at a distance r from the reference particle, and $\langle \ldots \rangle$ denotes the ensemble

average [133]. This spatial orientational correlation function enables us to investigate the degree of correlation of the particle orientations as a function of the distance in the system: for a solid phase we would expect to find long ranged orientational order, while this would not be the case for a freely rotating phase.

6.3 Results

6.3.1 Equations of state

In Fig. 6.2 we present the equations of state (EOS) as obtained in NPT MC compression runs for systems consisting of both $N = 500$ and $N = 432$ particles and each of the interaction potentials determined by the $1/\kappa\sigma$ values given in Table 6.1. As we can see, the obtained EOS for both system sizes with a given $1/\kappa\sigma$ value are the same within statistical error. Also, the equations of state do not indicate the presence of any phase transitions as the systems are compressed, remaining apparently smooth over the density range we have studied. Inspection of the simulation snapshots, however, reveals that positional ordering of the particles' centers of mass does emerge for all the systems studied, except those interacting with the potential defined by $1/\kappa\sigma = 0.1$. This suggests that any change in density during the transition must be small. We note that we have also performed NPT
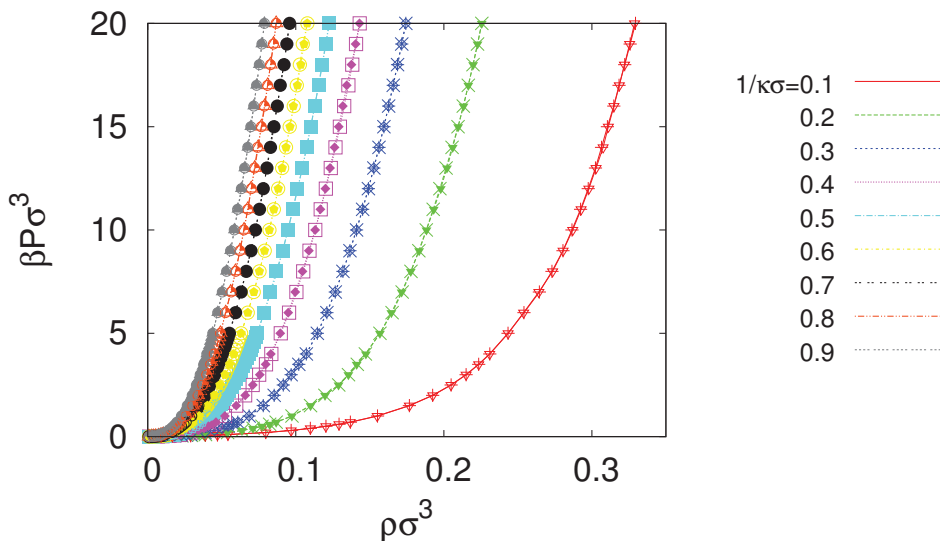

Figure 6.2: Equations of state (EOS) of systems consisting of both $N = 500$ and $N = 432$ site-site repulsive hard-core Yukawa dumbbell particles for all $1/\kappa\sigma$ values given in Table 6.1. $\rho\sigma^3$ denotes the dimensionless number density and the EOS are shown up to the reduced pressure $\beta P\sigma^3 = 20$; σ denotes the diameter of a constituent sphere of a dumbbell.

MC compression runs on systems contained in simulation boxes of variable shape. These showed identical EOS to the ones presented here, although the simulation box was found to readily deform due to the long range nature of the interaction potentials, rendering further structural analysis more difficult.

6.3.2   Translational order

When compressed, most of the systems studied here exhibit long-ranged positional order of the centers of mass of the dumbbell particles, as mentioned in Sec. 6.3.1. Our goal in this section is to investigate if and at what density the transition from a fully disordered to a positionally ordered phase occurs for the range of model potentials we are considering. Additionally, we wish to identify the crystalline structures formed by the particles' centers of mass. We note that, as we are only interested in the ordering of the particles' centers of mass in this section, we do not consider their orientations.

We begin by calculating the radial distribution functions of the particles' centers of mass for all the simulated systems, and in Fig. 6.3 we show examples of these for the systems with $N = 432$ particles interacting with potentials defined by $1/\kappa\sigma = 0.2$ (Fig. 6.3a) and $1/\kappa\sigma = 0.8$ (Fig. 6.3b). The radial distribution functions shown here were calculated at two densities for each system: one at a density where the simulation snapshots do not show any positional ordering and the other at a density at which positional ordering is present. From the plots in Fig. 6.3 we see that the radial distribution functions, $g(r)$,
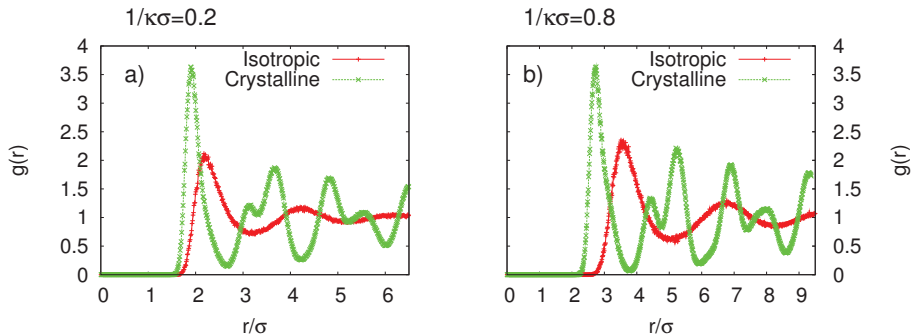

Figure 6.3: Radial distribution functions $g(r)$ of the centers of mass of repulsive hard-core Yukawa dumbbell particles calculated from simulations of systems consisting of $N = 432$ dumbbells. The radial distribution functions are plotted as a function of distance r at two different densities for systems interacting with potentials defined by: a) $1/\kappa\sigma = 0.2$ and b) $1/\kappa\sigma = 0.8$. Isotropic denotes the radial distribution functions at reduced density $\rho\sigma^3 = 0.0972$ for the system with $1/\kappa\sigma = 0.2$ and $\rho\sigma^3 = 0.0259$ for the system with $1/\kappa\sigma = 0.8$, at which the systems are in an isotropic fluid phase. Crystalline denotes positionally ordered phases, plotted for reduced density $\rho\sigma^3 = 0.1888$ for the system with $1/\kappa\sigma = 0.2$ and $\rho\sigma^3 = 0.0651$ for the system with $1/\kappa\sigma = 0.8$.

have the same properties for both interaction potentials shown: characteristic of fluid
phases at lower densities and more structured (exhibiting split peaks) in ordered phases.
The distances at which the first peaks and the minima occur are, as expected, larger for
the system with particles interacting via a more long-ranged repulsion (i.e. $1/\kappa\sigma = 0.8$).
We note that the radial distribution functions exhibit qualitatively the same behavior for
all $1/\kappa\sigma \geq 0.2$. In addition, since the radial distribution functions were calculated using
configurations obtained in MC compression runs, and since their behavior is qualitatively
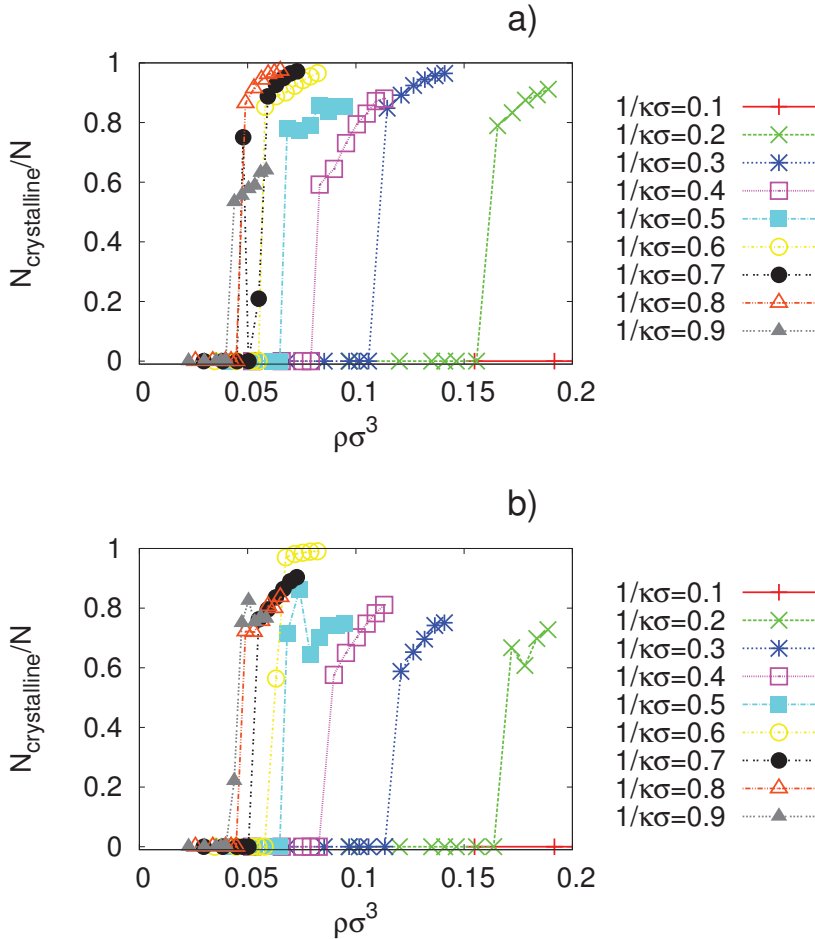

Figure 6.4: Fraction of crystalline particles in a system as a function of the reduced number
density $\rho\sigma^3 = N\sigma^3/V$, where N is the number of particles and V the volume of the system,
shown for $1/\kappa\sigma$ values in the range of $0.1 - 0.9$ in steps of 0.1 and: a) $N = 432$ and b) $N = 500$
particles.

the same in positionally ordered phases for all $1/\kappa\sigma$ values, we expect the ordered phases which form spontaneously in the compression runs to have the same underlying structure.

In order to systematically distinguish between isotropic fluid phases and positionally ordered structures in the systems under consideration, for each of them (i.e. for both system sizes and for all the screening lengths listed in Table 6.1) we calculate the local bond order parameter q_6 for the center of mass of each particle and determine the number of crystalline particles in a configuration using the method described in Sec. 6.2.1. These calculations were performed for each system for a range of particle number densities along the equation of state, and the values were averaged over 100 equilibrated configurations for each density. The obtained results for the average fraction of crystalline particles at
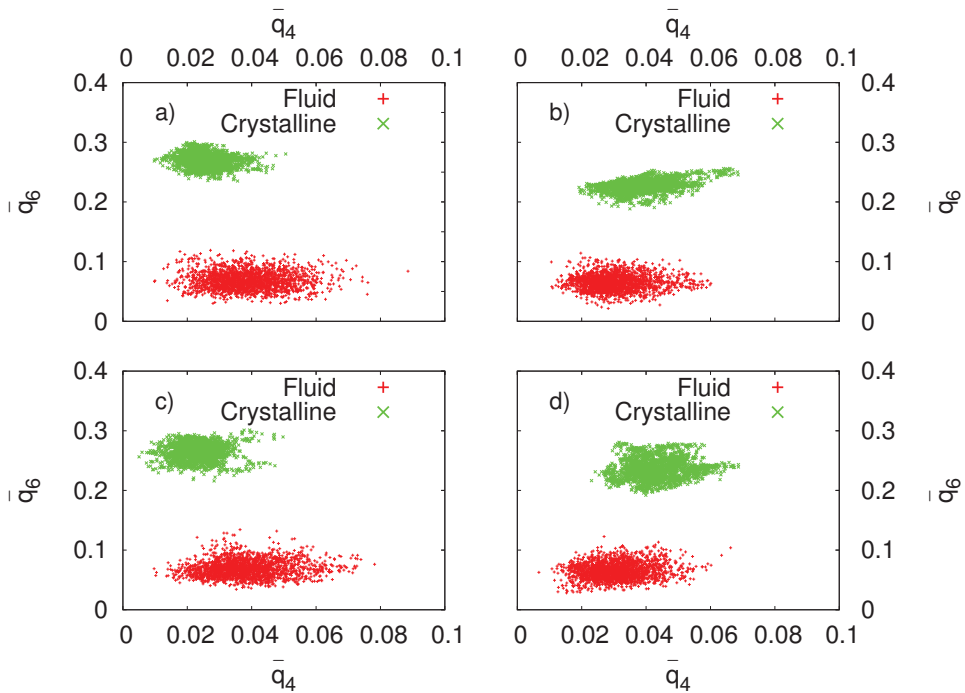

Figure 6.5: Averaged order parameters $\bar{q}_4$ and $\bar{q}_6$ shown in $\bar{q}_4 - \bar{q}_6$ representation for systems with: a) $N = 432$, $1/\kappa\sigma = 0.2$; b) $N = 432$, $1/\kappa\sigma = 0.9$; c) $N = 500$, $1/\kappa\sigma = 0.2$ and d) $N = 500$, $1/\kappa\sigma = 0.9$. Each $(\bar{q}_4, \bar{q}_6)$ point represents the values of $\bar{q}_4$ and $\bar{q}_6$ for a single randomly chosen particle, and we show 2000 points for each phase. Fluid denotes that the system is in an isotropic fluid phase, crystalline denotes the phases in which the particles' centers of mass are on average positionally ordered on a BCC lattice. The data plotted here are calculated on systems at a reduced pressure $\beta P\sigma^3 = 1$ for the fluid phases and $\beta P\sigma^3 = 10$ for the crystalline phases [128].

each state point are shown for systems with $N = 432$ in Fig. 6.4a and for systems with
$N = 500$ in Fig. 6.4b. As we can see, the fraction of crystalline particles exhibits a sharp
jump for all systems except those with $1/\kappa\sigma = 0.1$. We also see that these jumps take
place at slightly lower number densities for systems with $N = 432$, and that the fractions
of crystalline particles achieved are mostly lower in systems with $N = 500$ than in those
with $N = 432$ particles. This indicates that 432 is the preferred number of particles,
i.e. it is commensurate with the number of lattice sites of the structure forming in a
cubic simulation box. Since the positionally ordered phases form spontaneously while
the systems are undergoing compression, and since the density jumps at coexistence are
known to be very narrow for long-ranged repulsive interactions [125], we can use the
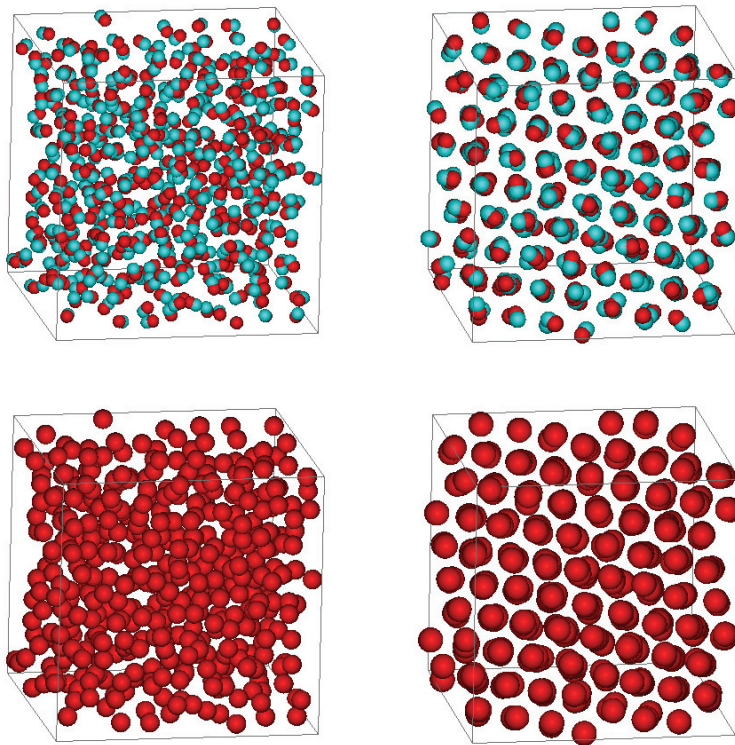abrupt changes in the crystallinity fraction to locate the fluid-solid transitions.

Figure 6.6: Simulation snapshots of the system with $N = 432$ particles and $1/\kappa\sigma = 0.4$.
Top row: particles represented by dumbbells with constituent spheres of diameter σ and sphere
separation 0.5σ. Bottom row: particles represented by spheres of diameter 1.5σ placed at the
dumbbell centers of mass. Left column shows an isotropic fluid phase, right column shows a
positionally ordered phase with dumbbell centers of mass located on average on a BCC lattice.

To investigate what the underlying structures of the formed crystalline phases are, we follow Ref. [128] and calculate averaged order parameters $\bar{q}_4$ and $\bar{q}_6$. The obtained results are shown in Fig. 6.5 in the $\bar{q}_4 - \bar{q}_6$ plane for systems with 2 different $1/\kappa\sigma$ values and both system sizes. Each point in these plots represents the values of $\bar{q}_4$ and $\bar{q}_6$ for a single particle, and we plot 2000 points randomly chosen from the configurations of the simulated systems in each phase. For all the systems we see two clearly distinct regions: one where the values of both $\bar{q}_4$ and $\bar{q}_6$ are small, typically $\lesssim 0.1$, and one where the values that $\bar{q}_4$ takes remain small but the distribution of $\bar{q}_6$ moves to higher values. The first region corresponds to a fluid phase and the second to a BCC crystalline phase, as identified in Ref. [128]. Clearly, BCC phases form in systems with both $N = 432$ and $N = 500$ particles, even though the latter number of particles is not commensurate with a BCC lattice contained in a cubic box. This indicates strongly that BCC is the stable ordered phase of the particles' centers of mass, and we expect the crystals forming in systems with $N = 500$ particles to have more defects than those forming in systems with $N = 432$ particles.

As an example of the BCC phases that form spontaneously under compression in the systems we study, in Fig. 6.6 we show simulation snapshots of both the isotropic fluid and the positionally ordered phase for the system with $N = 432$ particles and $1/\kappa\sigma = 0.4$. We show the particles represented by dumbbells with constituent spheres of diameter σ and also as spheres placed at the dumbbell centers of mass (shown spheres have a diameter equal to the length of the above dumbbells, i.e. 1.5σ). Representing the dumbbells as spheres allows us to see more clearly the underlying structure of the crystalline phase, as only the particle centers of mass, and not the constituent spheres, appear to be ordered. However, visualizing the particles as dumbbells allows us to see the degree of orientational ordering in the system. The apparent absence of orientational
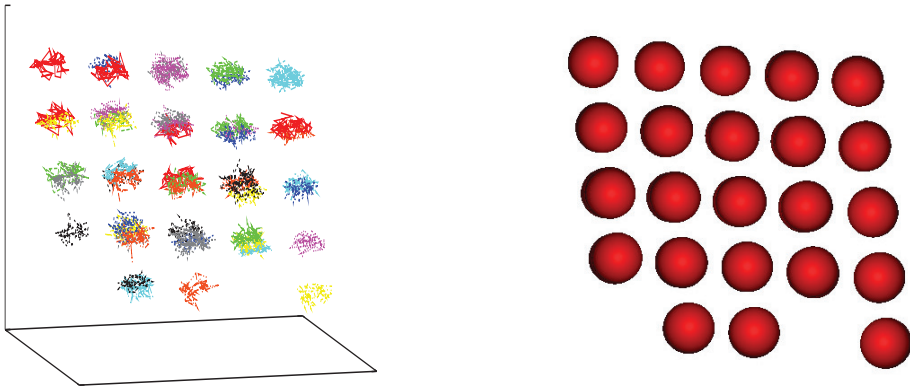

Figure 6.7: Left: the fluctuations of the particle centers of mass around their ideal lattice positions for the system with $1/\kappa\sigma = 0.4$ at a reduced number density $\rho\sigma^3 \sim 0.11$. Right: the averaged configuration for the same system.

ordering seen in our simulation snapshots indicates that the formed BCC phases are most likely to be BCC based plastic crystal phases, consistent with the experimental observations of BCC rotator phases in systems of charged anisotropic particles [122, 126]. We will investigate the orientational behavior of the particles further in Sec. 6.3.3.

From the snapshots shown in Fig. 6.6 we can see that there is a large amount of free space between the dumbbell particle hard cores in the formed BCC plastic crystals. This is consistent with the distances at which the first peaks appear in the radial distribution functions, as shown in Fig. 6.3, and with what we would generally expect to see in the crystalline phases of particles interacting via long range repulsive potentials. In Fig. 6.7, we show the trajectories that the particle centers of mass make during a simulation run along with the averaged center of mass configuration for a system with an intermediate $1/\kappa\sigma$ value of 0.4. From the trajectories we see that the fluctuations of the centers of mass cover a relatively large volume indicating that the particles have a high degree of positional freedom, although their averaged positions form a very regular lattice.

6.3.3   Orientational degrees of freedom

In the previous section we examined the translational behavior of the particle centers of mass in our systems, and determined that for all $1/\kappa\sigma \geq 0.2$ they form BCC crystalline structures. An initial inspection of simulation snapshots (see Fig. 6.6) reveals no specific organization of particles' orientations. In this section we wish to examine the orientational behavior of the particles in these systems in more detail.
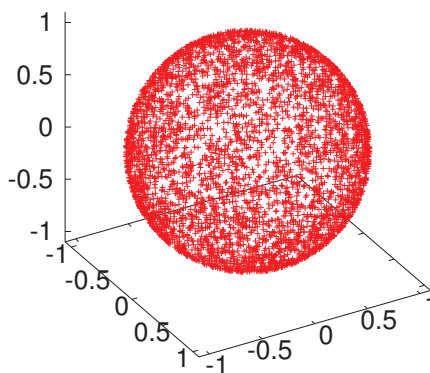

Figure 6.8: Distribution of unit vector orientations of a single randomly chosen particle over a long simulation run in a system with $1/\kappa\sigma = 0.2$ at a reduced pressure $\beta P\sigma^3 = 10$ in a positionally ordered BCC phase.

In Fig. 6.8, as an example, we plot the unit vector orientations of a single randomly chosen particle in a system with $1/\kappa\sigma = 0.2$ during a simulation run. The distribution of the unit vector orientations on the surface of a sphere again shows no preference for any specific direction. This would imply that the resulting crystalline phases are indeed BCC plastic crystal phases. In Fig. 6.9a we show the orientational time correlator $P_1(t)$ and in Fig. 6.9b we show $P_2(t)$ calculated using Eq. (6.8) for a randomly chosen particle. The correlators are shown for $1/\kappa\sigma = 0.1$, 0.2 and 0.9, where the correlation functions for the system with $1/\kappa\sigma = 0.1$ are calculated for a generated BCC phase while those for $1/\kappa\sigma = 0.2$ and 0.9 are calculated from the spontaneously formed BCC phases. As we can see, all the calculated correlation functions show a rapid decay to zero indicating that the particles are free to rotate in these phases, even for the shortest ranged interaction studied ($1/\kappa\sigma = 0.1$). We note that in Chapter 5 we found that rotator phases of hard dumbbell-shaped particles can become hindered and hence show orientational correlations over long times, which is clearly not the case for these long-ranged repulsive interactions. The large inter-particle spacing that is present in the long-ranged repulsive systems studied here allows for the free rotation of the particles in the positionally ordered structures we observe.
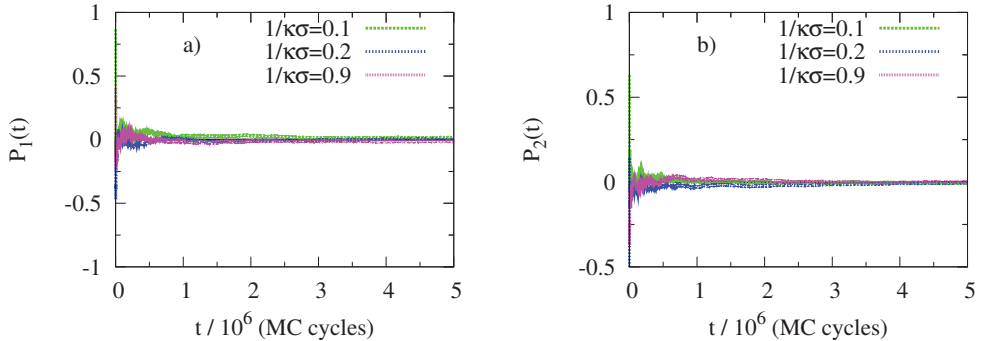

Figure 6.9: Orientational time correlation functions for a randomly chosen particle in systems with $1/\kappa\sigma = 0.1$, 0.2 and 0.9 at a reduced pressure $\beta P\sigma^3 = 10$ in a positionally ordered BCC phase. a) $P_1(t)$ and b) $P_2(t)$ as a function of time t given in units of MC cycles.

In order to examine spatial correlations between particle orientations in BCC rotator phases we calculate the orientational correlation functions $g_2(r)$ from Eq. (6.9). We show examples of these in Fig. 6.10 for systems with $1/\kappa\sigma = 0.1$, 0.2 and 0.9; as before, the data for $1/\kappa\sigma = 0.1$ is taken from an expansion run of a generated BCC phase. As can be seen, none of the systems shown exhibit strong correlations, even for the most short ranged interaction studied. Our results also indicate the absence of long-ranged correlations between particle orientations, as all the correlation functions decay to zero quickly. We do however observe a small, but pronounced, peak indicating the presence of some correlation between nearest neighbor particles. In addition, as the screening length
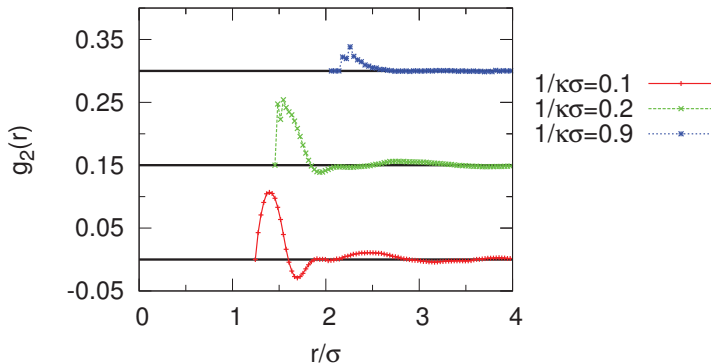
Figure 6.10: Orientational pair correlation functions $g_2(r)$ calculated for systems with $N = 432$ and $1/\kappa\sigma = 0.1$, 0.2 and 0.9 at reduced pressure $\beta P\sigma^3 = 10$ in a positionally ordered BCC phase. The plotted curves are offset by 0.15 in the y direction for clarity.

$1/\kappa\sigma$ is reduced, the peak becomes larger and moves to shorter distances, as we would expect. For the shortest screening length we also observe a region of anticorrelation following the first peak. We would expect that any further reduction of the screening length would result in the particle orientations becoming more strongly correlated and also over larger distances, and hence free rotation would become increasingly hindered until it is completely suppressed.

6.3.4 Phase diagram

In Figs. 6.11 and 6.12 we summarize our findings in the form of phase diagrams with $1/\kappa\sigma$ plotted against the pressure and also the number density of the system. The phase diagrams include the data from NPT MC compression runs using $N = 432$ particles, which we discussed in previous sections, together with data from additional NPT MC expansion runs. The expansion runs were performed in order to obtain the melting curves of the crystals, and to do so we begin by generating a perfect BCC lattice with 432 lattice sites. We then place the dumbbell particles on the sites such that their centers of mass are on the lattice and their orientations are chosen randomly, and we expand these systems in NPT MC simulations in small steps. To determine when the crystals melt, we use the local bond order parameter in the same way as was done in Sec. 6.2.1 for the compression runs.

From the plots in Figs. 6.11 and 6.12 we can see that the densities at which the rotator phases are first observed become progressively lower as we increase the screening length of the potential. A larger screening length implies that the particles will interact while still at relatively large distances and hence, in order to minimize its potential energy, the system will adopt positional ordering of the centers of mass at a lower density. We can also see that the crystal phases retain positional ordering when expanded to densities

below those at which we observe spontaneous crystallization during compression. This is particularly pronounced for the system with $1/\kappa\sigma = 0.1$ where we observe a rotator phase only in the expansion runs, although it melts at relatively low densities. Below the melting density of the generated BCC crystal the stable structure will certainly be an isotropic fluid, while above the densities at which the systems spontaneously crystallize we expect the stable structures to be BCC based rotator phases: the regions in between these two densities, for each $1/\kappa\sigma$ value, will contain the phase coexistence regions. We expect the coexistence regions to be very narrow since we do not observe any abrupt changes in the equations of state, similar to what was found in Ref. [125] for spherical hard-core Yukawa particles. Finally, we note that in contrast to the predicted phase behavior for systems of spherical particles interacting via hard-core Yukawa potentials with similar screening
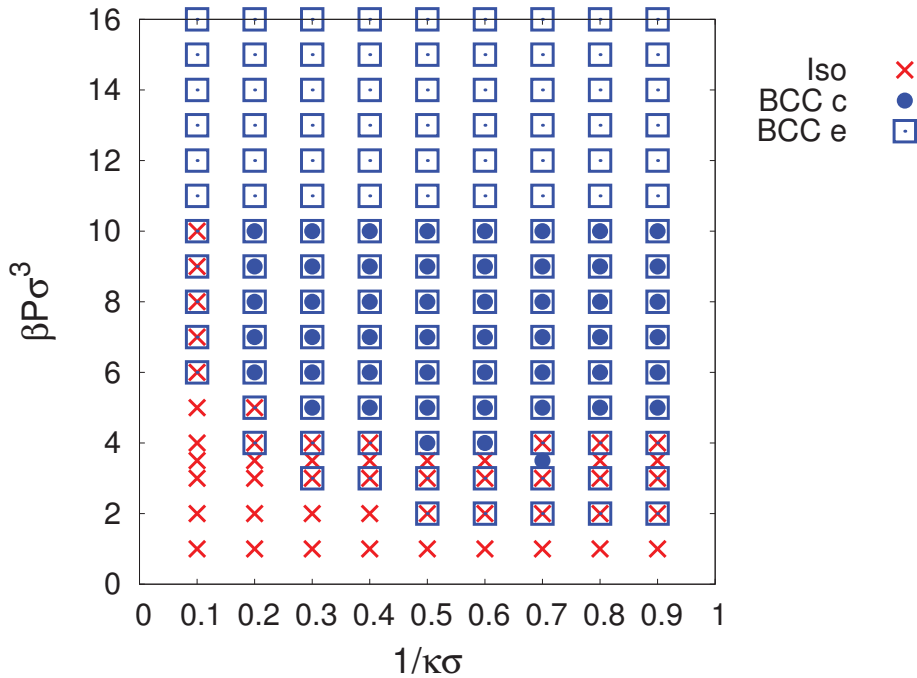

Figure 6.11: Phase diagram for a system of dumbbell particles interacting via a site-site hard-core repulsive Yukawa potential. The presented results are obtained in NPT MC simulations of $N = 432$ particles with $1/\kappa\sigma$ values listed in Table 6.1 and with $\epsilon = 81$. The phase behavior for each screening length $1/\kappa\sigma$ is shown as a function of reduced pressure $\beta P\sigma^3$ in the system. Red crosses (Iso) denote points where we observe isotropic fluid phases when compressing the system, filled blue dots (BCC c) represent points where we find BCC plastic crystal phases formed in compression runs, and open blue squares (BCC e) represent the points where the systems which start from an initial BCC plastic crystal remain crystalline in expansion runs.

lengths [125], for the anisotropic particles studied here, we never observe the formation of an FCC crystalline phase. For the ϵ value used in this work, based on the results for spherical hard-core Yukawa particles, we would expect to see an isotropic fluid-FCC phase transition at least for $1/\kappa\sigma \lesssim 0.25$ (which would only shift to higher $1/\kappa\sigma$ values for higher ϵ).
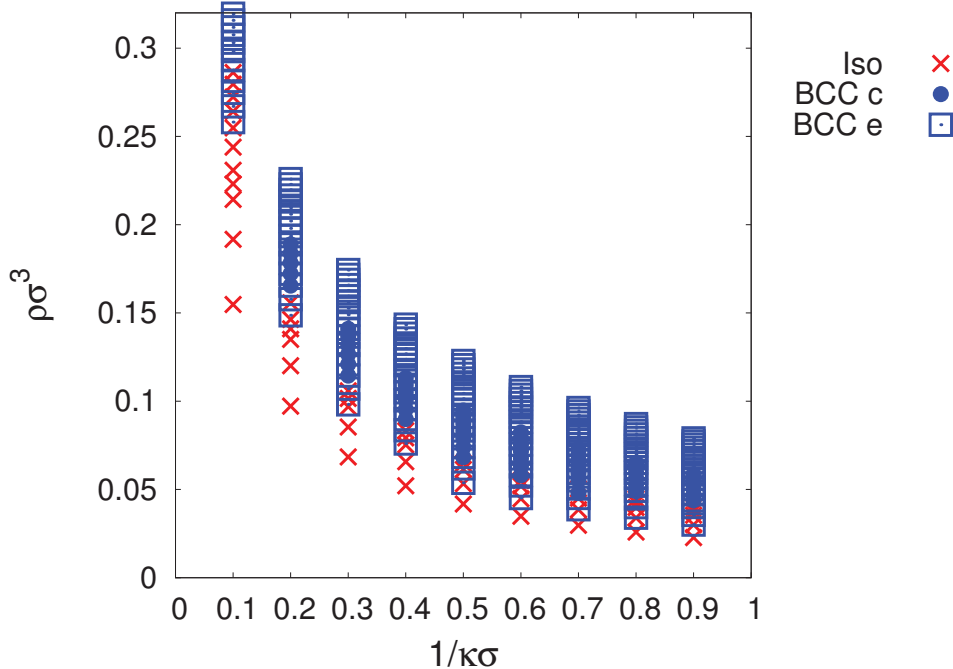

Figure 6.12: Phase diagram for a system of dumbbell particles interacting via a site-site hard-core repulsive Yukawa potential. The presented results are obtained in NPT MC simulations of $N = 432$ particles with $1/\kappa\sigma$ values listed in Table 6.1 and $\epsilon = 81$. The phase behavior for each screening length $1/\kappa\sigma$ is shown as a function of reduced number density $\rho\sigma^3$ of the system. Symbols are the same as in Fig. 6.11.

6.4   Discussion and conclusions

Using computer simulations we have investigated the phase behavior of a range of systems interacting via long range repulsive potentials. The studied systems consist of anisotropic dumbbell-shaped particles, and to model their interactions we use site-site hard-core repulsive Yukawa potentials with a range of different screening lengths $1/\kappa\sigma$. We find that, when compressed in simulation runs, systems with $1/\kappa\sigma \geq 0.2$ spontaneously form rotator

phases with the particle centers of mass positioned on average on a BCC lattice. We have also found that the rotations of the particles in these phases are not hindered.

Hard dumbbell particles with the same constituent sphere separation as those studied here (0.5σ) do not form stable rotator phases [78], and hence our simulations demonstrate how long ranged repulsive interactions can stabilize rotator phases of anisotropic particles. The shape anisotropy introduced here also alters the underlying crystal structure in the ordered phases: it was predicted in Ref. [125] that spherical particles interacting via hard-core Yukawa potentials with $0 < 1/\kappa\sigma \lesssim 0.25$ and $\epsilon = 81$ would form FCC, and not BCC phases. Closer examination of the behavior of the particles' orientations in the BCC rotator phases reveals no considerable auto-correlations nor spatial correlations, indicating that for the range of potentials studied here the particles are indeed rotationally free. This is in contrast to the rotator phases found in systems of hard particles (see Chapter 5).

Although we would not expect the model system used here to fully capture the behavior of a real system of charged dumbbell-shaped particles and to account for it quantitatively, our results indicate that it can, however, qualitatively reproduce the phase behavior observed experimentally in systems of anisotropic particles interacting via long-ranged repulsions.

References

[1] R. Jones, *Soft Condensed Matter*. Oxford: Oxford University Press, 2002.

[2] E. Bianchi, R. Blaak, and C. Likos *Phys. Chem. Chem. Phys.*, vol. 13, pp. 6397–6410, 2011.

[3] S. Sacanna, W. Irvine, P. Chaikin, and D. Pine *Nature*, vol. 464, p. 575, 2010.

[4] P. Damasceno, M. Engel, and S. Glotzer *Science*, vol. 337, pp. 453–457, 2012.

[5] A. van Blaaderen *MRS Bulletin*, vol. 29, pp. 85–90, 2004.

[6] N. Metropolis, A. Rosenbluth, M. Rosenbluth, A. Teller, and E. Teller *J. Chem. Phys.*, vol. 21, p. 1087, 1953.

[7] B. Alder and T. Wainwright *J. Chem. Phys.*, vol. 27, p. 1208, 1957.

[8] D. Frenkel and B. Smit, *Understanding Molecular Simulation*. London: Academic Press, 2002.

[9] D. Frenkel and A. Ladd *J. Chem. Phys.*, vol. 81, p. 3188, 1984.

[10] L. Verlet *Phys. Rev.*, vol. 159, p. 98, 1967.

[11] W. Swope, H. Andersen, P. Berens, and K. Wilson *J. Chem. Phys.*, vol. 76, p. 637, 1982.

[12] A. Malevanets and R. Kapral *J. Chem. Phys.*, vol. 110, p. 8605, 1999.

[13] A. Malevanets and R. Kapral *J. Chem. Phys.*, vol. 112, p. 7260, 2000.

[14] J. D. Weeks, D. Chandler, and H. C. Andersen *J. Chem. Phys.*, vol. 54, p. 5237, 1971.

[15] U. Gasser *J. Phys.: Condens. Matter*, vol. 21, p. 203101, 2009.

[16] C. M. Soukoulis, *Photonic Crystals and Light Localization in the 21st Century*. Kluwer Academic Publishers, 2001.

[17] M. Maldovan, C. K. Ullal, W. C. Carter, and E. L. Thomas *Nature Mater.*, vol. 2, p. 664, 2003.

[18] A. Moroz *Phys. Rev. B*, vol. 66, p. 115109, 2002.

[19] A. J. Garcia-Adeva *New J. Phys.*, vol. 8, p. 86, 2006.

[20] T. Ngo, C. M. Liddell, M. Ghebrebrhan, and J. D. Joannopoulos *Appl. Phys. Lett.*, vol. 88, p. 241920, 2006.

[21] W. B. Pearson, *The Crystal Chemistry and Physics of Metals and Alloys*. New York: Elsevier, 1972.

[22] A.-P. Hynninen, J. H. J. Thijssen, E. C. M. Vermolen, M. Dijkstra, and A. van Blaaderen *Nature Mater.*, vol. 6, p. 202, 2007.

[23] A.-P. Hynninen, L. Filion, and M. Dijkstra *J. Chem. Phys.*, vol. 131, p. 064902, 2009.

[24] E. V. Shevchenko, D. V. Talapin, N. A. Kotov, S. O'Brien, and C. B. Murray *Nature*, vol. 439, p. 55, 2006.

[25] G. H. Ma, T. Fukutomi, and N. Morone *J. Colloid Interface Sci.*, vol. 168, p. 393, 1994.

[26] S. Yoshimura and S. Hachisu *Prog. Colloid Polym. Sci.*, vol. 68, p. 59, 1983.

[27] P. Bartlett, R. H. Ottewill, and P. N. Pusey *Phys. Rev. Lett.*, vol. 68, p. 3801, 1992.

[28] E. C. M. Vermolen, *Manipulation of Colloidal Crystalization.* PhD thesis, Utrecht University, 2008.

[29] J. S. Turner *Annu. Rev. Fluid Mech.*, vol. 6, p. 37, 1974.

[30] D. Velegol, S. Shori, and C. E. Snyder *Industrial & Engineering Chemistry Research*, vol. 48, p. 2414, 2009.

[31] H. A. Jerri, W. P. Sheehan, C. E. Snyder, and D. Velegol *Langmuir*, vol. 26, p. 4725, 2010.

[32] C. Royall, J. Dzubiella, M. Schmidt, and A. van Blaaderen *Phys. Rev. Lett.*, vol. 98, p. 188304, 2007.

[33] J. T. Padding and A. A. Louis *Phys. Rev. E*, vol. 77, p. 011402, 2008.

[34] A. Wysocki, C. P. Royall, R. G. Winkler, G. Gompper, H. Tanaka, A. van Blaaderen, and H. Löwen *Faraday Discuss.*, vol. 144, pp. 245–252, 2010.

[35] A. Wysocki, C. P. Royall, R. G. Winkler, G. Gompper, H. Tanaka, A. van Blaaderen, and H. Löwen *Soft Matter*, vol. 5, pp. 1340–1344, 2009.

[36] S. Chandrasekhar, *Hydrodynamic and Hydromagnetic Stability.* Oxford: Oxford University Press, 1961.

[37] J. T. Padding and A. A. Louis *Phys. Rev. Lett.*, vol. 93, p. 220601, 2004.

[38] J. K. G. Dhont, *An Introduction to Dynamics of Colloids.* Amsterdam: Elsevier, 1996.

[39] A. Moncho-Jordá, A. A. Louis, and J. T. Padding *Phys. Rev. Lett.*, vol. 104, p. 068301, 2010.

[40] M. Hecht, J. Harting, T. Ihle, and H. J. Herrmann *Phys. Rev. E*, vol. 72, p. 011408, 2005.

[41] M. Hecht, J. Harting, M. Bier, J. Reinshagen, and H. J. Herrmann *Phys. Rev. E*, vol. 74, p. 021403, 2006.

[42] M. Hecht, J. Harting, and H. J. Herrmann *Phys. Rev. E*, vol. 75, p. 051404, 2007.

[43] S. H. Lee and R. Kapral *J. Chem. Phys.*, vol. 124, p. 214901, 2006.

[44] M. Ripoll, R. G. Winkler, and G. Gompper *Phys. Rev. Lett.*, vol. 96, p. 188302, 2006.

[45] K. Mussawisade, M. Ripoll, R. G. Winkler, and G. Gompper *J. Chem. Phys.*, vol. 123, p. 144905, 2005.

[46] H. Noguchi and G. Gompper *Phys. Rev. Lett.*, vol. 93, p. 258102, 2004.

[47] J. L. McWhirter, H. Noguchi, and G. Gompper *Proc. Natl. Acad. Sci. U. S. A.*, vol. 106, pp. 6039–6043, 2009.

[48] H. Noguchi and G. Gompper *J. Chem. Phys.*, vol. 125, p. 164908, 2006.

[49] J. T. Padding and A. A. Louis *Phys. Rev. E*, vol. 74, p. 031402, 2006.

[50] T. Ihle and D. M. Kroll *Phys. Rev. E*, vol. 63, p. 020201, 2001.

[51] C. I. Mendoza and I. Santamaría-Holek *J. Chem. Phys.*, vol. 130, p. 044904, 2009.

[52] R. A. Usmani *Indian J. Pure Appl. Math*, vol. 14, pp. 398–411, 1983.

[53] K. O. Mikaelian *Phys. Rev. Lett.*, vol. 48, p. 1365, 1982.

[54] K. O. Mikaelian *Phys. Rev. E*, vol. 54, p. 3676, 1996.

[55] E. Santiso and E. Müller *Mol. Phys.*, vol. 100, p. 2461, 2002.

[56] N. Saito *J. Phys. Soc. Jpn.*, vol. 5, p. 4, 1950.

[57] S. C. Glotzer and M. J. Solomon *Nature Mater.*, vol. 6, p. 557, 2007.

[58] A. van Blaaderen *Science*, vol. 301, p. 470, 2003.

[59] V. N. Manoharan, M. T. Elsesser, and D. J. Pine *Science*, vol. 301, p. 483, 2003.

[60] M. Okubo, Z. Wang, E. Ise, and H. Minami *Colloid Polym. Sci.*, vol. 279, p. 976, 2001.

[61] S. Reculusa, C. Poncet-Legrand, A. Perro, E. Duguet, E. Bourgeat-Lami, C. Mingotaud, and S. Ravaine *Chem. Mater.*, vol. 17, p. 3338, 2005.

[62] A. Perro, S. Reculusa, E. Bourgeat-Lami, E. Duguet, and S. Ravaine *Colloids and Surfaces A*, vol. 284, p. 78, 2006.

[63] D. Nagao, M. Hashimoto, K. Hayasaka, and M. Konno *Macromol. Rapid Commun.*, vol. 29, p. 1484, 2008.

[64] D. J. Kraft, J. Groenewold, and W. K. Kegel *Soft Matter*, vol. 5, p. 3823, 2009.

[65] D. Nagao, C. M. van Kats, K. Hayasaka, M. Sugimoto, M. Konno, A. Imhof, and A. van Blaaderen *Langmuir*, vol. 26, p. 5208, 2010.

[66] W. G. Hoover and F. H. Ree *J. Chem. Phys.*, vol. 49, p. 3609, 1968.

[67] B. J. Alder, W. G. Hoover, and D. A. Young *J. Chem. Phys.*, vol. 49, p. 3688, 1968.

[68] L. V. Woodcock *Nature*, vol. 385, p. 141, 1997.

[69] P. G. Bolhuis, D. Frenkel, S. C. Mau, and D. A. Huse *Nature*, vol. 388, p. 236, 1997.

[70] S. Mau and D. A. Huse *Phys. Rev. E*, vol. 59, p. 4396, 1999.

[71] K. Wojciechowski *Phys. Lett. A*, vol. 122, p. 377, 1987.

[72] J. D. McCoy, S. Singer, and D. Chandler *J. Chem. Phys.*, vol. 87, p. 4853, 1988.

[73] S. J. Smithline, S. W. Rick, and A. D. J. Haymet *J. Chem. Phys.*, vol. 88, p. 2004, 1988.

[74] K. W. Wojciechowski, D. Frenkel, and A. C. Branka *Phys. Rev. Lett.*, vol. 66, p. 3168, 1991.

[75] C. Vega, E. P. A. Paras, and P. A. Monson *J. Chem. Phys.*, vol. 96, p. 9060, 1992.

[76] C. Vega, E. P. A. Paras, and P. A. Monson *J. Chem. Phys.*, vol. 97, p. 8543, 1992.

[77] M. Kowalik and K. W. Wojciechowski *J. Non-Crystalline Solids*, vol. 354, p. 4354, 2008.

[78] M. Marechal and M. Dijkstra *Phys. Rev. E*, vol. 77, p. 061405, 2008.

[79] P. Bartlett, R. H. Ottewill, and P. N. Pusey *J. Chem. Phys.*, vol. 93, p. 1299, 1990.

[80] N. Hunt, R. Jardine, and P. Bartlett *Phys. Rev. E*, vol. 62, p. 900, 2000.

[81] M. J. Murray and J. V. Sanders *Philosophical Magazine A*, vol. 42, p. 721, 1980.

[82] J. K. Kummerfeld, T. S. Hudson, and P. Harrowell *J. Phys. Chem. B*, vol. 112, p. 10773, 2008.

[83] T. S. Hudson and P. Harrowell *J. Phys.: Condens. Matter*, vol. 23, p. 194103, 2011.

[84] L. Filion and M. Dijkstra *Phys. Rev. E*, vol. 79, p. 046714, 2009.

[85] L. Filion, M. Marechal, B. van Oorschot, D. Pelt, F. Smallenburg, and M. Dijkstra *Phys. Rev. Lett.*, vol. 103, p. 188302, 2009.

[86] D. P. Stucke and V. H. Crespi *Nano Letters*, vol. 3, p. 1183, 2003.

[87] A. Šarić, B. Bozorgui, and A. Cacciuto *J. Phys. Chem. B*, vol. 79, p. 046714, 2011.

[88] A. Brańka and K. W. Wojciechowski *Mol. Phys.*, vol. 78, p. 1513, 1993.

[89] K. W. Wojciechowski *Phys. Rev. B*, vol. 46, p. 26, 1992.

[90] E. Widom *J. Chem. Phys.*, vol. 39, p. 2808, 1963.

[91] J. F. Nagle *Phys. Rev.*, vol. 152, p. 190, 1966.

[92] M. Dijkstra, R. van Roij, and R. Evans *Phys. Rev. E*, vol. 59, p. 5744, 1999.

[93] E. Trizac, M. D. Eldridge, and P. A. Madden *Mol. Phys.*, vol. 90, p. 675, 1997.

[94] M. D. Eldridge, P. A. Madden, P. N. Pusey, and P. Bartlett *Mol. Phys.*, vol. 84, p. 395, 1995.

[95] M. D. Eldridge, P. A. Madden, and D. Frenkel *Nature*, vol. 365, p. 34, 1993.

[96] W. Kranendonk and D. Frenkel *Mol. Phys.*, vol. 72, p. 679, 1991.

[97] L. Filion, M. Hermes, R. Ni, E. C. M. Vermolen, A. Kuijk, C. G. Christova, J. C. P. Stiefelhagen, T. Vissers, A. van Blaaderen, and M. Dijkstra *Phys. Rev. Lett.*, vol. 107, p. 168302, 2011.

[98] W. H. Evers, B. de Nijs, L. Filion, S. Castillo, M. Dijkstra, and D. Vanmaekelbergh *Nano Letters*, vol. 10, p. 4235, 2010.

[99] A. M. Wierenga, T. A. J. Lenstra, and A. P. Philipse *Colloids and Surfaces A. Physicochem. Eng. Aspects*, vol. 134, p. 359, 1998.

[100] A. Kuijk, A. van Blaaderen, and A. Imhof *J. Am. Chem. Soc.*, vol. 133, pp. 2346–2349, 2011.

[101] J.-M. Meijer, F. Hagemans, L. Rossi, D. V. Byelov, S. I. R. Castillo, A. Snigirev, I. Snigireva, A. P. Philipse, and A. V. Petukhov *Langmuir*, vol. 28, p. 7631, 2012.

[102] C. J. DeSantis and S. E. Skrabalak *Langmuir*, vol. 28, p. 9055, 2012.

[103] M. Dennison, K. Milinković, and M. Dijkstra *J. Chem. Phys.*, vol. 137, p. 044507, 2012.

[104] J. D. Forster, J.-G. Park, M. Mittal, H. Noh, C. F. Schreck, C. S. O'Hern, H. Cao, E. M. Furst, and E. R. Dufresne *ACS Nano*, vol. 5, p. 6695, 2011.

[105] I. D. Hosein, S. H. Lee, and C. M. Liddell *Adv. Funct. Mater.*, vol. 20, p. 3085, 2010.

[106] E. B. Mock and C. F. Zukoski *Langmuir*, vol. 26, p. 13747, 2010.

[107] N. Chaturvedi, B. Juluri, Q. Hao, T. Huang, and D. Velegol *Journal of Colloid and Interface Science*, vol. 371, p. 28, 2012.

[108] M. Hoffmann, M. Siebenbürger, L. Harnau, M. Hund, C. Hanske, Y. Lu, C. S. Wagner, M. Drechsler, and M. Ballauff *Soft Matter*, vol. 6, pp. 1125–1128, 2010.

[109] S. Sacanna, W. T. M. Irvine, L. Rossi, and D. J. Pine *Soft Matter*, vol. 7, p. 1631, 2011.

[110] S. J. Gerbode, U. Agarwal, D. C. Ong, C. M. Liddell, F. Escobedo, and I. Cohen *Phys. Rev. Lett.*, vol. 105, p. 078301, 2010.

[111] P. N. Pusey and W. van Megen *Nature*, vol. 320, p. 340, 1986.

[112] J. M. Polson, E. Trizac, S. Pronk, and D. Frenkel *J. Chem. Phys.*, vol. 112, p. 5339, 2000.

[113] C. Vega and E. Noya *J. Chem. Phys.*, vol. 127, p. 154113, 2007.

[114] C. Vega and P. Monson *J. Chem. Phys.*, vol. 107, p. 2696, 1997.

[115] M. Hoffmann, Y. Lu, M. Schrinner, M. Ballauff, and L. Harnau *J. Phys. Chem. B*, vol. 112, pp. 14843–14850, 2008.

[116] M. Hoffmann, C. S. Wagner, L. Harnau, and A. Wittemann *ACS Nano*, vol. 3, p. 3326, 2009.

[117] S. Deka, K. Miszta, D. Dorfs, A. Genovese, G. Bertoni, and L. Manna *Nano Lett.*, vol. 10, pp. 3770–3776, 2010.

[118] S. Chen, Z. L. Wang, J. Ballato, S. H. Foulger, and D. L. Carroll *J. Am. Chem. Soc.*, vol. 125, pp. 16186–16187, 2003.

[119] Y. Wang, Y. Wang, D. R. Breed, V. N. Manoharan, L. Feng, A. D. Hollingsworth, M. Weck, and D. J. Pine *Nature*, vol. 491, pp. 51–55, 2012.

[120] A. Yethiraj and A. van Blaaderen *Nature*, vol. 421, pp. 513–517, 2003.

[121] O. Cayre, V. N. Paunov, and D. O. Velev *J. Mater. Chem.*, vol. 13, pp. 2445–2450, 2003.

[122] T. Besseling, 2012. unpublished.

[123] B. Derjaguin and L. Landau *Acta Physicochim. URSS*, vol. 14, p. 633, 1941.

[124] E. J. W. Verwey and J. T. G. Overbeek, *Theory of the stability of lyotropic colloids.* Amsterdam: Elsevier, 1948.

[125] A.-P. Hynninen and M. Dijkstra *Phys. Rev. E*, vol. 68, p. 021407, 2003.

[126] A. F. Demirörs, *Anisotropic colloids: synthesis and phase behavior of eccentric, dimer and string-like colloids.* PhD thesis, Utrecht University, 2010.

[127] P. R. ten Wolde, *Numerical Study of Pathways for Homogeneous Nucleation.* PhD thesis, University of Amsterdam, 1998.

[128] W. Lechner and C. Dellago *J. Chem. Phys.*, vol. 129, p. 114707, 2008.

[129] T. Kawasaki and H. Tanaka *PNAS*, vol. 107, pp. 14036–14041, 2010.

[130] L. Filion, M. Hermes, R. Ni, and M. Dijkstra *J. Chem. Phys.*, vol. 133, p. 244115, 2010.

[131] R. Ni and M. Dijkstra *J. Chem. Phys.*, vol. 134, p. 034501, 2011.

[132] W. Lechner, C. Dellago, and P. G. Bolhuis *Phys. Rev. Lett.*, vol. 106, p. 085701, 2011.

[133] J. A. C. Veerman and D. Frenkel *Phys. Rev. A*, vol. 45, pp. 5632–5648, 1992.

Summary

Colloidal suspensions, which we study in this thesis, consist of microscopic particles dispersed in a continuous medium. Our interest in these systems is mainly based on two things: they are considered an important model system for atomic and molecular behavior, and also the rich variety of different colloidal particles that can be synthesized nowadays makes them a promising class of systems for practical applications. Furthermore, the time and length scales associated with colloids are large enough to make single particle level studies in real time and real space possible.

An important characteristic of colloidal particles is that when suspended in a solvent they experience collisions with fast-moving solvent molecules which, together with thermal fluctuations within the solvent, lead to the colloids performing Brownian motion. These thermal fluctuations allow colloidal systems to explore the phase space in order to find the most favorable configuration, making, in principle, colloidal self-assembly possible. In this thesis we aim to investigate the collective properties of a number of different colloidal systems using computer simulations. A brief description of the two main simulation techniques used, namely molecular dynamics and Monte Carlo algorithms, is given in the introductory chapter (Chapter 1). The systems we focus on are binary mixtures of hard-sphere-like particles (Chapters 2 and 3) and monodisperse systems of dimer particles interacting both via hard-core (Chapters 4 and 5) and repulsive Yukawa interactions (Chapters 6).

In Chapters 2 and 3 we study hydrodynamic instabilities in binary colloidal mixtures. Specifically, we study Rayleigh-Taylor-like instabilities in the context of colloidal suspensions with different compositions and different particle properties. Starting from a configuration with a layer of heavier fluid placed above a lighter one, the simulated suspensions undergo a Rayleigh-Taylor-like instability which is a gravity induced instability of the interface separating the two fluids. The initial undulations of the interface are accompanied by strong density fluctuations and also the formation of characteristic network-like patterns in the direction perpendicular to gravity. In order to be able to capture this behavior when simulating colloidal systems it is essential to employ a computer simulation method that incorporates both Brownian motion and hydrodynamic interactions, and the method we used in this work is a hybrid between molecular dynamics and stochastic rotation dynamics techniques. To investigate how different particle properties influence the formation and the evolution of the instability we simulate binary mixtures with a range of relative Peclet numbers of the particle species. We found that the distributions of the colloids within the colloid rich regions that form as a consequence of the density fluctuations induced by the instability do not depend significantly on the composition of the mixtures. However, we did see a strong dependence of the distributions of the different species on the relative magnitudes of the Peclet numbers - a much higher degree of mixing is observed in the case when the smaller particles have smaller Peclet numbers than in the case when the smaller particles have larger Peclet numbers. In the latter case the particle species had become separated in such a way that the smaller, heavier colloids were positioned mostly in the inner parts of the colloid rich regions and were enveloped

by the the larger, lighter particles. To follow the dynamics of the instability formation we calculated the spatial colloid velocity correlation functions which allow us to investigate how the characteristic correlation length in the mixtures develops in time. We observed alternating regions in which the sedimentation velocities of the particles were correlated and anticorrelated, which is consistent with the network-like structure observed in the simulation snapshots. To study the instability behavior on a more coarse grained level, we calculated the growth rates of the unstable modes both from the simulation data and using a theoretical approach and we found good agreement between the results of both methods. The growth rates in the theoretical approach were calculated numerically from the linearized Navier-Stokes equation which describes the instability. This equation required a suitably defined viscosity profile of the binary sediment.

For the remainder of the thesis we focused on the phase behavior of monodisperse dimer systems. Snowman-shaped particles, which we studied in Chapter 4, consist of two hard spheres with diameters D_1 and D_2 rigidly attached at their surfaces. We calculated the phase diagram for the constituent sphere diameter ratios $d = D_1/D_2$ ranging from 0 to 1 using Monte Carlo simulations and free energy calculations. Depending on the diameter ratio of the snowmen particles, these systems form a variety of stable crystalline phases including isotropic fluid, plastic crystal and aperiodic crystal phases. Aperiodic crystals are characterized by the constituent spheres located on lattice sites of a binary crystal while the orientations of the resulting snowman-shaped particles are aperiodic. At high densities, the structures found to be stable for a given sphere diameter ratio correspond to the close packed structures predicted for equimolar binary hard-sphere mixtures with the same diameter ratio. However, we also predict several crystal-crystal phase transitions such that structures with a higher degree of degeneracy are found to be stable at lower densities.

The systems we studied in Chapter 5 consist of particles ranging from a hard snowman-shaped particle with $d = 0.5$ to a hard sphere. The particle shape is varied by reducing the particle length through the reduction of the separation of the constituent spheres. Investigating the phase behavior of these systems and comparing to the already known phase behavior of snowman-shaped particle systems allows us to further investigate the interplay between packing and degeneracy entropy. To obtain the phase diagram of hard asymmetric dumbbell particles with the constituent sphere diameter ratio of $d = 0.5$, we used Monte Carlo simulations and free energy calculations. The phases found to be stable depending on the constituent sphere separation are isotropic fluid, rotator, and periodic $NaCl$-based and both periodic and aperiodic CrB-based crystalline phases. We note that no periodic structures were found to be stable in snowman-shaped particle systems suggesting that reducing the sphere separation results in the aperiodic crystalline phases becoming destabilized as compared to the phase behavior of snowman-shaped particles. The rotator phases predicted to be stable for systems of hard asymmetric dumbbells with low constituent sphere separations have similar stability ranges as those found in systems of snowman-shaped and dumbbell particles. We investigated the properties of these phases by comparing their stability ranges and by looking at the orientational reorganization of particles. Finally, we found that the stable periodic $NaCl$-based crystalline phase can expand its range of stability by undergoing a slight modification which allows it to pack better.

Chapter 6 is dedicated to studying the phase behavior of systems of hard-core repulsive Yukawa dumbbells consisting of equal sized spheres of diameter D and sphere separation $0.5D$. We simulated systems interacting via a range of repulsive potentials, characterized by different potential screening lengths, in order to investigate how the range of the particle repulsions affects the system phase behavior. We found that dumbbells with sufficiently long-ranged repulsive interactions, when compressed, crystallize spontaneously into rotator phases in which the particle centers of mass are located on average on a BCC crystal lattice. The underlying structure was determined by examining the local bond order parameters. We also calculated the auto- and spatial orientational correlation functions which indicate the absence of any significant hindrance of the particle rotations even for the shortest ranged interactions studied.

Samenvatting

Colloïdale suspensies, welke we bestuderen in dit proefschrift, bestaan uit microscopische deeltjes gedispergeerd in een continu medium. Onze belangstelling voor deze systemen vloeit voornamelijk voort uit twee dingen: ze worden gezien als een belangrijk modelsysteem voor atomair en moleculair gedrag, en de rijke verscheidenheid aan colloïdale deeltjes die tegenwoordig gesynthetiseerd kunnen worden maakt hen een veelbelovende systeemsoort voor praktische toepassingen. Tevens zijn de tijd- en lengteschalen geassocieerd met colloïden groot genoeg om onderzoek op het niveau van enkele deeltjes in realtime en in positieruimte mogelijk te maken.

Een belangrijke eigenschap van colloïdale deeltjes is dat als ze opgelost zijn in een oplosmiddel, ze botsingen ondervinden van snel bewegende oplosmiddelmoleculen, hetgeen samen met thermische fluctuaties in het oplosmiddel ertoe leidt dat de colloïden Browns bewegen. Deze thermische fluctuaties maken het mogelijk voor colloïdale systemen om hun faseruimte te verkennen en zo hun gunstigste configuratie de vinden, hetgeen in principe colloïdale zelfassemblage mogelijk maakt. In dit proefschrift hebben we als doel om de collectieve eigenschappen van een aantal verschillende colloïdale systemen te onderzoeken met behulp van computersimulaties. Een korte beschrijving van de twee voornaamste gebruikte simulatietechnieken, namelijk moleculaire dynamica en Monte Carlo-algoritmes, wordt gegeven in het introductiehoofdstuk (Hoofdstuk 1). De systemen waarop we ons concentreren zijn binaire mengsels van hardebollenachtige deeltjes (Hoofdstuk 2 en 3) en monodisperse systemen van dimeerdeeltjes die zowel volgens een hardekernrepulsie (Hoofdstuk 4 en 5) alsook volgens afstotende Yukawa-interacties (Hoofdstuk 6) wisselwerken.

In Hoofdstuk 2 en 3 bestuderen we hydrodynamische instabiliteiten in binaire colloïdale mengsels. Om precies te zijn bestuderen we Rayleigh-Taylorachtige instabiliteiten in de context van colloïdale suspensies met verschillende samenstellingen en deeltjeseigenschappen. Beginnend met een configuratie met een laag van zwaarder vloeistof geplaatst bovenop een lichtere vloeistof ondergaan de suspensies een Rayleigh-Taylorachtige instabiliteit, hetgeen een instabiliteit van het grensvlak tussen de twee vloeistoffen is, geïnduceerd door zwaartekracht. De aanvankelijke golvingen van het grensvlak worden vergezeld door sterke dichtheidsfluctuaties en ook de vorming van karakteristieke netwerkachtige patronen in de richting loodrecht op die van de zwaartekracht. Om in staat te zijn dit gedrag te vangen in simulaties van colloïdale systemen is het essentieel om computersimulaties te gebruiken die zowel Brownse beweging alsook hydrodynamische interacties omvatten, en de methode die we gebruikten in dit werk is een tussenvorm van moleculaire dynamica en stochastische rotatiedynamicatechnieken. Om te onderzoeken hoe verschillende deeltjeseigenschappen de vorming en ontwikkeling van de instabiliteit beïnvloeden simuleren we binaire mengsels met een spreiding aan relatieve Pécletgetallen van de deeltjessoorten. We ontdekten dat de verdelingen van de colloïden binnen de colloïdrijke gebieden die zich vormen als gevolg van de dichtheidsfluctuaties geïnduceerd door de instabiliteit, niet significant afhangen van de samenstelling van de mengsels. We zagen echter dat de verdeling van de verschillende deeltjes sterk afhangt van de relatieve

grootte van de Pécletgetallen - we bemerkten een veel grotere mate van vermenging in het geval dat de kleinere deeltjes een kleiner Pécletgetal hebben dan in het geval dat de kleinere deeltjes een groter Pécletgetal hebben. In het laatstgenoemde geval waren de deeltjessoorten gescheiden geraakt op zo'n manier dat de kleinere, zwaardere colloïden voornamelijk gepositioneerd waren in het binnengedeelte van de colloïdrijke gebieden terwijl de grotere, lichtere deeltjes hen omringden. Om de dynamica van de vorming van de instabiliteit te volgen hebben we de ruimtelijke correlatiefuncties van de colloïdsnelheid berekend, die het mogelijk maken te onderzoeken hoe de karakteristieke correlatielengte in de mengsels zich ontwikkelt als functie van de tijd. We zagen afwisselend regio's waarin de sedimentatiesnelheden van de deeltjes gecorreleerd en antigecorreleerd waren, hetgeen consistent is met de netwerk-achtige structuur gezien in de momentopnames van de simulaties. Om de instabiliteit te bestuderen met een grovere korreligheid hebben we de groeisnelheden uitgerekend van de instabiele fluctuaties zowel uit de simulatiedata alsook gebruik makend van een theoretische aanpak, en we vonden goede overeenstemming tussen de resultaten van beide methoden. De groeisnelheden in de theoretische aanpak werden numeriek uitgerekend uit de gelineariseerde Navier-Stokes-vergelijking die de instabiliteit beschrijft. Deze vergelijking had een voldoende goed gedefinieerd viscositeitsprofiel van het binaire sediment nodig.

Voor de rest van dit proefschrift focusten we ons op het fasegedrag van monodisperse dimeersystemen. Sneeuwpopvormige deeltjes, bestudeerd in Hoofdstuk 4, bestaan uit twee harde bollen met diameters D_1 en D_2 waarvan de oppervlakken stijf aan elkaar vastzitten. We rekenden het fasediagram uit voor een reeks diameterverhoudingen $d = D_1/D_2$ van de samenstellende bollen, variërend van 0 tot 1, gebruik makend van Monte Carlo-simulaties en vrije-energieberekeningen. Afhankelijk van de diameterverhouding van de sneeuw-popdeeltjes vormen deze systemen een verscheidenheid aan stabiele kristallijne fases, zoals isotrope fluïden, plastic kristallen en niet-periodieke kristallen. Niet-periodieke kristallen worden gekenmerkt door het feit dat de samenstellende bollen zich bevinden op de rooster-erpunten van een binair kristal terwijl de oriëntaties van de sneeuwpopvormige deeltjes niet-periodiek zijn. Bij hoge dichtheid corresponderen de structuren waarvan gevonden was dat ze stabiel zijn voor een gegeven boldiameterverhouding met de dichtgestapelde structuren voorspeld voor equimolaire binaire hardebollenmengsels met dezelfde diameterverhouding.

De systemen die we bestudeerden in Hoofdstuk 5 bestaan uit deeltjes variërend van een hard sneeuwpopvormig deeltje met $d = 0.5$ tot een harde bol. De deeltjesvorm wordt gevarieerd door de deeltjeslengte te verminderen door de afstand tussen de samenstellende bollen kleiner te maken. Door het fasegedrag van deze systemen te onderzoeken en het te vergelijken met het al bekende fasegedrag van systemen van sneeuwpopvormige deeltjes kunnen we de wisselwerking tussen stapeling en ontaardingsentropie verder bestuderen. Om het fasediagram van harde asymmetrische dumbbelldeeltjes met diameterverhouding $d = 0.5$ van de samenstellende bollen te verkrijgen gebruikten we Monte Carlo-simulaties en vrije-energieberekeningen. De fases waarvan we ontdekten dat ze, afhankelijk van de afstand tussen de samenstellende bollen, stabiel waren, zijn een isotroop fluïde, een rotatorfase, en periodieke $NaCl$-gebaseerde en zowel periodieke als niet-periodieke CrB-gebaseerde kristallijne fases. We merken op dat geen periodieke structuren zijn gevonden die stabiel zijn in een systeem van sneeuwpopvormige deeltjes, hetgeen erop wijst dat

het verminderen van de bolafstand resulteert in het destabiliseren van de niet-periodieke kristallijne fases vergeleken met het geval van sneeuwpopvormige deeltjes. De rotatorfases waarvan we voorspellen dat ze stabiel zijn voor systemen van harde asymmetrische dumbbells met een kleine afstand tussen de samenstellende bollen hebben een vergelijkbaar stabiliteitsdomein als de gevonden in systemen van sneeuwpopvormige en dumbbelldeeltjes. We onderzochten de eigenschappen van deze fases door hun stabiliteitsdomeinen te vergelijken en door te kijken naar de oriëntatiereorganisatie van de deeltjes. Tenslotte ontdekten we dat de stabiele periodieke $NaCl$-gebaseerde kristallijne fase zijn stabiliteitsdomein kan vergroten door een kleine herschikking te ondergaan die een betere stapeling toelaat.

Hoofdstuk 6 is gewijd aan het bestuderen van het fasegedrag van systemen met Yukawa-repulsieve dumbbells met harde kern, bestaand uit bollen met gelijke diameter D en bolafstand $0.5D$. We simuleerden systemen wisselwerkend volgens een verscheidenheid aan afstotende potentialen gekarakteriseerd door verschillende drachten, om zo te onderzoeken hoe de dracht van de deeltjesrepulsies het fasegedrag van het systeem beïnvloedt. We vonden dat als ze gecomprimeerd worden, dumbbells met een afstotende interactie van voldoende lange dracht spontaan kristalliseren in rotatorfases waarin de massamiddelpunten van de deeltjes zich gemiddeld bevinden op een BCC-kristalrooster. De onderliggende structuur werd bepaald door de locale bindingsordeparameters te onderzoeken. We berekenden ook de auto- en ruimtelijke oriëntationele correlatiefuncties, die wijzen op de afwezigheid van welke significante hinder voor de deeltjesrotaties dan ook, zelfs voor de interacties met de kortste bestudeerde dracht.

Acknowledgments

Four years ago the idea of getting to the point of having created one of these booklets sounded quite surreal, from all the work that goes in, to the level of administrative alertness necessary. However, it has happened. And some people helped along the way.

First of all, of course, I would like to thank my supervisor Marjolein Dijkstra for giving me the opportunity to work in such an inspiring and dynamic environment as the SCM group is. I have learned a lot, not just about the work in this thesis, but also about the experimental side of colloidal research and science in general - the benefits of a group as large and varied as this. I am also grateful to Marjolein for all the interesting and diverse project ideas that made working on this thesis an exciting journey.

I would also like to thank Alfons van Blaaderen for all the critical comments on my work and also on my many presentations. Johan Padding, for his invaluable input on SRD and hydrodynamics in general - they made the first two chapters of this thesis possible. Matthieu Marechal, for the initial help and patience with the numerous technical and simulation issues I came across, and also for the inspiring science chats. Matthew Dennison, the work on phase behavior of various dumbbells and even the writing were a pleasure. Bas Kwaadgras for his exemplary knowledge of, and willingness to use, the Dutch language (see the Dutch summary section). And of course, all the members of SCM and adjacent groups I have had a pleasure of running into in the past 4 years: Arnout Imhof, René van Roij, Peter Helfferich, Judith Wijnhoven and the rest of the bachelor students/master students/PhD/postdoc crowd. I am also grateful to Tanja Schilling and Patrick Pfleiderer for setting me on a soft matter path in the first place.

However, not all the efforts were science (and admin) related. I am very grateful to Peter van Oostrum and Laura Filion for showing me how lovely the Utrecht area can be when explored by bike, and for persuading me to get on one for the first time in my life. Neither their task of persuading me nor my task of learning were particularly easy. As it turned out, it's not a bad skill to have. Joost de Graaf and Marjolein van der Linden, my dear office mates of 3.5/4 years, for all the help with deciphering many of the Netherlands specific issues, for a lovely office (complete with posters and plants), and all the experiences that come with sharing a room for such a long time. Johan Stiefelhagen must get a special mention for sharing his magical cookies and the cooking inspiration.

And finally: Zoran, Milena, Magdalena, Nana, Matthew, Marina, Bas, Marina, Marija and Jelena, particularly for everything, and for nothing in particular.

Kristina